Study of Cationic Substitution in Perovskite Oxides for Electrocatalysis of the Oxygen Evolution Reaction in Alkaline Environment

Henrik Lind Petlund

M.Sc. Thesis

in Materials Science for Energy and Nanotechnology

60 credits

Department of Chemistry

Faculty of Mathematics and Natural Science

UNIVERSITY OF OSLO

May 2022

2021

Study of Cationic Substitution in Perovskite Oxides for Electrocatalysis of the Oxygen Evolution Reaction in Alkaline Environment

Henrik Lind Petlund

http://www.duo.uio.no/

Print: Reprosentralen, University of Oslo

“If I have seen further it is by standing on the shoulders of giants”

Isaac Newton, 1675

Acknowledgements

This thesis is written as partial fulfilment of the requirements for a Master's degree in Materials Science for Energy and Nanotechnology at the Department of Chemistry, University of Oslo. The experimental work has been conducted between August 2020 and May 2022 at the Group for Electrochemistry, a part of the Centre for Materials Science and Nanotechnology (SMN) and the research project "Photovoltaic-assisted hydrogen generation (PH2ON)" supported by the Research Council of Norway (project number 288320).

I would first like to greatly thank my supervisors, Truls Norby and Athanasios Chatzitakis, for overseeing and guiding me. Your counsel and genuine encouragement have been key in order for me to conduct this work and tie it all together. Thanks to everyone in the group for Electrochemistry for our good discussions and for providing a great social environment.

A special appreciation goes to Alaa Faid and Svein Sunde from the Department of Materials Science and Engineering at the Norwegian University of Science and Technology (NTNU) in Trondheim for their help with in situ Raman spectroscopy. Thanks to Sebastian Prodinger from the Catalysis group at the University of Oslo for helping me with Brunauer-Emmet-Teller measurements. I further express my gratitude towards David Wragg from the Nafuma group at the University of Oslo and Magnus Sørby at IFE for their valuable assistance with Rietveld refinement.

Lastly, I would like to thank my lovely fiancé for her unending supporting and patience during these two last years.

Henrik Lind Petlund

15.05.22

Summary

As the world's power demand swells even bigger every year, the already worrying CO_2 emissions expand with it. If our future generations are going to inherit a healthy planet, measures must be taken to reduce the reliance on fossil fuels. A carbon free fuel that has great potential and is predicted to have a substantial role in the future sustainable energy mix, is hydrogen. Since it only emits water upon combustion, hydrogen is ideal in order for industries with large carbon footprints to transition towards lower emissions. Still, almost all hydrogen produced today comes from natural gas and is accompanied by enormous amounts of CO_2 emissions. Electrolysis of water is a green way of producing hydrogen, when the electricity comes from renewable energy sources. However, a limiting factor of water electrolysis today is the slow kinetics of the anodic oxygen evolution reaction (OER). Earth-abundant, highly efficient and low cost electrocatalysts are therefore needed to reduce the energy losses and total costs of water electrolysis.

In this work, we synthesised 17 oxygen evolution electrocatalysts based on the parent oxide perovskite $Ba_{0.5}Gd_{0.8}La_{0.7}Co_2O_{6-\delta}$ (BGLC587) through the sol-gel citrate synthesis route. We substituted Co on B-site with different amounts of Fe and Ni, having the general formula $Ba_{0.5}Gd_{0.8}La_{0.7}Co_{2-x-y}Fe_xNi_yO_{6-\delta}$. Furthermore, we substituted Ba with K, Ca and Cs and attempted nitrogen doping on the oxygen site. Physiochemical characterisation with XRD, SEM, TEM and Brunauer-Emmet-Teller surface area resulted in a thorough structural, elemental and morphological characterisation of the B-site substituted electrocatalysts. All materials revealed complex phase compositions and significant variations in physical surface area. Substitution with Fe increased the surface area, whereas Ni had less impact. The major $LaCoO_3$ ($R\bar{3}c$) phase in BGLC587 was found to be gradually replaced by the double perovskite, $BaGdCo_2O_{6-\delta}$ (*Pmmm*), phase and the single perovskite, $LaFeO_{3-\delta}$/$Gd_{0.8}La_{0.2}O_{3-\delta}$ (*Pbnm/Pnma*), phases with increasing Fe content. Ni substitution resulted in secondary phases of both NiO and $La_3Ni_2O_7$ (Ruddlesten-Popper type structure).

The electrocatalytic performance of the catalysts was assessed at room temperature in alkaline solution using linear sweep voltammetry, cyclic voltammetry, chronopotentiometry, chronoamperometry and electrochemical impedance spectroscopy. The A-site substituted materials had less significant impact on the OER activity and hence the extensive electrochemical characterisation was not carried out for these.

On the contrary, we found that substitution with Fe generally increased the OER performance and that a 30-70% Fe content gave the lowest overpotentials (428-439 mV) and Tafel slopes (64-73 mV dec^{-1}), however not as low as the state-of-the-art IrO_2 (330-450 mV). Based on the oxygen content in the Fe substituted electrocatalysts, we argue that the increased activity of these is due to a higher concentration of electron holes. However, no indication of higher valent Fe^{4+} was found by XPS or in situ Raman spectroscopy, thus we concluded that the electron holes are delocalised in the bulk of the structure or at Co.

Alloying with Ni had less impact on the activity, however we found that a combination of Fe and low Ni content showed outstanding activity. Particularly, substitution with 20% Fe and 10% Ni (BGLCFN2010) resulted in the overall highest specific activity (i_s) of 1.77 mA cm^{-2}_{oxide} at 400 mV overpotential. The overpotential at 10 mA cm^{-2}_{geo} was 451 mV. This was followed by the best performing Fe substituted materials with i_s from 1.04-1.21 mA cm^{-2}_{oxide}. The N-doped sample (BGLCN-NH3) also showed high catalytic activity with an overpotential of 429 mV at 10 mA cm^{-2}_{geo} and Tafel slope of 54 mV dec^{-1}. However, we explained this to be due to an exsolved Co layer on the surface and not a successful N-doping on oxygen site.

From Tafel slopes and in situ Raman spectroscopy, we found that the rate determining step of the OER in all catalysts is likely a proton-exchange reaction. We also found indication of oxy-hydroxide intermediates on Ni containing catalysts during OER, whereas Fe catalysts had only oxide termination. Based on this, we concluded that the OER is likely to progress through the adsorbate evolution mechanism (AEM) in the Fe-based electrocatalysts. Faradaic efficiency measurements of selected catalysts indicated close to 100% efficiency.

An increased stability was found from galvanostatic measurements at 10 mA cm^{-2}_{geo} with Fe substitutions of 50% and 70% (BGLCF50 and BGLCF70). These electrocatalysts experienced a 20% degradation after ~50 h, which was twice the duration of the pristine BGLC587. Since the activity of these were among the highest, it was concluded these materials do not follow the typically reported inverse trend that high activity is usually followed by poor stability. The best stability was found with 30% Fe and 20% Ni (BGLCFN3020), which endured for 84 h before reaching 20% degradation all the while operating at lower overpotentials than both BGLCF50 and BGLCF70. On the contrary, the electrocatalyst with 50% Ni (BGLCN50) showed the lowest stability with mediocre activity. Hence, we concluded that there must be a synergy in electrocatalysts with both Fe and low Ni content giving higher stability and activity.

This master's thesis hence contributes to further understanding of perovskites as earth-abundant oxygen evolution catalysts (OECs) and how their catalytic activity can be enhanced through tuning elemental composition, structure, electronic properties and reaction intermediates.

List of Abbreviations

AEM	Adsorbate evolution mechanism
AC	Alternating current
BGC	$BaGdCo_2O_{6-\delta}$
BGLC	$Ba_{1-x}Gd_{0.2-y}La_{x+y}Co_2O_{6-\delta}$
BGLC587	$Ba_{0.5}Gd_{0.8}La_{0.7}Co_2O_{6-\delta}$
BSE	Backscattered electrons
BET	Brunauer-Emmet-Teller
CA	Chronoamperometry
CP	Chronopotentiometry
CPE	Constant phase element
CE	Counter electrode
CV	Cyclic voltammetry
DFT	Density functional theory
EC	Electrocatalyst
EIS	Electrochemical impedance spectroscopy
ECSA	Electrochemically active surface area
EDS	Energy dispersive X-ray spectroscopy
GC	Gas chromatograph
GCE	Glassy carbon electrode
GLC	$Gd_{0.8}La_{0.2}CoO_{3-\delta}$
HER	Hydrogen evolution reaction
HS	High spin
HOR	Hydrogen oxidation reaction
ICA	Intrinsic catalytic activity
LC	$LaCoO_3$

LF	$LaFeO_3$
LOM	Lattice oxygen-participated mechanism
LS	Low spin
LSV	Linear sweep voltammetry
NZE	Net zero emission
OEC	Oxygen evolution catalyst
OER	Oxygen evolution reaction
ORR	Oxygen reduction reaction
PDOS	Partial density of states
PEC	Photoelectrochemical
PEM	Polymer electrolyte membrane
PM	Post mortem
PXRD	Powder X-ray diffraction
rds	Rate determining step
RE	Reference electrode
RHE	Reversible hydrogen electrode
RDE	Rotating disk electrode
SCE	Saturated calomel electrode
SSRS	Solid-state sintering reaction
SOE	Solid oxide electrolyser
SA	Specific activity
SHE	Standard hydrogen electrode
TM	Transition metal
WE	Working electrode
XPS	X-ray photoelectron spectroscopy

Table of Contents

1 Introduction

1.1 The Renewable Transition

In 2021, the emissions of CO_2 into the atmosphere through energy-related processes amounted to a staggering 33.0 gigatonnes [1]. This is an increase of about 60% over the last 30 years and reflects the increasing global power demand of the human kind which is, in fact, estimated to double over the course of the next 30 years [2]. To cope with this tremendous increase, it is necessary to facilitate a large-scale transition from fossil fuels towards renewable energy sources and consequently moderating the ongoing global warming. Since about 80% of the world's total energy supply comes from fossil fuels [3], this transition will require a great turnover by the world's industry and infrastructure. With Russia's invasion of Ukraine, especially Europe has started to think of ways to become more independent on fossil fuels from Russia, which can be an incentive for boosting the renewable transition and restructuring the European energy map.

Several clean alternatives to harvesting energy has already been developed, some examples are solar-, water-, wind-, wave-, and geothermal power. All these power generating methods have their advantages and disadvantages, but typically, they all generate electricity. As of 2020, renewables stood for roughly 29% of the global electricity production, but it is expected that it must reach more than 60% by 2030 if the International Energy Agency's (IEAs) goal of net zero emissions (NZE) is to be reached by 2050 [4].

Among the renewable energy sources receiving attention, both wind and solar photovoltaic (PV) power have a great potential and is two of the fastest growing renewable power generation technologies [5]. However, it is important to address their intermittent nature if the energy is to be used efficiently. In general, the electricity demand at a certain time does not always match the amount of electricity produced and may cause periods of excess energy, which is essentially lost. One way to address this is to store the energy for later use and which can be realised by converting it into chemical energy in for example batteries or as a fuel such as hydrogen.

1.2 The Role of Hydrogen

Hydrogen is a versatile and important element and chemical participating in several processes in nature as well as modern industry. It is a highly abundant element and biologically speaking; life on earth depends on it. The versatility of hydrogen originates from the possibility to use it as a fuel, in energy storage and chemical processes in industry. Already today, hydrogen is being used as fuel in vehicles for transportation. This includes long-range transport sectors such as shipping, but also short-distance fuel cell electric vehicles (FCEVs) have been commercialised in recent years where several more are expected to be in the pipeline [6].

Figure 1.1 shows how hydrogen can be distributed across several sectors from 2020 to 2050 as modelled by IEA in their Net Zero Emissions report. This emphasises the future importance of hydrogen as part of the global energy economy. In addition, hydrogen-based fuels (hydrogen, ammonia and synthetic hydrocarbon fuels from hydrogen and CO_2) are anticipated to deliver 13% of the global final energy demand in 2050. Moreover, about 60% of the hydrogen production will have to come from electrolysis of water [7].

When produced from electrolysis of water, compressed hydrogen may serve as a clean energy carrier with a high energy density competing with solid-state batteries [8]. With a specific density of 33.3 kWh kg^{-1}, hydrogen outshines both natural gas, petrol and diesel [9]. However, the energy density (kWh dm^{-3}) of these are much higher, ultimately imposing a costly volumetric limitation on the storage and transportation of liquefied, compressed and absorbed hydrogen [10].

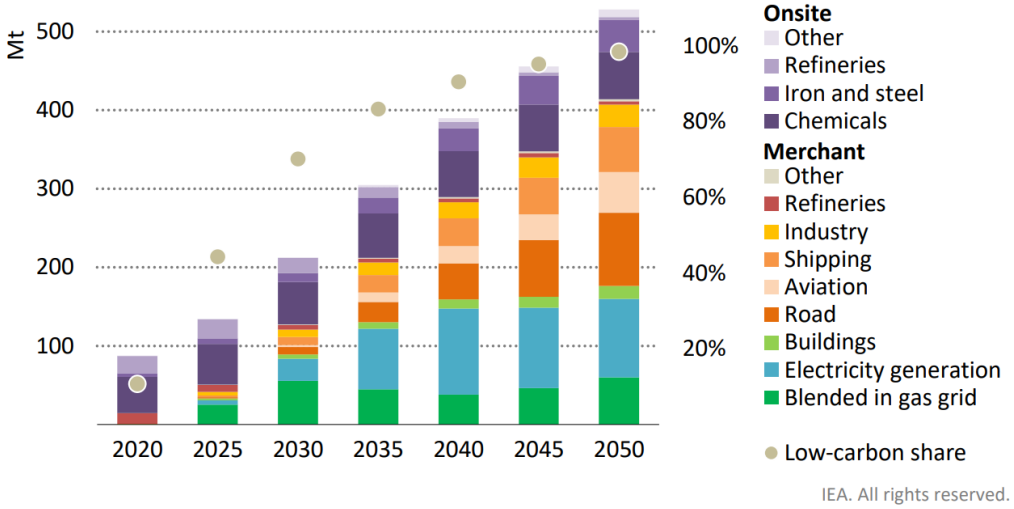

Figure 1.1: Modelled distribution of H_2 in megatons across different energy demanding sectors to reach Net Zero Emissions (NZE) by 2050 as laid out by IEA. Circles indicate the share of low-carbon hydrogen [7].

1.3 Water Splitting

Hydrogen production from renewable energy sources such as solar energy is now, more than ever, among the most apparent choices if we are to build a renewable energy society. Utilising the photovoltaic phenomenon is one way of harvesting solar energy by the conversion of photons into electricity. PV power generation has already been available for many years and has grown to produce about 3.0 % of the world's electricity demand as of 2019 [11]. However, as mentioned, the intermittent feature of solar power gives rise to the need for storage solutions. Therefore, storing excess energy as hydrogen through i.e. conventional electrolysis of water or photoelectrochemical (PEC) water splitting can be a potential solution to this. In an official study for EU by Albrecht et al., PEC hydrogen production is also underlined as one of the six most prominent methods for production in the EU [12].

A benefit of PEC water splitting is that it is performed in a 2-in-1 system because the hydrogen is evolved at the same geographical position as the harvested sunlight. This makes PEC water splitting a direct solar-to-hydrogen technique, which has great potential for off-grid hydrogen production. That is fundamentally different from electrolysis systems that need electricity from the grid, such as solid oxide electrolysers (SOEs) and the alkaline polymer electrolyte membrane (PEM) electrolyser. As opposed to these, PEC water splitting can ultimately reduce energy loss associated with transportation of the electricity on the grid.

Nevertheless, whether the hydrogen is produced by PEM electrolysers, SOEs or photoelectrochemically, the efficiency of these methods needs to increase. In order for them to be competitive options compared to hydrogen produced from fossil fuels, they must become viable and cost-effective. It is estimated that the current cost of producing hydrogen from fossil fuels is around 1.40 USD per kg, which is much lower than what any renewable production method have achieved today. However, it is estimated that under optimistic conditions, these water-splitting technologies may be able to reach this level before 2050 [10].

1.4 The Oxygen Evolution Reaction (OER)

An important efficiency-limiting factor of alkaline water splitting is the oxygen evolution reaction (OER). The kinetics of this anodic half-reaction is much more complex compared to its counterpart: the hydrogen evolution reaction (HER). While the HER, in Equation (1.2), is a two-electron-transfer process with a relatively well known reaction path, the OER, in Equation (1.1), is a four-electron-transfer process with several different proposed reaction paths and mechanisms highly reliant on the electrode of choice [13].

The standard reduction potentials in pH = 14 of the OER and HER are also given in Equation (1.1) and (1.2) respectively. Equation (1.3) contains the total water splitting reaction with its standard reversible potential, E^0_{rev}. The negative sign of E^0_{rev} indicates that it is a nonspontaneous reaction.

$$4OH^-(aq) + 4h^{\cdot} \rightarrow O_2(g) + 2H_2O(l) \qquad E^0 = -0.40\ V \tag{1.1}$$

$$4H_2O(l) \rightarrow 2H_2(g) + 4OH^-(aq) + 4h^{\cdot} \qquad E^0 = -0.83\ V \tag{1.2}$$

$$2H_2O(l) \rightarrow 2H_2 + O_2(g) \qquad E^0_{rev} = -1.229\ V \tag{1.3}$$

According to thermodynamics, a potential difference of 1.229 V is required to dissociate water into O_2 and H_2 gas, though in practice, the OER adds a substantial potential requirement known as overpotential. The overpotential is a consequence of kinetic hindrance of the electrochemical reaction [14], and since the HER is much more feasible, it also requires significantly less overpotentials compared to the OER in both acidic and alkaline solutions. This is exemplified in Figure 1.2 which gives the overpotentials of some OER and HER electrocatalysts from literature in both acidic and alkaline environments.

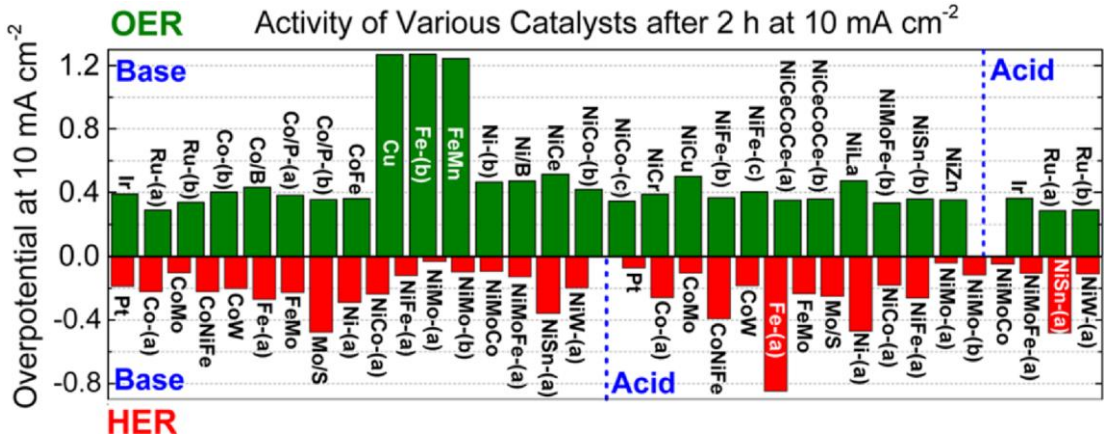

Figure 1.2: Overpotentials obtained at 10 mA cm^{-2}_{geo} for some electrocatalysts during OER and HER in both alkaline and acidic environment [15].

The identification of the bottleneck in electrochemical water splitting, which we now understand is that of the OER, has paved the way for the development of novel electrocatalysts. The historically most well known electrocatalyst for the OER is the noble metal oxides IrO_2 and RuO_2 exhibiting high activity at low overpotentials. Even though these are regarded as the state-of-the-art electrocatalysts, their low abundance and high cost have driven the research towards cheaper and more earth-abundant electrocatalysts. Many of the noble-metal-free OER

electrocatalysts being studied are Ni, Co, Fe and Mn-based hydroxides/oxyhydroxides, oxides, chalcogenides, nitrides and phosphides [16]. These transition metal electrocatalysts are especially interesting because of their tuneable oxidation states and structural versatility, which makes them suitable for optimising the OER activity. Today, several high-performance electrocatalysts comprised of these elements have already been reported [17, 18].

One group of materials, which has gained a large attention as potential electrocatalysts for the OER, is those having the perovskite-type structure. In general, perovskites have the formula ABO_3, but they may also have larger unit cells with more complex formulas, such as double and even quadruple perovskites. Electrocatalysts of the closely related Ruddlesden-Popper type structure has also been reported [19]. Perovskites have typically a small redox active transition metal cation, B, in corner-sharing BX_6 octahedra. The larger 12-coordinated A-site cations are typically chosen from the alkali, alkaline-earth or rare-earth metals. The X-site is often occupied by O-anions, but other anions such as chloride and nitride have also been reported [20-22]. The many possible configurations of A-, B- and X-sites of the perovskite structure have resulted in materials exhibiting very different properties, such as piezoelectricity, magnetoresistance, ionic conductivity and superconductivity ($LaAlO_3/SrTiO_3$ heterointerfaces) [23].

Electrocatalysts catalysing the OER are not only important for water splitting, but they are important in several other technologies. Some may play a vital role as anode materials in electrochemical cells for the reduction of CO_2 into valuable chemicals [16, 24]. Others may act as bifunctional catalyst in rechargeable metal-air batteries, where activity towards both the OER and oxygen reduction reaction (ORR) is desired [17, 21]. These two technologies are highly important for storage and utilisation of hydrogen as well as carbon capture, utilisation and storage (CCUS), which are all valuable in the transition towards a renewable society. Advances within OER electrocatalysis will therefore also benefit these scientific areas.

1.5 Aim and Approach

Recently, perovskite cobaltites with the general formula $Ba_{1-x}Gd_{0.8-y}La_{0.2+x+y}Co_2O_{6-\delta}$ (BGLC) were found to be stable and efficient anode materials for proton ceramic electrolysers (PCEs) at temperatures of around 600°C [25]. Inspired by this, BGLC was further investigated as electrocatalysts for the OER at room temperature in alkaline environment. This resulted in several different stoichiometries showing promising activities of which $Ba_{0.5}Gd_{0.8}La_{0.7}Co_2O_{6-\delta}$ (BGLC587) had the highest activity and stability [26, 27]. As a continuation of these studies, the main aim of this work is to further investigate and improve the OER activity of BGLC587

at room temperature in alkaline environment. The secondary aim is to reduce the content of cobalt in BGLC587 by substitution with the more benign transition metals Fe and Ni.

The approach taken in this work can be divided into three stages:

(1) Synthesis of A-, B- and O-site substituted BGLC587 catalysts
    a. A-site substitutions: K, Ca and Cs
    b. B-site substitution: Fe and Ni
    c. O-site substitution: N
(2) Extensive physiochemical and electrochemical characterization of the most active catalysts
(3) Discussion of mechanisms, activity performance and stability.

Our main hypothesis is that elements such as Fe and Ni can increase the OER performance of BGLC587 by B-site substitution. We rationalise this by referring to results from literature, where both Fe and Ni based electrocatalysts have been both predicted and shown to exhibit good OER activity, as well as stability [28-30]. One such material containing iron is $Ba_{0.5}Sr_{0.5}Co_{0.8}Fe_{0.2}O_{3-\delta}$ (BSCF82), which was found to have exceptional specific activity and is considered the benchmark perovskite oxide electrocatalyst for the OER [31].

We also hypothesise that A-site substitution with lower valent cations such as K^+ and Cs^+ will increase the OER activity by introducing more electron holes, which are important for the oxidation reaction at the anode. In terms of defect chemistry, this is justified by the fact that the lower valent cations acting as acceptors and thus increase the concentration of either oxygen vacancies or electron holes to charge compensate. Substitution with Ca is also considered at A-site because it was previously shown to improve activity and stability of a similar cobalt-based oxide perovskite [32].

To extract data on the OER performance of the novel electrocatalyst compositions, relevant electrochemical methods such as linear sweep voltammetry (LSV), cyclic voltammetry (CV), electrochemical impedance spectroscopy (EIS) and chronoamperometry/potentiometry (CA/CP) will be done. We will carry out a basic structural analysis with X-Ray diffraction (XRD), Rietveld refinement, electron microscopy and Brunauer-Emmet-Teller (BET) measurements in order to understand the effects of elemental substitution in connection to the electrochemical measurements.

As the last part of this work, we will discuss the results obtained from the abovementioned techniques. The OER activity and stability found from electrochemical methods will be compared with physical and chemical properties such as crystal structure, phase and elemental composition, morphology, surface area and electron configuration. To evaluate the electrocatalysts as promising and scalable, we will in this part also aim at determining plausible reaction mechanisms and reliable OER benchmark values for the electrocatalysts.

1.6 Outcome and Impact

The outcome of this work will be a better understanding of the interplay between physical, chemical and electrochemical properties of advanced perovskite based materials. We hope that it will contribute to an increased knowledge of kinetics and mechanisms of oxide perovskites as electrocatalysts for the OER in general and in close correlation to their structural features. The fundamental electrochemical studies carried out in this work will shed light on the pitfalls and the validity of relevant techniques and practices within aqueous electrochemistry and water electrolysis. The overarching aim of this thesis is hence to have an impact on the scientific progress in the field of electrocatalytic water splitting, as it will be an important part of the transition towards a renewable energy society.

2 Theory

2.1 Thermodynamics and Kinetics

The water splitting reaction in Equation (1.3) is an uphill, energy demanding reaction. At standard conditions (p = 1 bar and T = 298.15 K), this can be seen by calculating the Gibbs free energy change (ΔG_R^0) from Equation (2.1), where the number of electrons ($n = 2$) to produce one mole of H_2, the standard reversible cell potential ($E_{rev}^0 = -1.229$ V) and Faradays constant (F) and are used. The positive sign of ΔG_R^0 denotes that the water splitting reaction is not thermodynamically favourable.

$$\Delta G_R^0 = -nFE_{rev}^0 = +237.2 \text{ kJ mol}^{-1} \tag{2.1}$$

2.1.1 The Butler-Volmer Equation

To evaluate the kinetics of the OER we will need to utilise the Butler-Volmer equation. This equation tells us how the net current in an electrode is related to the concentration of reactants and products, temperature and the applied overpotential. To understand how the Butler-Volmer equation is derived, we start by looking at the simple oxidation reaction with one electron transfer a reduced species R in solution

$$R(soln) \leftrightharpoons e^- + O(soln) \tag{2.2}$$

where O is the oxidised species and R is the previously reduced species.

Electrode reactions can happen in an one-electron step such as in Equation (2.2), but they are typically much more complex consisting of several steps and multiple electron transfer processes. The OER and HER are no exceptions. However, it is believed that the more complex reactions can be expressed in steps of single-electron transfer reactions, much like the simple reaction in Equation (2.2) and in that way be systemised.

A system in chemical equilibrium has no net reaction rate, meaning that the forward and backward reaction rates are equal. Assuming that the reaction in Equation (2.2) has a net reaction rate, it can be expressed as

$$v_{net}(E) = v_{ox}(E) - v_{rd}(E) \tag{2.3}$$

where $v_{ox}(E)$ and $V_{rd}(E)$ is the forward (oxidation) and backward (reduction) reaction rates respectively. From the way the units of the reaction rate are defined in a heterogeneous system, Equation (2.3) can also be written as

$$\frac{i(E)}{F} = v_{ox}(E) - v_{rd}(E) \tag{2.4}$$

where $i(E)$ is the current density and F is Faradays constant. Equation (2.4) is also an explanation for why the anodic current at a working electrode is always positive.

The forward reaction rate is proportional to the activity of the reactants at the surface of the electrode

$$a_R^s = \gamma_R c_R^s / c^o \tag{2.5}$$

Where γ_R is the activity coefficient of R and c^o is the standard concentration. This further leads to Equation (2.6)

$$v_{ox}(E) = k_{ox}(E) a_R^s = k_{ox}(E) \gamma_R c_R^s / c^o = k'_{ox}(E) c_R^s \tag{2.6}$$

where $k_{ox}(E)$ and $k'_{ox}(E) = k_{ox}(E)\frac{\gamma_R}{c^o}$ are termed the oxidative rate constant and formal oxidative rate constant respectively. Using the same reasoning for the backward reaction rate, we can formulate Equation (2.7)

$$\frac{i(E)}{F} = k'_{ox}(E) c_R^s - k'_{rd}(E) c_O^s \tag{2.7}$$

If we now assume that the electrode is at the null potential, E_n, and hence $i = 0$, we may assume that the surface concentrations are equal to the bulk concentration. We then get

$$\frac{k'_{rd}(E_n)}{k'_{ox}(E_n)} = \frac{c_R^s}{c_O^s} \tag{2.8}$$

This result is useful if we look at the Nernst equation at the null potential

$$E_n = E^{o\prime} - \frac{RT}{F} \ln\left(\frac{c_R^s}{c_O^s}\right) \tag{2.9}$$

which can, by the help of Equation (2.8), be rewritten as

$$E_n = E^{o\prime} - \frac{RT}{F}\ln\left(\frac{k'_{rd}(E_n)}{k'_{ox}(E_n)}\right) \tag{2.10}$$

Since any potential in principle can be defined as the null potential by varying the bulk concentrations, we can write Equation (2.10) as

$$E = E^{o\prime} - \frac{RT}{F}\ln\left(\frac{k'_{rd}(E)}{k'_{ox}(E)}\right) \tag{2.11}$$

where we now state that the equation holds for all values of E. We can see that when E is the formal potential, $E^{o\prime}$, the two rate constants are equal. In this special case, we define a formal rate constant

$$k^{o\prime} = k'_{rd}\left(E^{o\prime}\right) = k'_{ox}\left(E^{o\prime}\right) \tag{2.12}$$

If the formal rate constant is implemented in Equation (2.11), it can be rearranged into

$$\frac{RT}{F}\ln\left(\frac{k^{o\prime}}{k'_{rd}}\right) + \frac{RT}{F}\ln\left(\frac{k^{o\prime}}{k'_{ox}}\right) = E - E^{o\prime} \tag{2.13}$$

where we have skipped the (E) suffixes to make the next expressions simpler.

Equation (2.13) is now differentiated with respect to E

$$\frac{RT}{F}\frac{d}{dE}\ln\left(\frac{k^{o\prime}}{k'_{rd}}\right) + \frac{RT}{F}\frac{d}{dE}\ln\left(\frac{k^{o\prime}}{k'_{ox}}\right) = 1 \tag{2.14}$$

from which we define the reductive transfer coefficient, α, and the oxidative transfer coefficient, $(1-\alpha)$, given in Equation (2.15) and (2.16) respectively.

$$\alpha = \frac{RT}{F}\frac{d}{dE}\ln\left(\frac{k^{o\prime}}{k'_{rd}}\right) \tag{2.15}$$

$$1 - \alpha = \frac{RT}{F}\frac{d}{dE}\ln\left(\frac{k^{o\prime}}{k'_{ox}}\right) \tag{2.16}$$

The transfer coefficients in Equation (2.15) and (2.16) are also called charge transfer coefficients or symmetry factors. When integrating these, we obtain expressions for the backward and forward formal reaction rates

$$k'_{rd} = k^{o'} \exp\left(-\frac{\alpha F}{RT}\left(E - E^{o'}\right)\right) \tag{2.17}$$

$$k'_{ox} = k^{o'} \exp\left(\frac{(1-\alpha) F}{RT}\left(E - E^{o'}\right)\right) \tag{2.18}$$

If we now introduce the equations for the rate constants to Equation (2.7), we arrive at one version of the Butler-Volmer equation

$$i = Fk^{o'}\left[-c_O^s \exp\left(\frac{-\alpha F}{RT}\left(E - E^{o'}\right)\right) + c_R^s \exp\left(\frac{(1-\alpha) F}{RT}\left(E - E^{o'}\right)\right)\right] \tag{2.19}$$

which is typically expressed with the exchange current density, $i_0 = Fk^{o'}\left(c_R^b\right)^{\alpha}\left(c_O^b\right)^{1-\alpha}$, so that we have

$$i = i_0\left[-\frac{c_O^s}{c_O^b}\exp\left(\frac{-\alpha F}{RT}(E - E_n)\right) + \frac{c_R^s}{c_R^b}\exp\left(\frac{(1-\alpha) F}{RT}(E - E_n)\right)\right] \tag{2.20}$$

The above versions of the Butler-Volmer equation states that the current density is dependent on the concentrations of reactants and products at the electrode surface. In a situation where transport polarisations are negligible, such as when using a rotating disk electrode (RDE), the surface concentrations can be set to be equal. This results in a simpler and important expression of the Butler-Volmer equation.

$$i = i_0\left[-\exp\left(\frac{-\alpha F}{RT}(E - E_n)\right) + \exp\left(\frac{(1-\alpha) F}{RT}(E - E_n)\right)\right] \tag{2.21}$$

Finally, we recognise $E - E_n$ as the overpotential and simplify Equation (2.21) even further

$$i = i_0\left[-\exp\left(\frac{-\alpha F}{RT}\eta\right) + \exp\left(\frac{(1-\alpha) F}{RT}\eta\right)\right] \tag{2.22}$$

2.1.2 The Tafel Equation

Tafel analysis is a powerful technique for evaluating the reaction mechanisms and kinetics at electrodes. It is being used extensively as one of the primary techniques to study electrocatalysts for water electrolysis [33]. We can understand the Tafel slope as a measure of how fast the current density can increase with increasing overpotential. Therefore, a lower Tafel slope is in general indicative of faster electrocatalytic kinetics of the electrode reaction.

To understand how the theory behind the Tafel approach can give us mechanistic and kinetic information, we will derive the Tafel equation from the Butler-Volmer equation in Equation (2.22). From a broad perspective, Tafel analysis begins with the procedure where the logarithmic current is viewed as a function of the applied potential. Normally, the analysis is done in regions where cathodic and anodic currents dominate separately. In this work, we only investigate the anodic behaviour of electrocatalysts during the OER. The overpotentials will therefore be large and positive and the term associated with the cathodic current in Equation (2.22) can be assumed negligible, as it goes to zero. Approaching Equation (2.22) with this, we thus get

$$\log(i) = \log(i_0) + \frac{\alpha z F}{2.303RT}\eta \tag{2.23}$$

where z is the number of electrons taking part in the reaction. Equation (2.23) is typically rewritten to fit the important Tafel equation in Equation (2.24)

$$\eta = a + b\log(i) \tag{2.24}$$

$$a = \frac{2.303RT}{\alpha z F}\log(i_0) \tag{2.25}$$

$$b = \frac{2.303RT}{\alpha z F} \tag{2.26}$$

where a contains the exchange current density and b is the Tafel slope. The exchange current density is hence found by extrapolating the linear Tafel region to $\eta = 0$.

We now know that a Tafel plot is a plot of η vs. $\log(i)$. We find the Tafel slope, with units of mV dec^{-1}, from the slope of the linear region in a Tafel plot. A criterion is usually that the linear region should span at least two orders of current magnitude [33]. However, this is not always strictly followed in literature, where also milder criterions are being used [34].

To interpret the Tafel slope of a multiple-electron reaction such as the OER, it is important to know how we can connect it to theory. Taking Equation (2.26), we see that the only variables are the transfer coefficient, α, and the number of electrons partaking in the reaction, z. We will assume that the OER proceeds through steps with only one electron transfer and hence, $z = 1$. In single-electron transfer reactions, the transfer coefficient is often assumed to have the value 0.5. From Equation (2.26), this would result in a Tafel slope of 120 mV dec^{-1}. This is however not a good assumption in order to precisely describe the multiple-electron reaction that is the OER.

To fit reactions with multiple-electron transfers, the transfer coefficient can be expressed by Equation (2.27)

$$\alpha_a = \frac{n_b}{\nu} + n_r\beta \tag{2.27}$$

where n_b is the number if electrons that transfers back to the electrode before the rate determining step, ν is the number of rate determining steps that take place in the overall reaction, n_r is the number of electrons participating in the rate determining step and β is the symmetry factor, assumed to take the value 0.5 [13]. It can be noted that the transfer coefficient of reaction steps without an electron transfer can also be expressed with Equation (2.27) if n_r is set to be 0. It is therefore useful in order to calculate theoretical Tafel slopes of steps in a proposed OER mechanism.

2.2 Reaction Paths and Mechanisms

This section presents some of the theoretical mechanisms by which the oxygen evolution reaction is suggested to happen. Some of the most widely accepted reaction paths with associated Tafel slopes are presented.

2.2.1 Adsorbate Evolution Mechanism (AEM)

A thorough analysis of the Tafel slopes of electrocatalysts during OER is important in obtaining information about the rate determining steps (rds). In OER electrocatalysis, the reactions are most commonly believed to happen at catalytically active transition metal sites, M. If the reactions happen solely on these M-sites with the electrolyte species ($OH^-/H^+/H_2O$) being the only reactants, it is called an adsorbate evolution mechanism (AEM). This is different from mechanisms where i.e. lattice oxygen is participating in the reactions steps and mediate the oxygen evolution.

As is depicted in Figure 2.1, the OER is expected to progress by two main AEM mechanisms [13]. The first is through the formation of two adjacent oxo (M-O) intermediates, where the oxygen atoms then associate to molecular oxygen (green path). The second is by the formation of peroxide (M-OOH) intermediates, which then decompose to release oxygen gas (black path). The red and blue arrows gives the reactants and products in alkaline and acidic environments respectively.

The two main reaction mechanisms in Figure 2.1 have several proposed reaction paths. A couple of these are summarised in Table 2.1, where the left and right columns describe the green and black mechanisms respectively. The reaction paths of the two mechanisms have in general the same initial steps, however they change after the first M-O bond is formed. It is also seen that the Tafel slopes decrease as the rate determining step moves closer to the final step where O_2 gas is evolved. This is why lower Tafel slopes are associated with higher electrocatalyst activity.

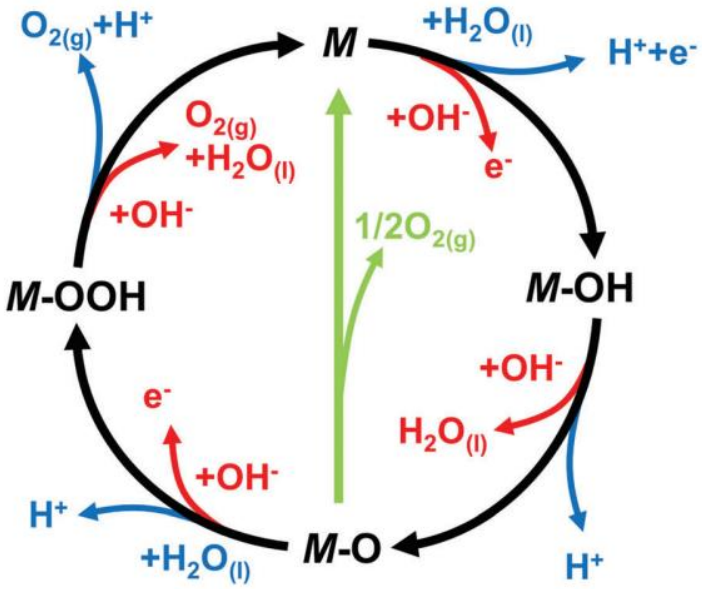

Figure 2.1: Schematic illustration of AEMs for the OER in alkaline (red) and acidic (blue) environment. It can be seen how the OER progresses via the formation of peroxide (M-OOH) intermediates (black path) or through the association of two adjacent oxo (M-O) intermediates (green path) [13].

Table 2.1: Proposed reaction paths from literature for the OER in alkaline solution. Paths in the left column are associated with oxygen evolution by the reaction of two oxy (M-O) intermediates on two adjacent sites. Paths in the right column are associated with OER happening through terminal peroxide groups. The table was adapted from [13].

OER paths with evolution through the reaction of two adjacent oxy (M-O) intermediates		**OER paths with evolution through terminal peroxide group**	
Path	Tafel slope (mv dec^{-1})	Path	Tafel slope (mv dec^{-1})
(1) The electrochemical oxide path		**(3) Doyle and Lyons path**	
$M + OH^- \rightarrow MOH + e^-$	120 mV dec^{-1}	$MOH_2 + OH^- \rightarrow MOH^- + H_2O$	-
$MOH + OH^- \rightarrow MO + H_2O + e^-$	40 mV dec^{-1}	$MOH^- \rightarrow MOH + e^-$	120 mV dec^{-1}
$2MO \rightarrow 2M + O_2$	15 mV dec^{-1}	$MOH + OH^- \rightarrow MO^- + H_2O$	60 mV dec^{-1}
		$MO^- \rightarrow MO + e^-$	120 mV dec^{-1}
		$MO + OH^- \rightarrow MO_2H + e^-$	40 mV dec^{-1}
		$MO_2H + OH^- \rightarrow MO_2 + H_2O + e^-$	40 mV dec^{-1}
		$MO_2 + OH^- \rightarrow MOH^- + O_2$	-
(2) Krasil'shchikov path		**(4) Shinagawa path**	
$M + OH^- \rightarrow MOH + e^-$	120 mV dec^{-1}	$MOH^- \rightarrow MOH + e^-$	120 mV dec^{-1}
$MOH + OH^- \rightarrow MO^- + H_2O$	60 mV dec^{-1}	$MOH + OH^- \rightarrow MO + H_2O + e^-$	30, 120 mV dec^{-1}
$MO^- \rightarrow MO + e^-$	40 mV dec^{-1}	$MO + OH^- \rightarrow MO_2H + e^-$	21, 40, 120 mV dec^{-1}
$2MO \rightarrow 2M + O_2$	15 mV dec^{-1}	$MO_2H + OH^- \rightarrow MO_2^- + H_2O$	22, 30, 60, 120 mV dec^{-1}
		$MO_2^- \rightarrow M + O_2 + e^-$	22, 120 or 40, 120 mV dec^{-1}

2.2.2 Lattice Oxygen-Participated Mechanism (LOM)

The AEMs proposed above all have reaction steps happening through redox reactions on a metal cation site, M, with the electrolyte as the only reactant. However, it has been shown that oxide electrocatalysts can also perform OER through participation from the lattice oxygen. This mechanism, first mentioned by Rong et al., is named the lattice oxygen(-participated) mechanism (LOM) [35-37]. The LOM was initially introduced because density functional theory (DFT) calculations showed that it agreed better with the experimental data from high activity electrocatalysts such as $LaNiO_3$ and $La_{1-x}Sr_xBO_3$ (B = transition metal).

Figure 2.2 shows the difference between the AEM and LOM in alkaline environment on a Co-based catalyst. There are two important aspects that makes LOM deviate from the AEM. Firstly, LOM needs participation from lattice oxygen to mediate the OER. Secondly, it does not change the oxidation state of the transition metal (TM) cation. The latter is explained by the fact that the lattice oxygen is oxidised instead of the Co^{3+} site, leaving an oxygen vacancy and a superoxide ion (O_2^-) intermediate. To understand this, the partial density of states (PDOS) below each mechanism in Figure 2.2 can be of help. During AEM, the $3d$ band of the TM cation lies above the O $2p$ band and hence only the TM cation can undergo oxidation to a higher valence. On the other hand, catalysts showing LOM have a larger degree of TM $3d$ to O $2p$

covalency, as can be seen from the larger overlap in the PDOS. This makes the oxidation of the lattice oxygen more feasible, upon which a ligand hole is created as can be seen by the 1E (E = electrochemical) transition in the PDOS. In the 1C (C = chemical) transition, the lattice oxygen is transferred to the adsorbed intermediate. This results in the PDOS of the 2*p* band of the adsorbate and lattice oxygen to increase and decrease respectively.

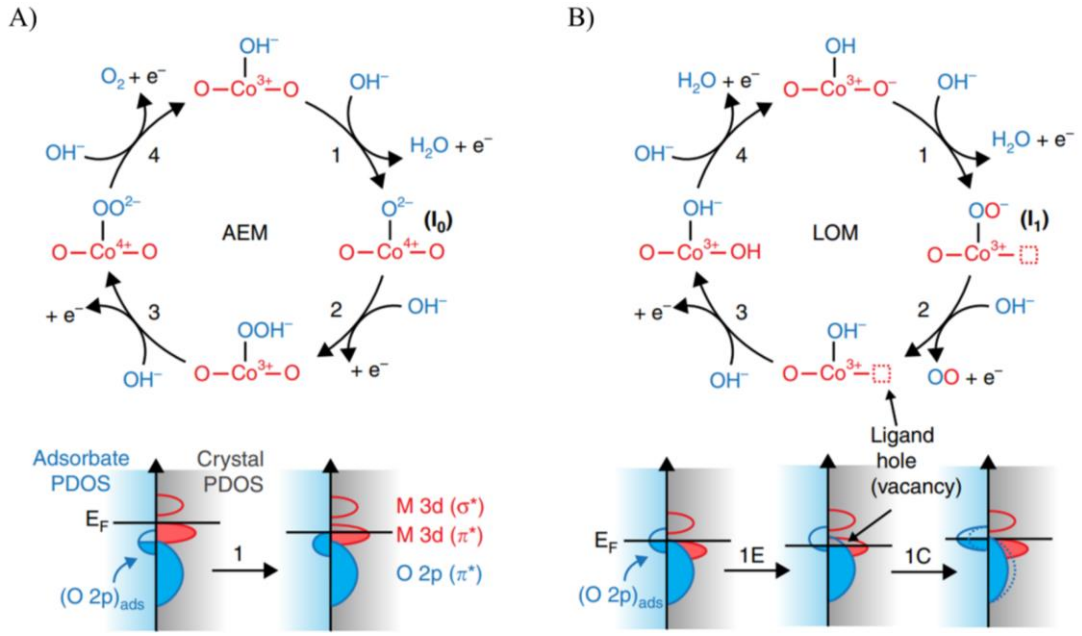

*Figure 2.2: The steps in the **A)** AEM and **B)** LOM during oxygen evolution in alkaline solution. Lattice species are given in red and electrolyte species are given in blue. Partial density of states (PDOS) of the two mechanisms are given below [37].*

It has been found that the mechanism by which the OER is mediated (AEM or LOM), has a significant impact on the observed stability of the catalyst. Specifically, catalysts with an increasing LOM contribution during the OER was found to exhibit a lower bulk stability [35, 37]. This can be understood qualitatively by the difference between the steps in the AEM and LOM. In the latter, the oxygen gas is evolved in step 2 followed by a regeneration of the lattice oxygen from the electrolyte, making the participation from the lattice oxygen reversible. However, if the regeneration of the lattice oxygen (step 3 and 4) happens slower than the release of lattice oxygen (step 1 and 2), the initial surface structure of the electrocatalyst will be lost over time.

The loss of lattice oxygen leaves oxygen vacancies in the catalysts surface. If these are not filled through step 3 and 4, they have to be compensated for by another mechanism. One such type of charge compensation can be the leaching of cations into the electrolyte. In this process, an

amorphisation of the surface is also common [38]. This leads to a change in the pristine atomic structure of the catalyst and can have a detrimental effect on its stability.

2.3 Defect Chemistry

Today, it is common knowledge among materials scientists that no inorganic compound is perfect with respect to crystal structure and chemical stoichiometry above 0 K temperature. This knowledge has made it possible to understand how inorganic compounds behave upon i.e. doping, exposure to different atmospheres and with changing temperature. In oxygen evolution catalysis, knowing the defect chemistry of the catalyst can be key to understanding its performance. Some simple defect chemistry considerations are therefore presented in this section by discussing acceptor doping of $LaCoO_3$ (LC) with Ba^{2+}. LC is chosen as example material because it exhibits the perovskite structure and the valence of the A- and B-site cations are similar to those found in BGLC587.

2.3.1 Acceptor Doped $LaCoO_{3-\delta}$

The material $LaCoO_{3-\delta}$ is well known to exhibit inherent oxygen non-stoichiometry. However, if no predominance is assumed and $LaCoO_{3-\delta}$ is acceptor doped by substitution of La^{3+} with a lower valent cation such as Ba^{2+}, there are two general outcomes. The first is that the acceptor doping is compensated by an increase in the oxygen vacancy concentration, $[v_O^{\bullet\bullet}]$, which is expressed by the defect reaction in Equation (2.28). The second outcome is that electron holes are the charge compensating defects, which is presented in the defect reaction in Equation (2.29).

$$2BaO + 2La_{La}^{X} + O_O^{X} \leftrightharpoons 2Ba'_{La} + v_O^{\bullet\bullet} + La_2O_3 \tag{2.28}$$

$$2BaO + 2La_{La}^{X} + \frac{1}{2}O_2(g) \leftrightharpoons 2Ba'_{La} + 2h^{\bullet} + La_2O_3 \tag{2.29}$$

$$[Ba'_{La}] = 2[v_O^{\bullet\bullet}] + h^{\bullet} \tag{2.30}$$

Equation (2.28) and (2.29) are two fundamentally different defect reactions, which will change the electrochemical properties of $LaCoO_{3-\delta}$ accordingly. Hence, it is very important to know whether the former or latter is happening. One simple way of knowing this is to measure the change in the value of δ. If δ increases, Equation (2.28) is dominating, whereas if δ decreases Equation (2.29) has the most influence. This we see from the charge neutrality condition in Equation (2.30).

Varying the type of B-site transition metal in a material such as $LaCoO_{3-\delta}$ may also have an effect on how the charge compensation occurs. This can be understood to be a consequence of the electronegativity of transition metals and their ability to bind oxygen in the lattice. In example, Lim et al. found that Fe substitution in $PrBa_{0.8}Ca_{0.2}Co_2O_{6-\delta}$ (PBCO) resulted in a higher O content, where δ increased from 5.75 to 5.97 [39]. This is close to a stoichiometric condition with $\delta = 0$. Since PBCO is an acceptor doped material, the higher oxygen content resulting from Fe-doping will therefore increase the concentration of electron holes as charge compensating defects through Equation (2.29).

In evaluating oxygen evolution catalysts (OECs), the oxidation state of the transition metal cations are mentioned as activity descriptors [30]. If holes are the charge compensating defect in acceptor doped perovskite materials, these may be found localised at the B-site transition metal atoms resulting in a higher valency of these. Equation (2.31) gives the defect reaction for electron holes localised on Co cations.

$$2BaO + 2La_{La}^{x} + 2Co_{Co}^{x} + \frac{1}{2}O_2(g) \leftrightharpoons 2Ba_{La}' + 2Co_{Co}^{\bullet} + La_2O_3 \tag{2.31}$$

The main difference between Equation (2.29) and (2.31) is that in the former, the electron holes are delocalised and may contribute to increased conductivity, whereas in the latter they are bonded to a specific transition metal, changing the redox properties of this.

2.4 Benchmarking the OER

2.4.1 Overpotentials

There is no real system in which a net electrochemical reaction happens at the potential predicted thermodynamically. The introduction of overpotential is hence very relevant when studying electrocatalysis of such reactions. The total overpotential of a reaction is given as the sum of the Ohmic, transport and kinetic overpotentials as in Equation (2.32).

$$\eta = \eta_{Ohmic} + \eta_{trans} + \eta_{kin} \tag{2.32}$$

The Ohmic contribution is associated with the so called uncompensated resistance, R_u, typically also called solution resistance, R_s. This resistance originates from the interface between electrochemical components such as the electrolyte and the electrodes. The potential drop due to this uncompensated resistance is often called *iR*-drop and can in most cases be compensated for by measuring its value with electrochemical impedance spectroscopy (EIS). The second

contribution is a consequence of a change in the concentration of reactants and products at the surface of the electrodes. All electrochemical reactions rely on a constant supply of reactants as well as removal of products. If the transport of these is not sufficient, a reaction may be so-called mass transport limited. This contribution to the overpotential is most often overcome by forcing convection in the system.

If both of the two abovementioned contributions to the overpotential are decoupled and avoided, we are left with only the kinetic overpotential. This is a material specific overpotential dependant on the electrode's ability to catalyse the desired reaction. It is quite common when investigating overpotentials for the OER to both *iR*-compensate and make sure the electrochemical cell is free from mass transport limitations. The reported overpotentials of OECs are therefore often equal to η_{kin} and it is common to report them at a current density of 10 mA cm^{-2}_{geo}.

Tafel slopes of electrocatalysts are almost always provided as activity descriptor along with the overpotentials. The Tafel slopes can be acquired by either linear sweep voltammetry (LSV), cyclic voltammetry (CV), electrochemical impedance spectroscopy (EIS), chronopotentiometry (CP) or chronoamperometry (CA). However, the values obtained in these methods can vary quite a lot if it is not taken care to obtain steady-state conditions [33]. Another important fact is that all the methods above, except for EIS, do not give Tafel slopes mirroring the intrinsic activity of the material. This is because voltammetry and potentiometry/amperometry will always have contribution by series resistance from different hetero-junctions in the electrochemical cell. With EIS, these contributions can be decoupled and one can extract a Tafel slope describing the true inherent kinetics of the electrocatalyst [33].

2.4.2 Current Normalisation

The current response that arises when applying an overpotential is not very useful if we want to compare the activity of different electrode materials. The most widely reported type of current normalisation is with respect to the geometrical surface area of the electrode. However, it has become more and more popular to use other properties such as the electrochemically active surface area (ECSA) and Brunauer-Emmet-Teller (BET) surface area when normalising. Typically, normalised current is benchmarked at a defined potential such as 0.4 V vs. RHE, but the whole i-E curve can also be given.

Geometrical Surface Area

Even though it has been used widely, OER current normalised with geometrical surface area is not without demerits. In most cases the surface area of the catalyst material is not equal to the nominal electrode area. The major drawback of this method is therefore that it does not reflect the intrinsic activity of the catalyst material. In principle, this means that one can observe very different current densities in one material depending on its micro- and nanostructure. Unless the material has a very well defined surface, this method can lead to wrongly determination of the activity.

Electrochemically Active Surface Area (ECSA)

A normalisation method that in theory may give the intrinsic activity of an electrocatalyst is normalisation with respect to the ECSA. It is often called specific activity, i_s, (with units A cm^{-2}_{ECSA}) and compared to normalisation through the geometrical surface area, this method accounts for the catalyst loading on the electrode [14]. The ECSA can be found with several methods by measuring the double layer capacitance of the electrode, C_{dl}. Two common methods are based on measuring the double layer capacitance with cyclic voltammetry or EIS in a potential region free from Faradaic current. This region may also be called capacitive or non-Faradaic. By using the double layer capacitance found from these measurements, ECSA provides a means of finding the real surface area that is in contract with the electrolyte. However, different methods may give very different capacitance values and lead to possible errors [14]. It has also been pointed out that the ECSA is not always easily determined and problems regarding reproducibility can be encountered [33]. Therefore, it is not the most widely used normalisation method.

Brunauer-Emmet-Teller (BET) Surface Area

Another method of current normalisation is to normalise with the BET surface area (with units A cm^{-2}_{oxide}). Like ECSA, this method is loading-sensitive and has become quite popular because of the ease by which one can measure the surface area of an electrocatalyst. Even though it is often reported as specific activity, it does not accurately give the intrinsic activity of the electrocatalyst. This is because the adsorption sites during a BET measurement are not necessarily active during OER and it is probable that an overestimation is made. Still, it is better than normalisation with geometrical surface area and quite suitable for porous materials.

Mass Activity

Current normalised with respect to catalyst loading is called mass activity (units A g^{-1}). This method accounts directly for the catalyst loading, but does not give any information about the intrinsic activity. It is useful of one wants to evaluate the effect of different catalyst loading of the same material, however it comes short if one wants to compare results with literature values. This drawback originates from the fact that the mass activity does not account for effects from particle size, density, morphology and topography of a material [14].

2.4.3 Electrochemical Impedance Spectroscopy

Electrochemical impedance spectroscopy (EIS) is a powerful technique when trying to learn how the different features of an electrode (or electrochemical cell) contributes to the overall performance of a chemical process. Impedance, Z, is defined as a complex number as shown in Equation (2.33)

$$Z = R + jX \tag{2.33}$$

where R and X are called resistance and reactance with units Ω and $j = \sqrt{-1}$. The impedance is measured by applying a sinusoidal AC voltage with a range of frequencies around a certain DC potential and measuring the AC current response. The impedance is then found by dividing the measured AC voltage by the current response, giving rise to its complex nature.

The power of EIS comes from the possibility to decouple contributions from different parts and processes an electrochemical system and find their intrinsic properties. Plotting -X vs. R gives rise to a Nyquist plot (exemplified to the right in Figure 2.3) and is commonly used when evaluating impedance data. EIS analysis is typically done by fitting the impedance data to an equivalent circuit with circuit elements following mathematical functions. One such circuit often deployed in EIS analysis of OER electrocatalysts is the Randles circuit.

This circuit has one resistance, R_s, typically assigned to wires, connections and the electrolyte, with a parallel R||C element in series. The capacitator in the R||C element is often expressed through a constant phase element (CPE), to account for the mixed capacitive and resistive behaviour of the electrode surface. In some cases, it can be practical to extend the Randles circuit in order to comprehend all the features of an EIS spectra. This is shown by the equivalent circuit to the left in Figure 2.3, where there are two R||C elements in series with the solution resistance R_s. This circuit is often used to deal with surface passivation layers on electrodes

[40] and adds a smaller semicircle to the Nyquist plot at higher frequencies, as seen to the right in Figure 2.3.

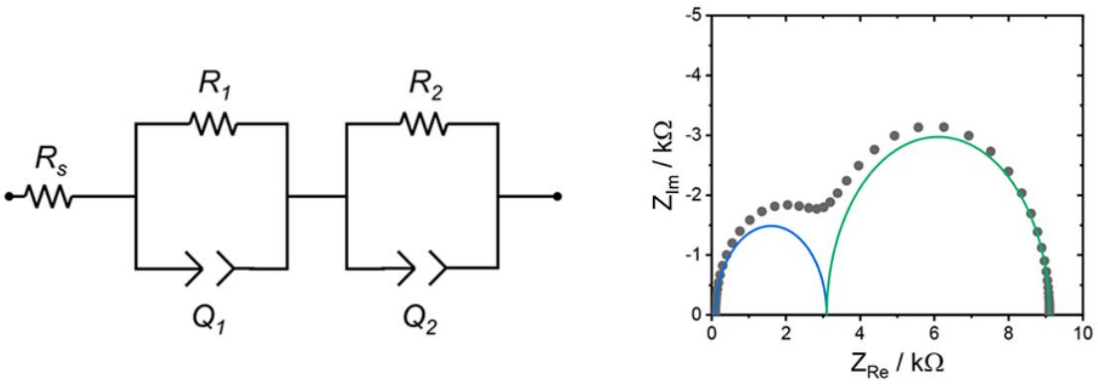

Figure 2.3: ***Left:*** *An extended Randles circuit with the solution resistance, R_s, in series with two parallel R||C elements.* ***Right:*** *The corresponding Nyquist plot of the extended Randles circuit showing two semicircles attributed to an electrode surface passivation layer and the electrode material [40].*

Charge Transfer Resistance

One of the intrinsic OER activity descriptors that can be extracted from EIS is the charge transfer resistance, R_{ct}. This is the resistance associated with the Faradaic transfer of charge across the interfaces in an electrochemical system. As an example, this can be the transfer of electrons or holes from the electrode surface to the species in the electrolyte. Since the charge transfer is a Faradaic process, it is only the resistors (R_1 and R_2) in the equivalent circuit in Figure 2.3 that contribute to R_{ct}. To find the charge transfer resistance in such a system, we only have to add the resistance of the resistors together, since they are connected in series. This is shown in Equation (2.34). By extracting the charge transfer resistance in this way with EIS, one can exclude all the other resistances not attributed to the catalytic process on the electrode.

$$R_{ct} = R_1 + R_2 \tag{2.34}$$

The $R_{ct}C_t$ Product as OER Descriptor

Papaderakis et al. reported a method for benchmarking the intrinsic and surface area normalised OER activity of electrocatalysts by calculating the $R_{ct}C_t$ product [41]. This product represents the time constant, τ, of the electrochemical reaction (units s) and the lower it is, the faster the kinetics.

The idea behind this descriptor is that the value of the charge transfer resistance, R_{ct}, gives the intrinsic activity, while the total capacitance, C_t, normalises this activity in a similar way to what has been discussed earlier for the ECSA. However, the C_t of particulate electrocatalysts was found to be hard to estimate during OER. For materials with such morphology, it can therefore be better to use the capacitance measured outside the OER region (non-Faradiac region).

The drawback of using a capacitance derived outside the OER potential region is that it might not reflect the true capacitance during oxygen evolution. Some electrodes may suffer from pore clogging from evolved gas, which blocks the active sites on the surface. This will in principle decrease the capacitance and invalidate the method. It can therefore be interesting to use the double layer capacitance, C_{dl}, derived from EIS measurements in the OER potential region instead of C_t. Even though this has been done before [26, 27], it is not an established technique and experimental validation should be done.

3 Literature

3.1 Electrocatalyst Requisites

Before discussing advances from the literature on OER catalysts, it is important to know the properties that are required in order for them to have high performance as electrode material. In 1984, Trasatti stated eight requisites for electrode materials which is to be used for technological applications [42], which were

(1) High surface area
(2) High electrical conduction
(3) Good electrocatalytic properties
(4) Long-term mechanical and chemical stability at the support/active layer and at the active layer/solution interface
(5) Minimized gas bubble problems
(6) Enhanced selectivity
(7) Availability and cost
(8) Health safety

Nearly 40 years later, these point are just as important as they were back then. In terms of an OER electrocatalyst, the surface area (1), the catalytic activity (3), stability (4) and cost (7), are the four most frequently evaluated requisites. A typical consequence of point 1 is an increased exposure of active sites and hence high activity. This has led to increasing interest in developing nanostructured catalysts such as nanosheets, nanowires (NWs) and nanoparticles (NPs) with considerably higher surface area [43, 44].

Usually, the catalytic activity (3) and stability (4) are inversely proportional to each other and one must find a compromise between these [45]. This is exemplified in Figure 3.1 where the OER activity of some noble metal oxides are compared to their stability to withstand dissolution in the electrolyte.

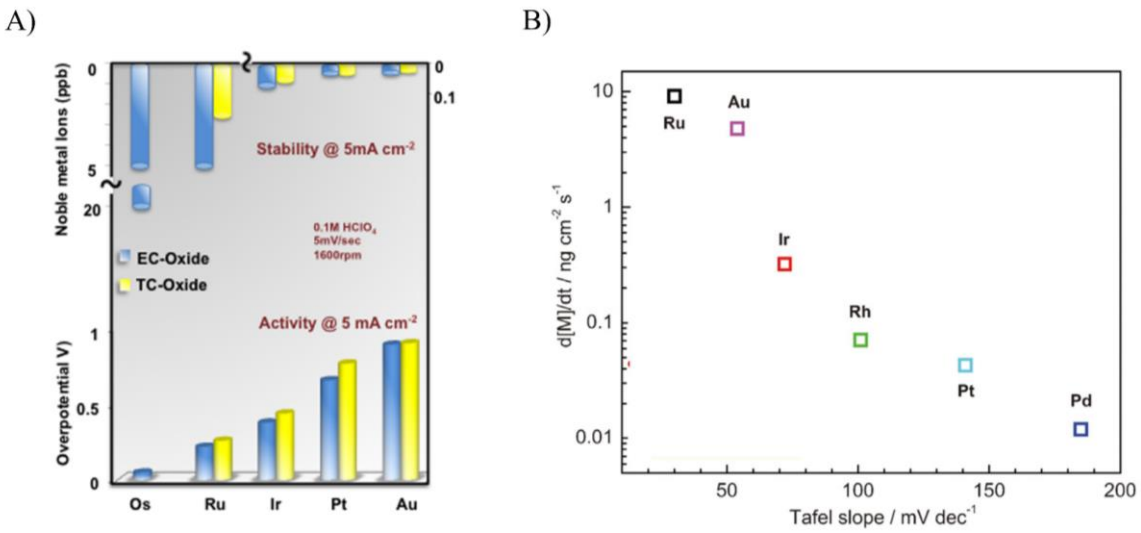

Figure 3.1: Relation between the stability and OER activity of some noble metal oxide electrocatalysts. ***A)****: Shows a clear inverse relation between the stability and OER activity of noble metal oxides synthesised by thermal (TC) and electrochemical (EC) methods [46].* ***B)****: The dissolution of noble metal electrocatalysts as a function of the Tafel slope. It can be observed that higher activity results in lower stability and vice versa [47].*

The abundance and cost (7) is naturally a very important aspect that needs to be considered for catalysts meant for large-scale industrialisation. The most commonly used electrocatalysts based on noble metals such as Ir, Ru or Pt have both low abundance and are associated with high cost. This is one of the main reasons why a lot of research is being put into finding earth-abundant electrocatalysts [48, 49].

3.2 OER Electrocatalysts

3.2.1 IrO_2 and RuO_2

As of today, iridium/ruthenium oxides are regarded as benchmark electrocatalysts for OER due to their excellent catalytic activity in both acidic and alkaline environments [13]. The Ir-/Ru-oxides typically exhibit low overpotentials and low Tafel slopes. However, it is observed that the activity of these may vary depending on electrolyte concentration, morphology and from work to work. This is emphasised in Table 3.1 presenting a selection of reported overpotentials, Tafel slopes and surface areas of rutile IrO_2 and RuO_2.

Table 3.1: OER activity of rutile IrO_2 and RuO_2 reported in literature. From left: overpotentials at 10 mA cm^{-2}_{geo}, Tafel slopes, BET surface areas, electrolyte used and references.

Structure and morphology	η_{10} (mV)	Tafel slope (mv dec^{-1})	Surface area (m^2 g^{-1})	Electrolyte	Ref.
IrO_2					
Rutile, powder	450	83	142 (BET)	0.1 M KOH	[50]
Rutile, powder	350	89	140 (BET)	0.1 M KOH	[51]
Rutile, powder	330	76	n.a.	1.0 M KOH	[52]
Rutile, powder	487	72	n.a.	1.0 M NaOH	[27]
RuO_2					
Rutile, powder	310	72	51 (BET)	1.0 M KOH	[22]
Rutile, powder	370	73.7	n.a.	1.0 M KOH	[53]
Rutile, powder	310	60.7	77 (BET)	1.0 M KOH	[53]
Rutile, NWs	260	56	n.a.	0.5 M KOH	[54]

Even though IrO_2 and RuO_2 show favourable activity towards the OER, their high cost and limited abundance compared to i.e. transition metals have impeded the large-scale deployment of these in industry. Another reported drawback of these noble metal oxides is the low stability in acidic and alkaline environment during OER, caused by the oxidation of IrO_2 and RuO_2 to IrO_3 and RuO_4 which may dissolve into the electrolyte [55, 56]. In general, dissolution is more prominent in alkaline solutions, in which IrO_2 is considered the most stable and RuO_2 the most active [57].

The difference in stability and activity of IrO_2 and RuO_2 has led to synthesis of mixed oxides of the type $Ir_xRu_{1-x}O_2$ in order to find the optimal stability vs. activity. Lyons and Floquet [58] found that a 1:1 ratio of Ir and Ru gave the highest activity in both alkaline and acidic solutions. Kötz and Stucki [59] found that introducing Ir in RuO_2 improved the stability during OER and that a 20% Ir content reduced the corrosion rate to 4% of that of the pristine RuO_2. They also saw from the results that a 20-50% Ir content gave the most optimal catalysts performance.

3.2.2 Oxide Perovskites

Another class of materials, which have been a popular choice as electrocatalysts for the OER during the last decades, are those exhibiting the perovskite structure. The interest in these comes from their highly tuneable (electro-)chemical and physiochemical properties originating from their great versatility in elemental composition. Table 3.2 presents the OER activity of a selection of perovskite oxides from literature compared to state-of-the-art materials such as IrO_2, RuO_2 and $Ba_{0.5}Sr_{0.5}Co_{0.8}Fe_{0.2}O_{3-\delta}$ (BSCF82) in alkaline environment.

Table 3.2: OER activity of some electrocatalysts in alkaline environment obtained from literature. From left: catalyst material, overpotential at 10 mA cm^{-2}_{geo}, Tafel slope, specific activity (i_s) at 0.4V overpotential (normalised by the specific surface area, A_s), stability, catalyst loading on substrate, electrolyte used and references.

Electrocatalyst	η_{10} (mV)	Tafel slope (mv dec^{-1})	$i_{s,@0.4\ V}$ (mA cm_{ox}^{-2})	Stability	Loading/ Substrate (mg cm^{-2})	Electrolyte	Ref.
Benchmark ECs							
IrO_2	350	89	0.04*	10h, 16.1% degrad.†	0.320, GC	0.1 M KOH	[51]
RuO_2	310	72	0.014** η = 0.25 V	10h, 12.5% degradation†	0.198, GC	1.0 M KOH	[22]
$Ba_{0.5}Sr_{0.5}Co_{0.8}Fe_{0.2}O_{3-\delta}$ (BSCF82)	320 $@\eta_{2.5}$	60	40⁑	n.a.	0.250, GC	0.1 M KOH	[31]
$Ba_{0.5}Sr_{0.5}Co_{0.8}Fe_{0.2}O_{3-\delta}$ (BSCF82)	500	129	0.8*	n.a.	0.639, GC	0.1 M KOH	[60]
Perovskite type ECs							
$Ba_{0.5}Gd_{0.8}La_{0.7}Co_2O_{6-\delta}$ (BGLC587)	470	78	n.a.	48h, no degradation†	0.280, GC	1.0 M NaOH	[27]
$Ba_4Sr_4(Co_{0.8}Fe_{0.2})_4O_{15}$ (hex-BSCF)	340	47	2* η = 0.35 V	10h, no degradation†	0.232, GC	0.1 M KOH	[61]
$CaCu_3Fe_4O_{12}$	380	51	17*	100 cycles, no degradation	0.250, GC	0.1 M KOH	[62]
$LaCoO_3$	371	97	1.92** η = 0.5 V	30 cycles, 30% degrad.	0.490, GC	1.0 M KOH	[63]
$La_{0.95}FeO_3$	410	48	0.364*	n.a.	0.232, GC	0.1 M KOH	[64]
$Pr_{0.5}Ba_{0.5}CoO_{3-\delta}$	450	82	n.a.	1000 cycles, 59.8% degrad.	0.390, GC	0.1 M KOH	[32]
$Pr_{0.5}Ba_{0.3}Ca_{0.2}CoO_{3-\delta}$	440	73	n.a.	1000 cycles, no degradation	0.390, GC	0.1 M KOH	[32]
$Sr_{0.95}Ce_{0.05}Fe_{0.9}Ni_{0.1}O_{3-\delta}$	340	51	1.6**	30h, no degradation†	0.232, GC	0.1 M KOH	[65]
$SrCo_{0.9}Ti_{0.1}O_{3-\delta}$	510	88	0.63*	10h, no degradation†	0.320, GC	0.1 M KOH	[51]
$SrFeO_3$	480	86	0.16**	< 3h, large degradation†	0.232, GC	0.1 M KOH	[65]
Other ECs							
$LiCoO_{1.8}Cl_{0.2}$	270	55	1** η = 0.25 V	500h, low degradation†	0.198, GC	1.0 M KOH	[22]

* = A_s from BET, ** = A_s from ECSA, ⁑ = A_s from SEM, † = CP/CA at 10 mA cm_{geo}^{-2}

$Ba_{0.5}Sr_{0.5}Co_{0.8}Fe_{0.2}O_{3-\delta}$ (BSCF82)

The oxide perovskite $Ba_{0.5}Sr_{0.5}Co_{0.8}Fe_{0.2}O_{3-\delta}$ (BSCF82) has gained a lot of attention for being the benchmark perovskite electrocatalyst for the OER in alkaline solution. It was first predicted as a highly active OER electrocatalysts by Suntivich et al. from DFT calculations in 2011 [31]. In this study, it was proposed that the intrinsic OER activity of oxide perovskites has a volcano

shaped dependence on the occupancy of the $3d$ e_g electron filling. This volcano plot can be seen in Figure 3.2 A, where the peak OER activity is visible around an e_g occupancy of unity. From this, it was predicted that BSCF82 had high intrinsic OER activity as it lies almost at the top of the volcano plot.

As predicted, electrochemical measurements showed that BSCF82 had both lower Tafel slopes (Figure 3.2 B) and overpotentials during OER. However, the most important activity parameter reported by Suntivich et al. was the specific current density (i_S) of 40 mA cm^{-2}_{oxide} at 0.4 V overpotential. This was much higher than what had been reported for either of the state-of-the-art IrO_2/RuO_2 electrocatalysts and indicated that BSCF82 could outperform these with the right surface area modification. In fact, this was also shown by increasing the surface area with simple ball milling, resulting in an OER overpotential similar to IrO_2.

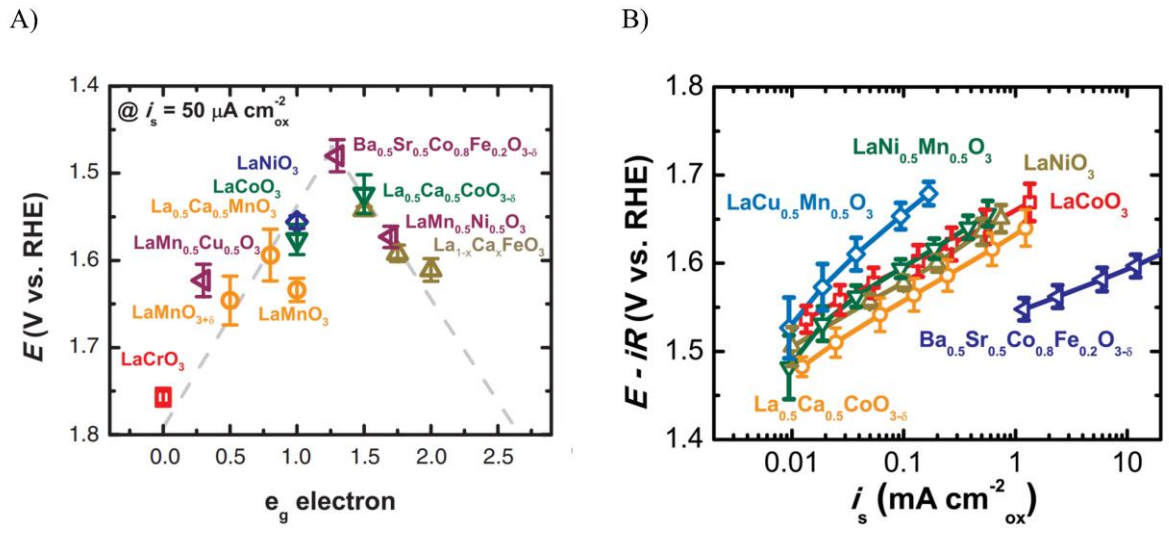

*Figure 3.2: **A)**: Oxygen evolution potential at a specific current density of 50 μA cm^{-2}_{oxide} as a function of the e_e electron occupancy of BSCF82 and other known OER electrocatalysts. **B)**: The Tafel slope of BSCF82 compared to other known electrocatalysts [31].*

Even though BSCF82 was found to exhibit a high OER activity, its stability was not completely understood. May et al. investigated the electrochemical stability of BSCF82 with chronoamperometry and cyclic voltammetry and found no indication of activity degradation from 2 hours CA at 1.6 V vs. RHE or from 100 CV cycles between (1.1 to 1.7 V vs RHE). On the contrary, they saw an increase in the current density with time. May et al. also investigated the structural stability of BSCF82 and other perovskite materials such as $La_{0.4}$ $Sr_{0.6}CoO_{3-\delta}$ (LSC46), $LaCoO_3$ (LC) and $LaMnO_3$ (LM). They found that the surface structure of these

behaved differently after OER cycling [38]. As opposed to the other materials, BSCF82 experienced a surface amorphisation after just a couple of OER cycles (1.1 to 1.7 V vs RHE).

The surface amorphisation of BSCF82 can be seen from the High-Resolution TEM (HRTEM) images in Figure 3.3 A, where the surface of BSCF82 experiences a transition from crystalline to amorphous upon 5 OER cycles, whereas in Figure 3.3 B, $LaCoO_3$ shows no sign of surface amorphisation. The amorphous layer of the BSCF82 particles was found have an average thickness of ~8 nm after 5 OER cycles. Considering this and the fact that that May et al. saw an increased pseudocapacitive current with increasing OER cycles, it was proposed that the surface amorphisation was responsible for the increased OER current by increasing the active surface area.

Investigation with Energy Dispersive X-Ray Spectroscopy (EDS) of the surface of BSCF82 showed that the amorphous layer had a lower A-site cation (Ba, Sr) concentration than the crystalline backbone. It was therefore concluded that BSCF82 experiences leaching of A-site cation during OER cycling and that the surface is enriched with B-site cations.

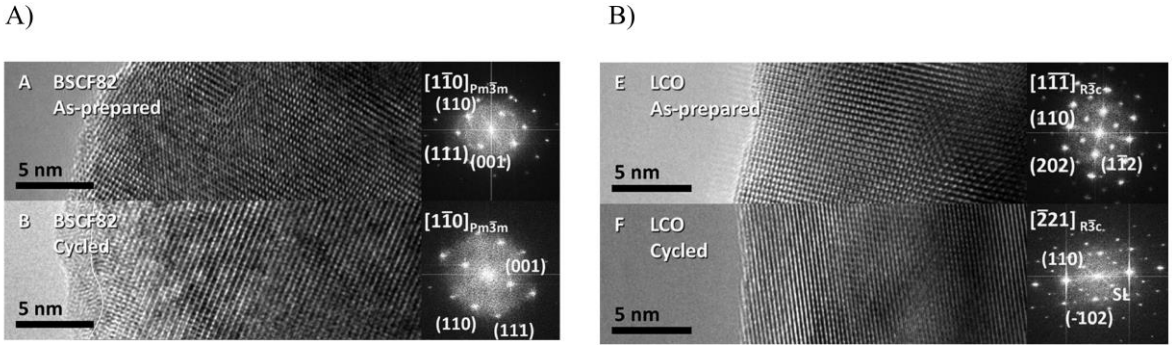

*Figure 3.3: High-Resolution TEM images with fast Fourier transforms (FFTs). **A)**: Surface of as-prepared BSCF82 and after 5 OER cycles. The white dotted line indicates the amorphous region of the cycled surface. **B)**: Surface of as-prepared $LaCoO_3$ and after 5 OER cycles. No surface amorphisation was observed in cycled $LaCoO_3$ [38].*

May et al. hypothesised that the surface amorphisation in BSCF82 is a consequence of its high O p-band centre causing a Fermi level pinning. The pinning of the Fermi level may allow both oxygen anions and metal cations to undergo redox reactions. Specifically, it was suggested that an O p-band centre higher than -2.2 eV (relative to Fermi level) is needed to facilitate amorphisation. This was based on the observation that LSC46, LC and LM with O p-band centres below -2.2 eV did not experience amorphisation, whereas BSCF82, BSCF46 and $SrCo_{0.8}Fe_{0.2}O_{3-\delta}$, with O p-band centres above -2.2 eV did.

$Ba_{0.5}Gd_{0.8}La_{0.7}Co_2O_{6-\delta}$ (BGLC587)

In the group for Electrochemistry at the University of Oslo, oxide perovskites with the general formula $Ba_{1-x}Gd_{0.2-y}La_{x+y}Co_2O_{6-\delta}$ (BGLC) have been investigated as anodes in proton ceramic electrolyser cells (PCECs) over the course of the last 10 years [66-70]. However, it was not until recently that the BGLCs were investigated as electrocatalysts for the OER in alkaline solutions [26, 27]. As a result of this, Zhu et al. found that the composition $Ba_{0.5}Gd_{0.8}La_{0.7}Co_2O_{6-\delta}$ (BGLC587) exhibited high catalytic activity and stability towards the OER, competing with the state-of-the-art IrO_2 [27].

The LSVs in Figure 3.4 A show how BGLC587 compares to other BGLCs and IrO_2 during OER. It was found that BGLC587 reached a current density of 10 mA cm^{-2} at 470 mV overpotential compared to 487 mV for IrO_2. Respective Tafel slopes were found to be 78 mV dec^{-1} and 72 mV dec^{-1} respectively. However, BGLC587 did not exhibit the lowest overpotential of the BGLCs. Still, it was considered the most promising electrocatalyst due to its superior OER stability compared to the other BGLCs. It was seen that after 300 cyclic voltammetry (CV) cycles, BGLC587 showed 6% degradation as compared to 24% and 17% for $BaGd_{0.8}La_{0.2}Co_2O_{6-\delta}$ (BGLC82) and $BaGd_{0.3}La_{0.7}Co_2O_{6-\delta}$ (BGLC37).

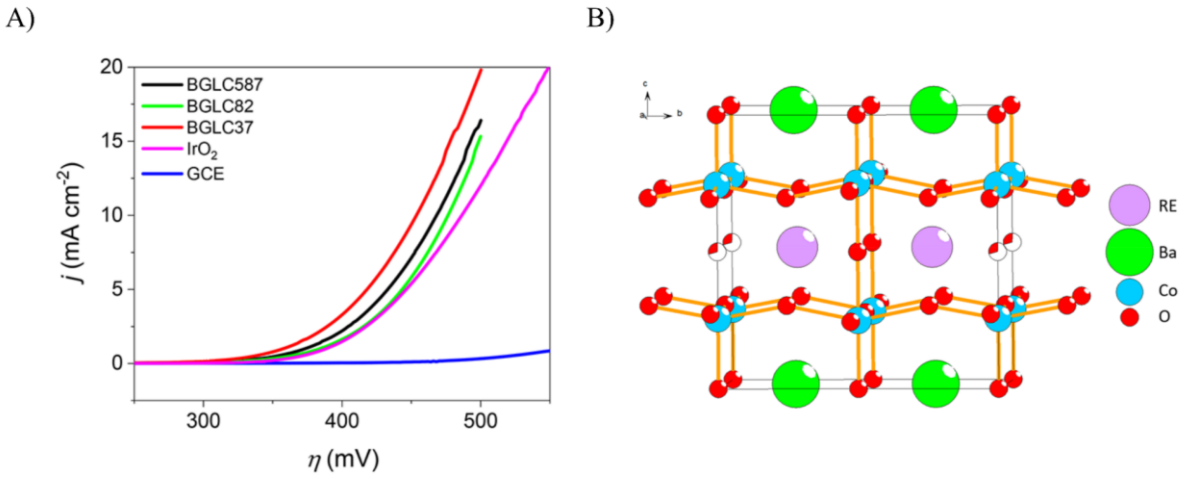

*Figure 3.4: **A)**: LSVs of OER performance of BGLC-based electrocatalysts in 1.0 M NaOH recorded at 10 mV s^{-1}. **B)**: Refined orthorhombic crystal structure (Pmmm) of the double perovskite phase in BGLC587. Figures from [27].*

BGLC587 was initially expected to take the orthorhombic double perovskite structure of $BaGdCo_2O_{6-\delta}$ (*Pmmm*) shown in Figure 3.4 B. However, Rietveld refinement of synchrotron radiation X-ray diffraction (SR-XRD) data showed the presence of five different phases. With 50.2 wt.%, the majority phase was found to be $LaCoO_3$ ($R\bar{3}c$), followed by 21.9 wt.%

$BaGdCo_2O_{6-\delta}$ (*Pmmm*) and 21.3 wt.% $Gd_{0.8}La_{0.2}O_3$ (*Pnma*). Smaller amounts of $BaCO_3$ (*Pmcn*) and Co_3O_4 ($Fd\bar{3}m$) were also found to be present.

A key aspect in understanding how OER electrocatalysts function is to analyse them post operation. Zhu et al. did this for BGLC587 using high-angle annular dark field scanning transmission electron microscopy (HAADF-STEM) and high resolution energy dispersive spectrometry (HREDS). This led to the observation of a reconstruction of the crystalline surface into a thin (5-6 nm) amorphous layer, which was accompanied by an A-site Ba loss. Figure 3.5 shows this amorphous layer from HAADF-STEM measurements. It was argued that the reconstruction of the surface may be responsible for the OER performance due to increased exposure of Co on the surface and hence activation of the adsorbate evolution mechanism (AEM). The cation vacancies from Ba loss was also expected to induce electron holes as charge compensating defects, furthermore promoting the OER performance.

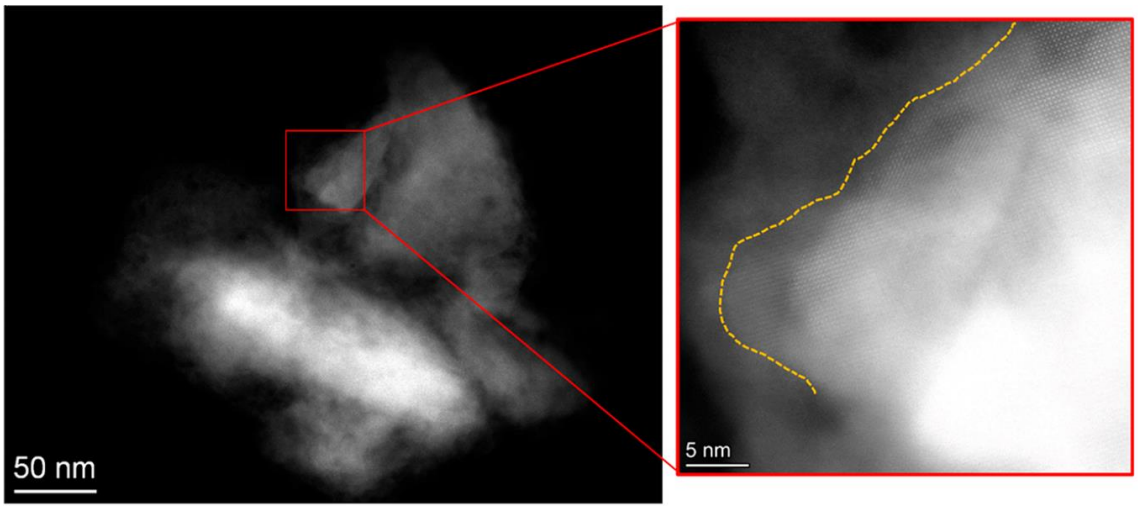

Figure 3.5: Post operation HAADF-STEM image of BGLC587. The yellow dashed line shows the amorphous-to-crystalline transition [27].

4 Methodology

The experimental share of this work is mainly divided into three parts: synthesis of electrocatalysts, electrochemical characterisation and physiochemical characterisation. During the first part, the sol-gel citrate method was used to synthesise oxide electrocatalysts with perovskite-type structure. The second part consists of a set of electrochemical measurements such as linear sweep voltammetry (LSV), cyclic voltammetry (CV), chronopotentiometry (CP), electrochemical impedance spectroscopy (EIS) and in situ Raman spectroscopy. Lastly, physiochemical characterisation of the perovskite powders and electrodes was conducted with X-ray diffraction (XRD), scanning electron microscope (SEM), transmission electron microscope (TEM) and Brunauer-Emmett-Teller (BET) surface area analysis. This section explains the details behind all of the methods in this work and Table 4.1 gives the abbreviations for all the synthesised electrocatalyst with different compositions. A list of all the chemicals used can be found in Table 9.1 in Appendix.

Table 4.1: Composition of the 17 synthesised electrocatalysts in this work with their respective abbreviations and nominal B-site subtitution.

Stoichiometric composition	Abbreviation	Nominal substitution
$Ba_{0.5}Gd_{0.8}La_{0.7}Co_2O_{6-\delta}$	BGLC587	Base material
$Ba_{0.5}Gd_{0.8}La_{0.7}Co_{1.8}Fe_{0.2}O_{6-\delta}$	BGLCF10	B-site: 10% Fe
$Ba_{0.5}Gd_{0.8}La_{0.7}Co_{1.4}Fe_{0.6}O_{6-\delta}$	BGLCF30	B-site: 30% Fe
$Ba_{0.5}Gd_{0.8}La_{0.7}Co_{1.0}Fe_{1.0}O_{6-\delta}$	BGLCF50	B-site: 50% Fe
$Ba_{0.5}Gd_{0.8}La_{0.7}Co_{0.6}Fe_{1.4}O_{6-\delta}$	BGLCF70	B-site: 70% Fe
$Ba_{0.5}Gd_{0.8}La_{0.7}Fe_2O_{6-\delta}$	BGLF	B-site: 100% Fe
$Ba_{0.5}Gd_{0.8}La_{0.7}Co_{1.8}Ni_{0.2}O_{6-\delta}$	BGLCN10	B-site: 10% Ni
$Ba_{0.5}Gd_{0.8}La_{0.7}Co_{1.4}Fe_{0.4}Ni_{0.2}O_{6-\delta}$	BGLCFN2010	B-site: 20% Fe and 10% Ni
$Ba_{0.5}Gd_{0.8}La_{0.7}Co_{1.4}Fe_{0.2}Ni_{0.4}O_{6-\delta}$	BGLCFN1020	B-site: 10% Fe and 20% Ni
$Ba_{0.5}Gd_{0.8}La_{0.7}Co_{1.0}Fe_{0.6}Ni_{0.4}O_{6-\delta}$	BGLCFN3020	B-site: 30% Fe and 20% Ni
$Ba_{0.5}Gd_{0.8}La_{0.7}Co_{1.0}Fe_{0.2}Ni_{0.8}O_{6-\delta}$	BGLCFN1040	B-site: 10% Fe and 40% Ni
$Ba_{0.5}Gd_{0.8}La_{0.7}Co_{1.0}Ni_{1.0}O_{6-\delta}$	BGLCN50	B-site: 50% Ni
$K_{0.1}Ba_{0.4}Gd_{0.8}La_{0.7}Co_2O_{6-\delta}$	KBGLC05	A-site: 5% K
$K_{0.3}Ba_{0.2}Gd_{0.8}La_{0.7}Co_2O_{6-\delta}$	KBGLC15	A-site: 15% K
$Ca_{0.2}Ba_{0.3}Gd_{0.8}La_{0.7}Co_2O_{6-\delta}$	CaBGLC10	A-site: 10% Ca
$Cs_{0.3}Ba_{0.2}Gd_{0.8}La_{0.7}Co_2O_{6-\delta}$	CsBGLC15	A-site: 15% Cs
$Ba_{0.5}Gd_{0.8}La_{0.7}Co_2N_xO_{6-x-\delta}$	BGLC-NH_3	O-site: Unknown amount N

4.1 Synthesis of Electrocatalysts

4.1.1 Sol-Gel Citrate Route

All electrocatalysts where prepared wet-chemically by the sol-gel citrate method as described in general by the flowchart in Figure 4.1. In this procedure, citric acid (CA) was dissolved in DI water in a 1 L beaker on a hotplate with constant magnetic stirring. Using a 1:1 ratio of CA and mol cations, a stoichiometric amount of precursors were slowly added until fully dissolved. The pH was then adjusted with concentrated ammonia until reaching pH 6-7 and obtaining a clear solution. Too low pH could have caused the solution to bleak and precipitate.

The water was further evaporated from the solution on the hotplate at 150°C until a very viscous and eventually dry gel was formed. At this point, the beaker was covered with a watch glass and put in a ventilated heating cabinet to obtain a more homogeneous heat distribution. The beaker was left in the heating cabinet for 2 h at 250°C to let the combustion reaction finish. The ash obtained was crushed thoroughly in a mortar inside a fume hood and transferred to a magnesia crucible. The powder was fired at 450°C for 2 h with a ramp rate of 300°C per hour to burn off most organic compounds. The powder was crushed thoroughly a second time and calcined at 1100°C for 8 h with a ramp rate of 250°C per hour to form the final powder.

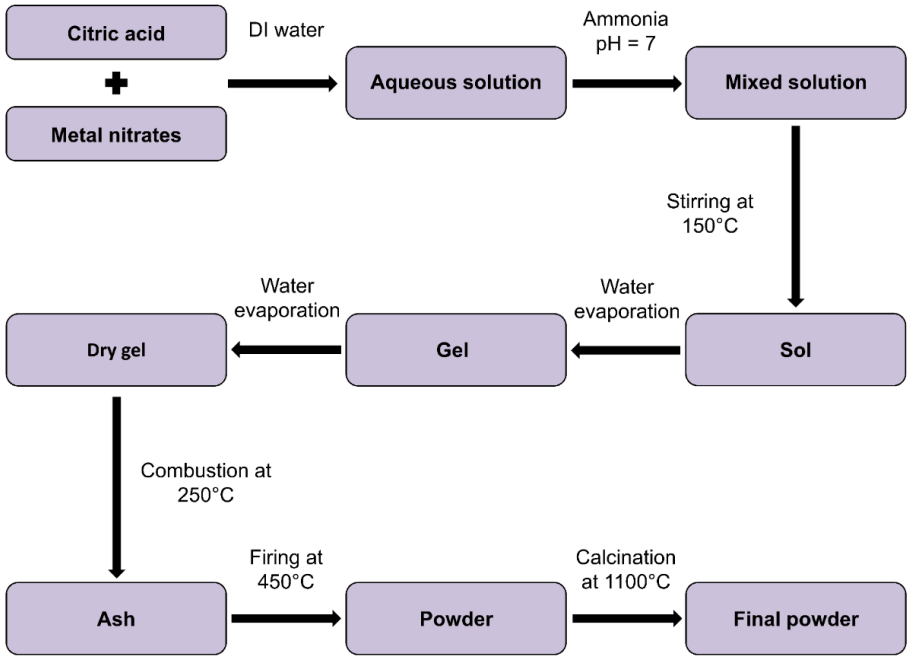

Figure 4.1: Flow-chart of sol-gel citrate method used to synthesise the oxide perovskites in this work.

4.1.2 Annealing in NH_3

A method proven to enhance the catalytic activity of perovskite cobaltites such as $LaCoO_3$ is doping with nitrogen [21]. Such anion doping can induce defects and alter the electronic properties of the active elements in the electrocatalyst. In the case of N-doping, one would expect N to be in a trivalent oxidation state substituting divalent O. This would make the material acceptor doped and could therefore increase the electron hole concentration as the positive charge compensating defect.

To approach this, pristine BGLC587 powder synthesised by the sol-gel method was annealed in ammonia at 400°C for 6 h in a tubular furnace. As can be seen in Figure 4.2 A and B respectively, Pt-foil was used as an inert crucible to contain the powder and a ProboStat™ (NorECs AS) was used to connect the thermocouple and the gas inlet/outlet, thus controlling the both the temperature and the annealing atmosphere. The crucible was put on top of the inner alumina tube (Figure 4.2 A) and the outer tube was placed over the inner and fastened to the Probostat™. Ammonia was supplied through the inner chamber (inside the inner tube), while blocking the inner gas outlet to have gas passing by the crucible and through the outer chamber outlet. The system was purged with N_2 gas prior to the experiment and while the furnace was cooling down after the experiment before retrieving the sample.

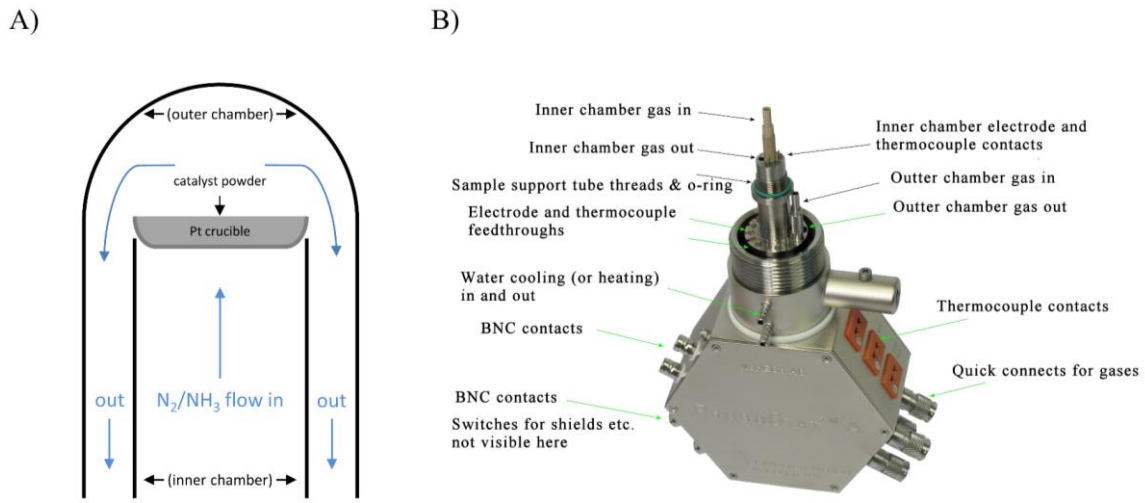

*Figure 4.2: **A)**: Pt-crucible with catalyst powder mounted on top of the inner alumina tube supplying the NH_3 gas. **B)**: Description of the Probostat™ cell [71]. Only the gas connects and the thermocouple contacts were used.*

4.2 Electrochemical Characterisation

All electrochemical measurements were carried out in a 1 M KOH electrolyte solution at room temperature (20 ± 2°C). All electrochemical experiments were controlled with a Gamry REF3000 potentiostat. If nothing else is specified, measurements were done using a three-electrode setup with a graphite counter electrode (CE) and a saturated calomel electrode (SCE) reference electrode (RE). The SCE is not considered stable in alkaline electrolytes since it is prone to chloride ion leaching and hydroxide diffusion from the electrolyte, which can have dire effects on both the potentials measured and the reaction kinetics of the working electrode [72, 73]. Therefore, longer measurements were conducted using a Hg/HgO (20% KOH) reference electrode which is the preferred reference electrode in alkaline solutions. However, whenever the SCE was used, it was always checked for drifts in potential prior to and after measurements. As working electrode (WE), both a rotating disk electrode (RDE) and C-paper electrode was used, depending on the measurement. The electrolyte solution was saturated with O_2 gas before and during all OER measurements.

4.2.1 Preparation of Catalyst Ink

Catalyst inks were prepared in a similar manner as in ref. [74] and [27] by dispersing 10 mg of catalyst powder in a solution of 1 mL ethanol and 100 µL 5 wt.% Nafion®. The ink was ultrasonicated in an ice bath for 1 h prior to being used. Before ink preparation, the catalyst powders where sieved in a vibratory sieve from Retsch using a 20 µm sieve. This ensured that the powders dispersed more homogeneously in the ink and ultimately resulting in better a distribution on the substrate electrode.

4.2.2 The Rotating Disk Electrode (RDE)

To assess the activity of the electrocatalysts in a system with negligible mass-transfer limitations, a Gamry RDE710 Rotating Electrode with a glassy carbon (GC) tip was used in a three-electrode setup as shown in Figure 4.3 A. The speed of the RDE was set to 1600 rpm to ensure satisfactory removal/availability of products/reactants.

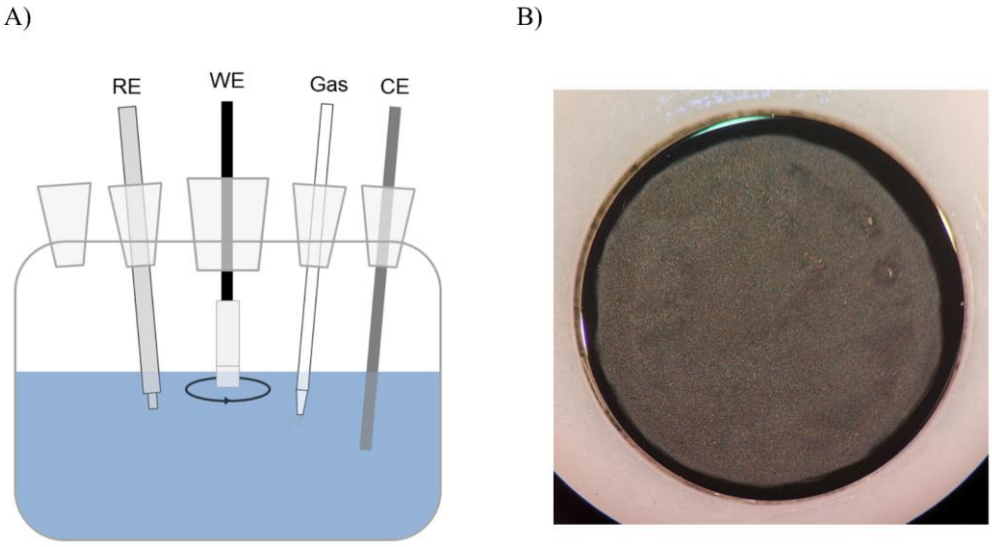

*Figure 4.3: **A)**: Illustration of the 3-electrode setup used in the electrochemical measurements. RE was either the SCE or Hg/HgO (20% KOH), WE was the RDE or C-paper and the CE was a graphite rod. **B)**: Representative appearance of the RDE surface with 0.28 mg cm^{-2} catalyst loading. The photo was taken through an optical microscope.*

Electrode preparation

Before electrochemical measurements were done, the GC electrode was polished to a mirror finish with alumina slurry (0.05 µm grains) on a polishing pad. Subsequently, it was ultrasonicated in 1 M KOH for about 5 minutes and rinsed in DI water before left to dry in ambient. This method was adapted from ref. [72] and [75]. The electrocatalyst powder was loaded on the electrode by drop-casting 6 mL of catalyst ink, corresponding to a loading of 0.28 mg cm^{-2}. To prevent any bubbles of air sticking to the electrode surface upon immersing it in the electrolyte, it was covered with a 30 µL droplet of DI water. Figure 4.3 B presents a representative photo of the RDE after electrode preparation.

Cyclic Voltammetry

After electrode preparation, CV was utilised to clean the electrode electrochemically. This was done by cycling the electrode from 0.03 to 1.0 V vs. RHE at 50 mV s^{-1}, as argued in , until a steady-state was reached. CV was then used to condition the electrocatalyst in the OER region by cycling the potential with a scan rate of 10 mV s^{-1} from the non-Faradaic region (around 1.1 V vs. RHE) to that which was required to reach a current density of 10 mA cm^{-2}. Typically, 10 cycles were enough to reach a steady-state. An example this CV cleaning and activation procedure is given for BGLC587 in Figure 4.4 A and B respectively.

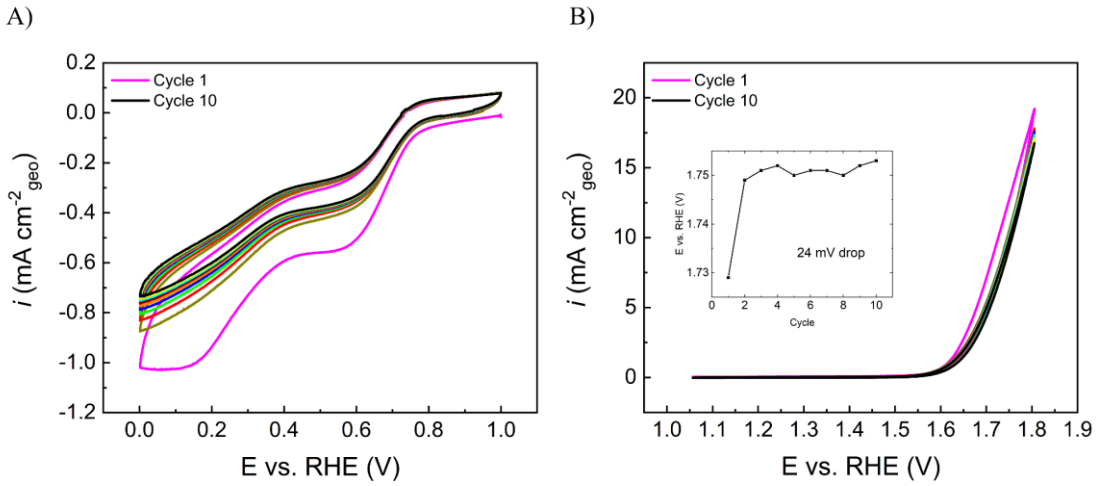

*Figure 4.4: Conditioning of the electrode materials on the RDE by **A)**: CV cleaning procedure and **B)**: CV activation procedure. The inset in B) shows how the potential stabilises during 10 CV cycles.*

After conditioning the electrode, CV was done in the non-Faradaic region (region with only capacitive current) from 1.06 to 1.16 V vs. RHE with scan rates varying from 5 to 200 mV s^{-1}. A representative figure of such a measurement on BGLC587 is given in Figure 4.5 A. The data obtained from this were used to evaluate the electrochemically active surface area (ECSA) through the double layer capacitance, C_{dl} (F). From the CV curves at different scan rates, ν (mV s^{-1}), the charging current, I_c, was found by Equation (4.1)

$$I_c = \frac{I_{anodic} - I_{cathodic}}{2} \tag{4.1}$$

where I_{anodic} and $I_{cathodic}$ are the currents associated with the positive and negative charging of the electrocatalyst surface respectively. C_{dl} was then found from the slope of Equation (4.2)

$$I_c = C_{dl} \cdot \nu \tag{4.2}$$

where it can easily be seen that C_{dl} has units $\mathrm{F} = \frac{\mathrm{A \cdot s}}{\mathrm{V}} = \frac{\mathrm{C}}{\mathrm{V}}$. Figure 4.5 B is a representative figure of how this relation looks experimentally in the Fe substituted ECs. It is not uncommon to observe two linear regions such as in this figure: one at lower scan rates (below ~50 mV s^{-1}) and one at higher rates (above ~50 mV s^{-1}).

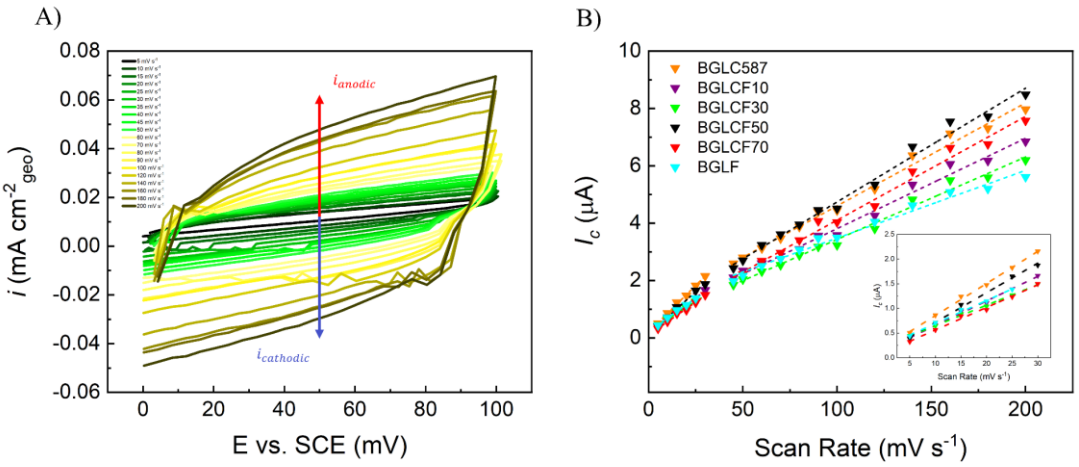

*Figure 4.5: **A)**: CV curves in the non-Faradaic region (capacitive region) taken at scan rates 5-200 mV s^{-1} for BGLC587. **B)**: Plot of capacitive current vs. scan rate for the Fe substituted ECs. We can clearly observe two linear regions. The inset is a magnification of the data from the lower region.*

Linear Sweep Voltammetry

Linear sweep voltammetry was used to acquire polarisation curves from the non-Faradaic region to the potential required to reach 10 mA cm^{-2}. The LSVs were collected at a scan rate of 10 mV s^{-1} and *iR*-compensation was done manually after measurement by using the solution resistance, R_s, found from EIS. From the LSVs, overpotentials at the onset and 10 mA cm^{-2} current density were extracted along with the Tafel slope.

Electrochemical Impedance Spectroscopy

In this work, EIS was performed at DC voltages corresponding to the non-Faradaic region, the onset and a current density of 10 mA cm^{-2}. The EIS spectra was acquired with an AC frequency range of 100 kHz to 0.1 Hz and an AC voltage of 10 mV rms. Zview (Scribner) was used to fit the data to the extended Randles circuit shown in Figure 4.6, equivalent to the one discussed in Chapter 2.4.3. The circuit consists of a solution resistance (R_s) which accounts for the electrolyte resistance as well as wires, clips and connections. Following R_s there are two R||C elements in series consisting of a resistor and constant phase element (CPE) in parallel with each other.

The first R||C element is related to the resistive (R_d) and capacitive (C_d) behaviour of a surface passivation layer and diffusion of reactants close to the surface [27, 40], while the second originates from the interfacial resistive (R_{int}) and capacitive (C_{int}) behaviour of the catalyst material. The constant phase element is used instead of a pure capacitor to account for the non-ideal capacitive behaviours in the system.

From the fitting, the charge transfer resistance and double layer capacitance was calculated from Equation (4.3) and (4.4).

$$R_{ct} = R_d + R_{int} \tag{4.3}$$

$$C_{dl} = \frac{1}{\frac{1}{C_d} + \frac{1}{C_{int}}} \tag{4.4}$$

where the capacitances in Equation (4.4) were found with Equation (4.5) containing values from the deconvolution

$$C_i = \left[Y_{0,i} \, R_i^{(1-n_i)} \right]^{\frac{1}{n_i}} \tag{4.5}$$

where $Y_{0,i}$ is the magnitude of the admittance of the ith CPE, R_i is the resistance of the resistor in parallel with the CPE and n_i defines the phase of the CPE. Lastly, from Equation (4.3) and (4.4), the $R_{ct}C_{dl}$ product was calculated as a descriptor on the intrinsic catalytic activity (ICA) of the electrocatalysts.

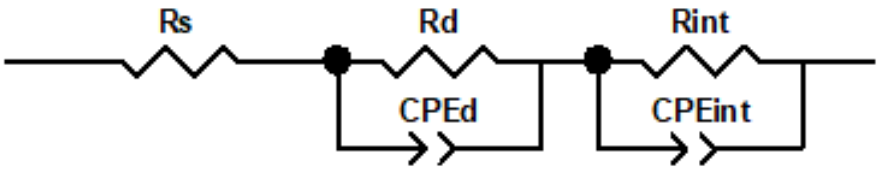

Figure 4.6: The equivalent circuit used to fit the impedance spectra. R_s is the solution resistance taking into account the also wires, clips and other contacts. The R_d and CPE_d are the resistance and capacitive behaviour associated with a surface passivation of the electrode, while R_{int} and CPE_{int} are the interfacial charge transfer resistance and capacitance of the electrode.

Chronopotentiometry

The Tafel slopes of the electrocatalysts were evaluated under steady-state conditions by doing a stepped CP measurement. The cell was run at a constant current density of 0.031, 0.061, 0.128, 0.250, 0.500, 1.020, 1.990 and 3.980 mA cm^{-2}_{geo} for 5 minutes each in order to reach a steady-state potential. The steady-state potential was calculated as the average of the potentials measured in the last 30 seconds of each step. The Tafel slope was found by plotting the steady-state overpotential, η, as a function of the logarithm of the current density, $\log(i)$.

4.2.3 Stability

To assess the stability of the electrocatalyst during oxygen evolution, chronopotentiometric (CP) measurements were performed at 10 mA cm^{-2}_{geo}. A 3-electrode setup as shown in Figure 4.3 A with the Hg/HgO (20% KOH) reference electrode and C-paper working electrode was used. The importance of using an electrode with a surface area of exactly 1 cm^2 for stability measurements is argued in ref. [33]. The main reason for this is that a small electrode typically needs less overpotential to give an equal current density compared to a large one. This ultimately exposes the EC to a lower and less harsh overpotential compared to a realistic situation. Another argument for using C-paper electrodes is that the electrocatalyst powders deposited on the RDE in general have a tendency of quickly detaching, which makes it unsuitable for long-term stability measurements.

Electrode preparation

Because of the above, the RDE configuration is not suitable for long-term stability measurements. Therefore, C-paper electrodes with a loading of 5 mg cm^{-2} were made by drop casting. The C-paper from Alfa Aesar is of the same grade used as substrate electrodes in polymer exchange membrane (PEM) electrolysers. As shown in Figure 4.7 A, the C-paper electrodes were designed to have a nominal surface area of 1 cm^2, whereas comparatively, the RDE has a geometric surface area of only 0.196 cm^2. The middle part of the C-paper electrodes were covered in Teflon™ tape, while the ends were wrapped in aluminium foil to ensure good contact and stability. Figure 4.7 B is representative of how the electrodes looked after catalyst deposition. The C-paper electrodes were cleaned and conditioned following the same procedure as was used for the RDE in Section 4.2.2 before CP measurements.

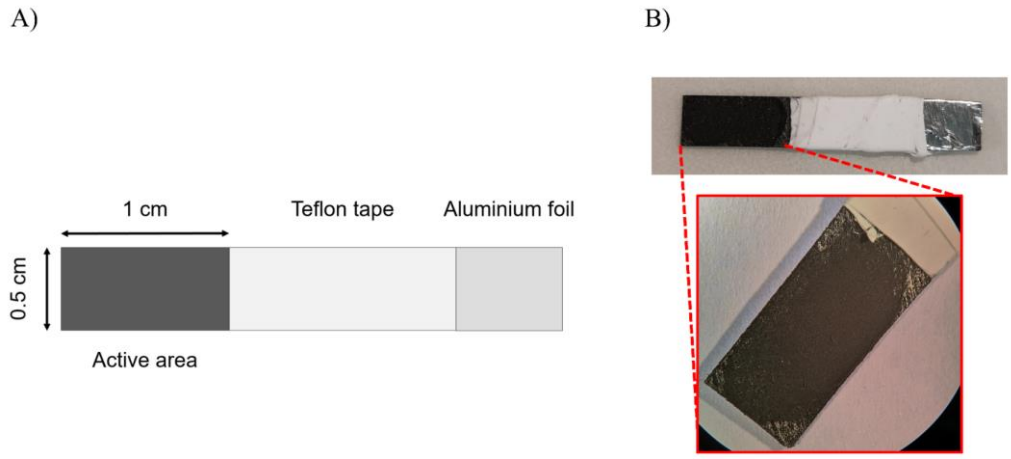

*Figure 4.7: **A)**: Schematic drawing of the C-paper electrode. **B)**: Photo of a C-paper electrode with 5 mg cm^{-2} loading. The red square is representative of the 1 cm^2 electrode area after catalyst loading.*

4.2.4 Faradaic Efficiency

The Faradaic efficiency of the electrocatalysts was determined by measuring the amount of O_2 and H_2 gases evolved as a function of time with a 3000 Micro Gas Chromatograph (GC) from Agilent Technologies. As depicted in Figure 4.8, a special gas tight 2-electrode cell with four openings was used for this purpose. One of the openings was coupled to the micro GC via Swagelok connections and Ar carrier gas was supplied to the cell through another. A C-paper electrode with 15 mg cm^{-2} loading was used as WE with a Pt-mesh RE/CE.

All connected parts were sealed gas-tight with epoxy, while caps with O-rings and Si-based grease. The headspace was clamped onto the lower part with a steel clamp. Before measuring, the cell was also purged free of O_2 and N_2 with Ar gas. Since Pt electrodes at cathodic potentials very easily can perform the oxygen reduction reaction (ORR), a plastic separator was put in between the WE and the RE/CE. This ensured that the transport of O_2 gas to the cathode was as limited as possible. In advance of the experiment, the GC was calibrated for H_2, O_2, and N_2 by measuring gases with known composition.

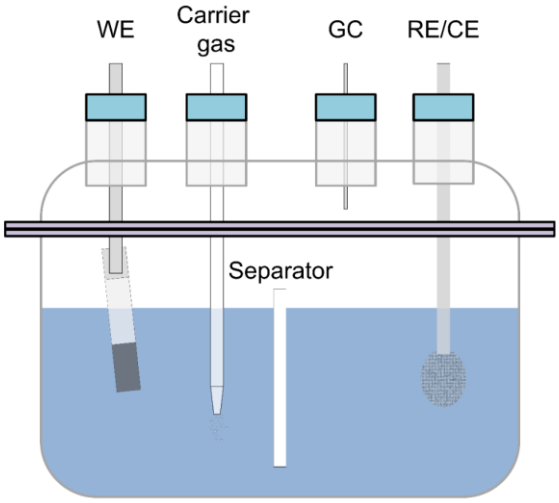

Figure 4.8: Illustration of the gas tight cell used to measure the Faradaic efficiency. From left: working electrode, carrier gas inlet, gas chromatograph outlet and reference/counter electrode.

Every 5 minutes, the percentage of H_2, O_2 and N_2 in the headspace of the cell were measured. With these, the number of moles of each gas, n_A, were found by multiplication with the total number of moles gas in the cell, n, which was calculated using the ideal gas law in Equation (4.6)

$$pV = nRT \tag{4.6}$$

where p is the pressure inside the headspace and was assumed to be 1 atm, V is the volume of the headspace which was measured to be 64 mL, T is the temperature and R is the ideal gas constant.

The cell was run galvanostatically at a current density of 5 mA cm^{-2} from which the amount of charge, Q, was found by the relation: $Q = It$. Faradays 1st law of electrolysis states that the number of moles of a substance produced at an electrode is proportional to the current going through that electrode. This is what is given in Equation (4.7)

$$Q = n_A F N_A \tag{4.7}$$

where N_A is the number of electrons needed to produce one mole of substance A , F is Faradays constant and n_A is the number of moles of substance A. The Faradaic efficiency was then calculated from Equation (4.8).

$$\eta_F = \frac{N_A F n_A}{It} \cdot 100\% \tag{4.8}$$

4.2.5 In situ Raman Spectroscopy

In situ Raman spectroscopy analysis was performed by Alaa Faid (NTNU) using a WITec alpha 300 R Confocal Raman spectrometer equipped with a 532 nm laser with a power of 20 mW. The Raman spectrometer was coupled with a Zeiss EC Epiplan 10 x objective and G1: 600 g/mm BLZ = 500 nm grating. Raman spectra were obtained after 30 s, 1 min, 5 min, 10 min and 30 min while keeping 1.6 V vs RHE.

The electrochemical cell consisted of catalyst deposited on glassy carbon electrode (Pine Research), Pt electrode, and Hg/HgO electrode (Pine Research) as working, counter, and reference electrode. N_2 saturated 1.0 M KOH electrolyte was used in the experiments. The laser beam was focused on the working electrode during the in-situ measurements.

Raman spectroscopy is a vibrational spectroscopic technique that can measure vibrational, rotational and low-frequency modes of species on the surface of a specimen [76]. When it is applied during OER, Raman spectroscopy can provide insightful information on the chemical bonds and adsorbed intermediates present at the surface. With this, it can even be possible to tell something about the oxidation state of the elements on the surface. Therefore, in situ Raman

spectroscopy can contribute to understanding the mechanism and chemical path by which the OER happens at different electrocatalyst surfaces.

4.2.6 Reference electrode calibration

To report values trustworthy and comparable with literature, it was taken care that the potential of the reference electrode versus the reversible hydrogen electrode (RHE) was well defined. All measured potentials were first calculated versus the standard hydrogen electrode (SHE) from Equation (4.9)

$$E_{SHE} = E_{measured} + E_{ref} \tag{4.9}$$

where $E_{measured}$ is the observed potential vs. the reference electrode and E_{ref} is a constant potential defined as the open circuit potential between the given reference electrode and the SHE. For the SCE, this potential is 0.241 V.

In theory, all reference electrodes have a given potential vs. SHE. However, the potential vs. SHE is pH dependant and reporting it vs. the RHE is therefore much more beneficial as it has no contribution from variations in pH. All experiments in this work was done in 1 M KOH, which has a theoretical pH of 14. Theoretically, the conversion from SHE to RHE can be calculated from Equation (4.10) derived from the Nernst equation

$$E_{RHE} = E_{SHE} + pH \cdot \frac{2.303\ RT}{F} \tag{4.10}$$

where E_{SHE} is found from Equation (4.9), R is the ideal gas constant, T is the temperature and F is Faradays constant. At 25°C, the potential of the reference electrode vs. SHE is shifted 59 mV per pH value according to Equation (4.10). Since pH values above 13 can be hard to determine precisely, it can also affect the measured potential with up to tens of mV [72]. Therefore, instead of using Equation (4.10), the potential of the SCE reference electrode vs. RHE was found from Equation (4.11)

$$E_{RHE} = E_{measured} - E_{offset} \tag{4.11}$$

where $E_{measured}$ is the potential measured vs. the reference electrode itself. E_{offset} was found by doing CV in the hydrogen evolution/oxidation reaction (HER/HOR) region with a polished Pt wire WE and Pt mesh CE in H_2 saturated electrolytes. The value of E_{offset} was then determined from the mean value of the intercepts with the x-axis. The CV was done with

constant magnetic stirring and at a scan rate of 1-2 mV s^{-1} to obtain close to steady-state conditions. This method was adapted from [72] and [77]. Prior to calibration, the cell was deaerated with Ar gas whereupon all connections were sealed with O-rings, Si-grease and Parafilm®.

To evaluate the experimentally obtained values to the theoretical ones, calibration of the SCE was done in several KOH electrolyte concentrations (0.085, 0.85, 0.9 and 1 M). The theoretical values of E_{offset} was found from Equation (4.10) with E_{SHE} = 0.241 V. By plotting the E_{offset} values as a function of KOH concentration, the theoretical model was compared to the experimentally derived data.

Result of Calibration

The calibration curves of the saturated calomel electrode (SCE) reference electrode in different KOH concentrations are given in Figure 4.9 A. From the intercepts with the x-axis, the E_{offset} values were found and plotted as a function of KOH concentration in Figure 4.9 B. The blue dashed line in Figure 4.9 B is the theoretical E_{offset} values as determined by Equation (4.1) which gives the pH dependency of the potential vs. the reversible hydrogen electrode (RHE). From the slope of the fitted line (red dashed line), it is observed that the trend found with the calibration method is in good agreement with the Nernstian behaviour of the blue theoretical line. However, the offset from the theoretical line supports the fact that Equation (4.10) should not be used carelessly, as it may not be a reliable way of converting the potential to the RHE.

In 1 M KOH, it was found that the experimental E_{offset} was -1057 mV, which is only 9 mV from the theoretical value of -1068 mV. This is not a significant difference and indicates that we are not too far from a theoretical system with electrolyte pH = 14. However, this might not be the case for all reference electrodes. As discussed above, reference electrodes can be prone to instabilities, which may alter their potential significantly and it is therefore considered good practice to calibrate them in the desired electrolyte. Even though the deviation was not found to be very significant in this case, it is in general sensible to reduce as many errors as possible, as there are many factors involved, which may become significant when combined.

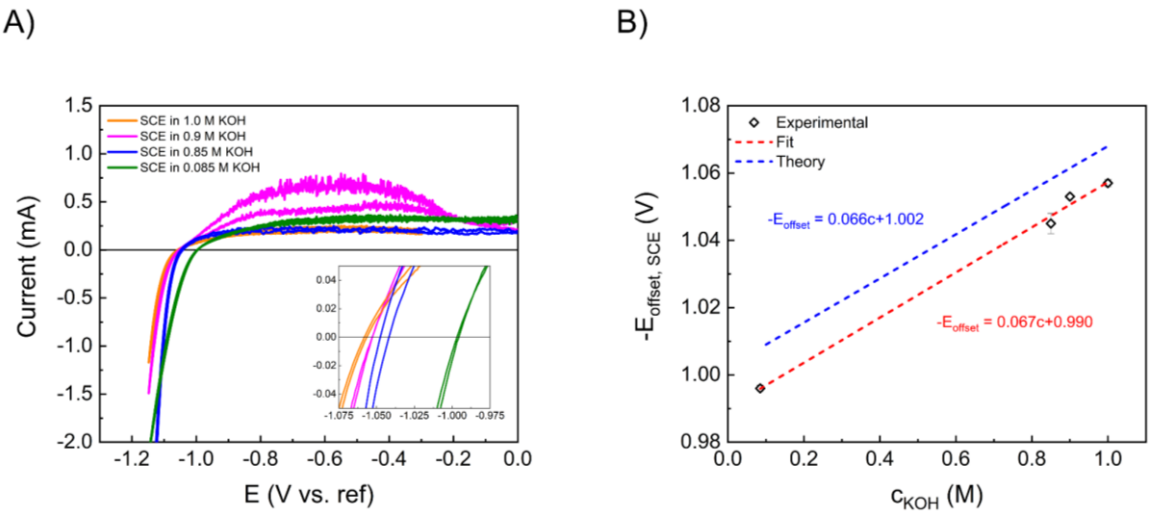

*Figure 4.9: **A)**: Measured calibration curves for the saturated calomel electrode (SCE) as function of KOH concentration. The intercepts with the x-axis of A) gives the E_{offset} values plotted in **B)**: which are compared to the theoretical values.*

4.3 Physiochemical Characterisation

4.3.1 X-Ray Diffraction (XRD)

The structure and phase purity of pristine and post operation electrocatalysts were determined with powder X-ray diffraction (PXRD). The measurements were done on a Bruker AXS D8 Discover with Bragg-Brentano geometry using Cu-$K_{\alpha 1}$ (λ = 1.54060 Å) and Cu-$K_{\alpha 2}$ (λ = 1.54439 Å) radiation. The samples were measured between 10° and 70° 2 with a step size of 0.02°. Initial fingerprint analysis was done in DIFFRAC.EVA V4.3 utilising data from the Crystallographic Open Database (COD). The phase composition of the B-site substituted electrocatalysts was found with Rietveld refinement in Topas V6 (Bruker) using cif-files from the COD and the authors in ref. [27]. All refinements had R_{wp}'s between 8 and 16, but they were primarily evaluated with respect to the geometry and position of the peaks. Based on the quality of the instrument and the X-ray source, it was estimated that an error of at least 4 wt.% could be expected. The as-synthesised catalysts were measured as powders, whereas post operation XRD was done on a catalyst loaded C-paper support.

4.3.2 Scanning Electron Microscopy (SEM)

The surface morphology and phase composition of the electrocatalyst powders were studied in a Hitachi SU8200 scanning electron microscope with acceleration voltages of 2-15 kV. A secondary electron (SE) detector was used for simple surface and porosity investigation, whereas a high-angle backscattered electron, HA(T), detector was used to obtain mainly atomic number contrast (Z-contrast). The Z-contrast originates from the fact that heavier elements

scatter electrons to higher angles than lighter elements. The elemental composition of the electrocatalysts were examined with Energy Dispersive X-Ray Spectroscopy (EDS) using a Bruker XFlash 6-10 detector.

4.3.3 Transmission Electron Microscopy (TEM)

BGLC587 and BGLCF70 were investigated with EDS in a FEI Titan G2 60-300 transmission electron microscope equipped with a DCOR probe C_s-aberration corrector. The TEM was operated in scanning transmission electron microscope (STEM) mode and EDS mapping were done at 300 kV acceleration. The EDS spectra were obtained with by a Super-X EDS detector.

4.3.4 X-Ray Photoelectron Spectroscopy (XPS)

X-Ray photoelectron spectroscopy (XPS) was performed on ECs with 0, 30, 50 and 70% Fe substitution by Ingvild Thue Jensen (SINTEF). The measurements were done on a Kratos Axis Ultra^{DLD} operated at 10 A and 15 kV with monochromated Al Kα = 1486.6 eV. Pass energy was 160 eV (survey) and 20 eV (high resolution) with step sizes of 1 eV (survey) and 0.1 eV (high resolution). The samples were pressed into high-purity In foil and mounted on glass. Charge correction was applied to the measurements. The data was analysed in the CasaXPS software with Shirley background subtraction. Energy axis was calibrated using C 1*s* = 284.8 eV.

4.3.5 Brunauer-Emmett-Teller (BET) Surface Area Analysis

Surface area estimation of the ECs was conducted by the BET technique using a Belsorp Mini X (MicrotracBEL Corp.). The electrocatalyst powders were activated in vacuum at 300°C for about 3 h to remove any physisorbed water and hydrocarbons at the surface. Approximately 1g of powder was used in each measurement and N_2 was used as the adsorptive gas. Only the B-site substituted samples where measured with the BET method.

5 Results and Discussion

5.1 Physiochemical Characterisation

This section presents the structural, elemental and morphological properties of the synthesised electrocatalysts. All materials were initially investigated with powder X-ray diffraction (PXRD) to determine whether the crystal structure had changed significantly from that of the pristine BGLC587. After an initial electrochemical screening of the electrocatalytic activity, some catalysts were studied more extensively and this section will mainly focus on these. More specifically, these materials are the B-site substituted samples and BGLC587 annealed in NH_3 (BGLC-NH_3). The PXRD data of the rest of the materials (A-site substituted) can be found in Figure 9.1 in the Appendix. It can be mentioned that all showed diffraction patterns similar to BGLC587, but the exact phase composition was not investigated.

5.1.1 Crystal Structure and Phase Compositions

The Rietveld refinement of the PXRD pattern of the base electrocatalysts material (BGLC587) is presented in Figure 5.1. An important result from this is that the phase composition of the synthesised BGLC587 has the same trend as those found for the commercial material by Zhu et al. [27].

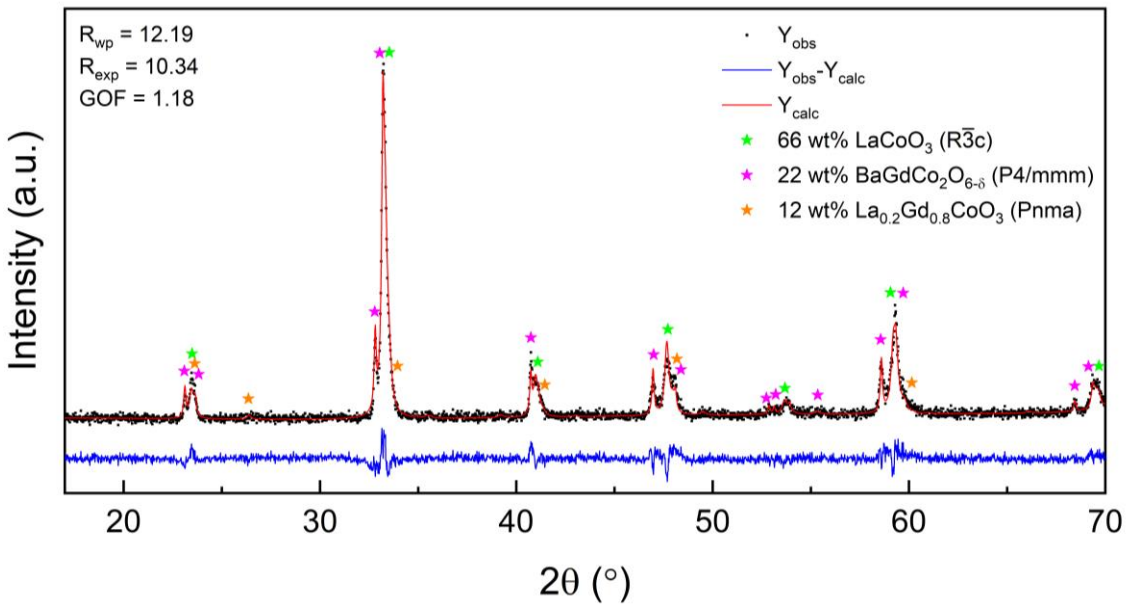

Figure 5.1: Powder XRD pattern of BGLC587 (black) with Rietveld refinement (red) and the residual plot (blue). Stars show peaks belonging to the refined phases.

In short, we see a majority of rhombohedral $LaCoO_3$ phase and two minor orthorhombic phases of the double perovskite $BaGdCo_2O_{6-\delta}$ and single perovskite $Gd_{0.8}La_{0.2}CoO_3$ (GdFeO-type structure) This proves that we have obtained successful synthesis conditions, where the commercial material has been reproduced satisfactory. To limit unnecessary figures, the Rietveld refinement graphs of the other catalyst samples are not presented in this work, however they were all done in the same way and had R_{wp}'s within 8 and 16.

Fe Substitution

The PXRD patterns of the Fe substituted electrocatalysts are given in Figure 5.2. We can see that the number of peaks and their positions in general look similar to the pristine BGLC587. However, a small shift towards lower 2θ values is observed for all peaks with increasing Fe content. There is also a small peak occurring at 2θ approximately equal to 26°, which could be due to an increase in the orthorhombic perovskite structure.

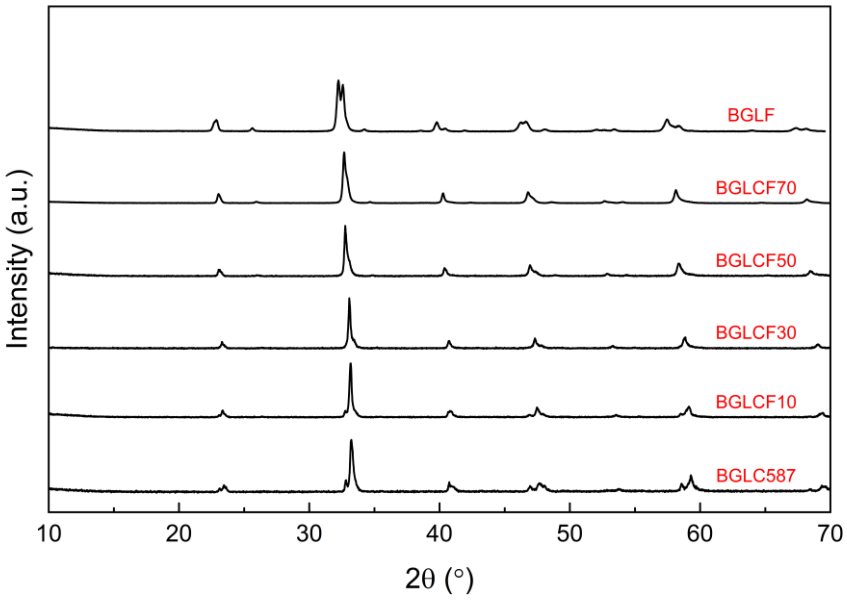

Figure 5.2: PXRD patterns of as synthesised Fe substituted BGLCs.

Figure 5.3 A and B present the results from Rietveld refinement of the PXRD data of BGLC587 as a function of Fe incorporation on B-site. From Figure 5.3 A, it can be seen that there are four different phases involved in the phase compositions: rhombohedral $LaCoO_3$ (LC) and the three orthorhombic phases $BaGdCo_2O_{6-\delta}$ (BGC), $LaFeO_3$ (LF) and $Gd_{0.8}La_{0.2}CoO_3$ (GLC). It is important to note that the two latter phases have quite similar symmetry (*Pbnm/Pnma*) and that a good fit from Rietveld refinement was usually also obtained without the LF phase. We therefore do not exclude the fact that some of the GLC phase can be mistaken for the LF phase.

It is evident that the amount of LC phase decreases with increasing Fe-content, which happens in parallel with an increase in the wt.% of BGC, GLC and LF. From this, it seems that increasing Fe-content favours the formation of the double perovskite phase (BGC) and that the rhombohedral symmetry of LC is transformed to orthorhombic as the Co-content declines. The latter is also consistent with findings in literature [78, 79].

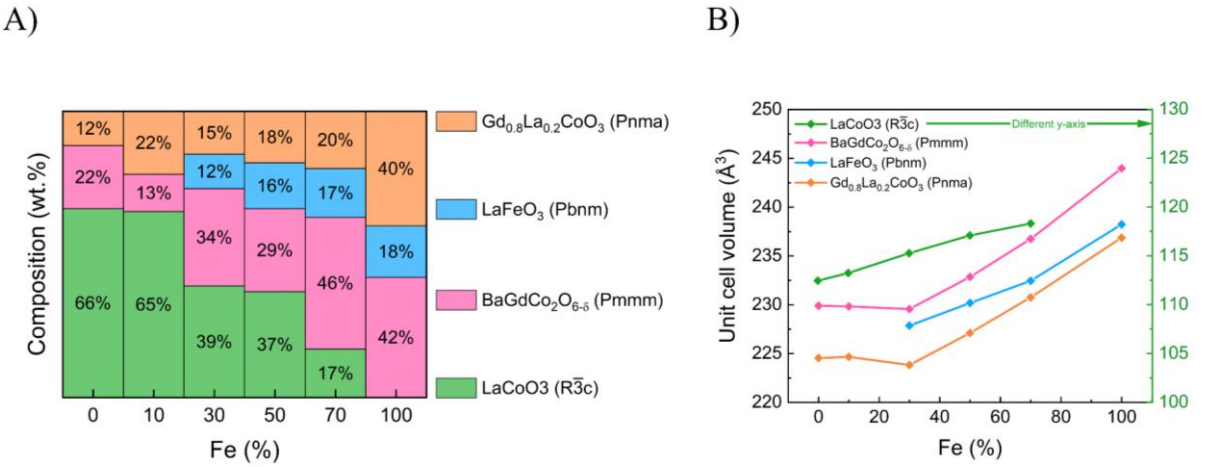

*Figure 5.3: **A)**: Phase composition of BGLC587 as a function of Fe substitution. Four different phases are present: rhombohedral LaCoO3 and three orthorhombic phases $BaGdCo_2O_{6-\delta}$ (BGC), $LaFeO_3$ (LF) and $Gd_{0.8}La_{0.2}CoO_3$ (GLC). **B:)** Unit cell volume of the different phases. The green y-axis corresponds to the data points of $LaCoO_3$, whereas other data follow the left axis. Both axes span 30 Å^3 to make comparisons between phases easier. The structural data were found by Rietveld refinement.*

Fe-content has a clear effect on the unit cell volume of all phases as they all in general increase with increasing Fe-content. This is in good agreement with the shift towards lower 2θ values. We also find this in similar Co containing perovskites [39, 78], where the increase is due to the larger covalent radius of Fe^{3+} (both low- and high-spin configurations) compared to that of Co^{3+}. The relative increase could therefore indicate which phases has the most Fe incorporation. However, this is assuming that there is no change in the ratio of A-site cations, which is not likely considering the significant variation in phase compositions as a function of Fe-content.

It is difficult to identify the distribution of cations in-between the different phases in this system without knowing the exact distribution in the starting material BGLC587. However, single-phase analysis of BGC found that it has a unit cell volume of 228.6 Å^3 [80]. Comparatively, a unit cell volume of 229.9 Å^3 was found for the refined BGC phase in BGLC587. The small difference can be an indication that the BGC phase is in fact pure, and that La is mainly distributed mainly between LC and GLC. Taguchi et al. reported the rhombohedral $LaCoO_3$ to have a unit cell volume of 111.98 Å^3 [81], which is comparable to 112.4 Å^3 found in BGLC587.

Again, this indicates that the LC phase is pure, which in principle leaves the GLC phase with the remaining A-site cations, mainly Gd.

Still, one problem emanating from the above hypothesis is that the LC phase has as much as 66 wt.%. If it were assumed that all A-site cations have equal mass, the maximum possible wt.% of a pure LC phase in BGLC587 would be equal to the percentage of La at A-site, which is 35%. Therefore, the LC phase cannot be pure, but then one can ask why the unit cell volume is so close to the pure phase? An answer to this could be related to the fact that the ionic radii of Ba, La and Gd decreases in this order. It is therefore theoretically possible that substitution of La with a combination of Ba and Gd can keep the unit cell volume stable and hence, facilitate the 66 wt.% of LC phase which is observed. The same analogy is in fact also applicable for the BGC phase, where it is possible that La substitute Ba and Gd in such ratios that the unit cell is close to the pure phase. We therefore assume that the distribution of A-site cations between the phases in all the materials synthesised in this thesis cannot be extracted entirely based on the PXRD data. To do this, elemental quantification with instruments giving higher spatial resolution, such as for example the scanning transmission electron microscope (STEM), can be better options. However, it must be mentioned that, statistically speaking, one looks at very small areas in the STEM and many measurements should be done to have trustable data.

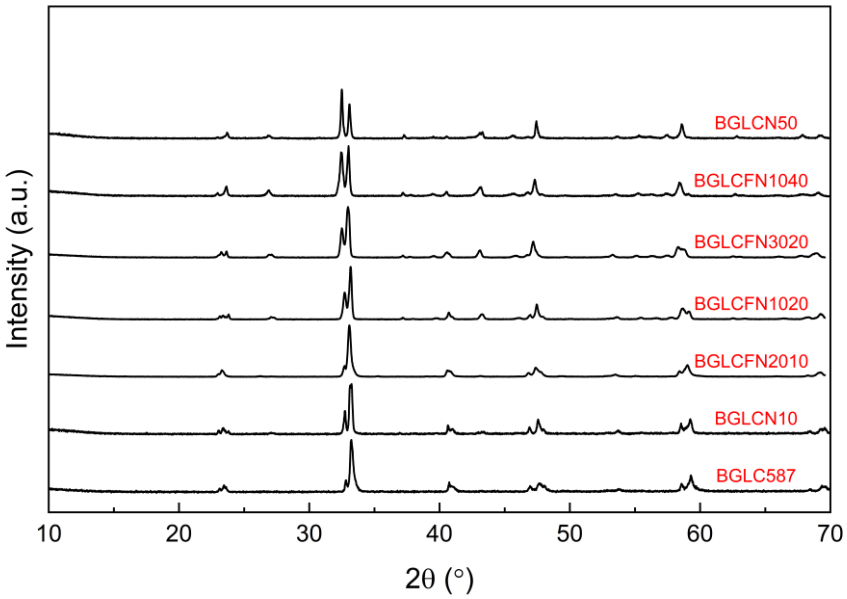

Figure 5.4: PXRD patterns of as synthesised Fe and Ni substituted BGLCs.

Ni and Fe Substitution

The PXRD patterns of the samples containing Ni and the combination of Ni and Fe is given in Figure 5.4. The Ni content in the compositions increases from the bottom diffractogram of BGLC587 to the top one of BGLCN50 and we can see from this that new peaks are forming as the Ni content increases.

The refined phase composition and unit cell volume of the samples in Figure 5.4 is given in Figure 5.5 A and B respectively. It is observed that two new phases appear, namely the orthorhombic Ruddlesden-Popper (RP) type $La_3Ni_2O_7$ with two rock salt layers and the cubic NiO_x phase. With only 10% Ni the orthorhombic GLC phase disappears and the $LaCoO_3$ phase is reduced, though maintaining its unit cell volume. As more Ni is incorporated, the LC phase diminishes completely and the RP-phase dominates with 72 wt.%. It is likely that the formation of NiO_x is a consequence of excess Ni, because the RP-phase has a 3:2 ratio between A- and B-site cations, and the desired BGLC-phase has a 1:1 ratio. No secondary phase with Co was found, which indicates that Ni is the only excess B-site cation.

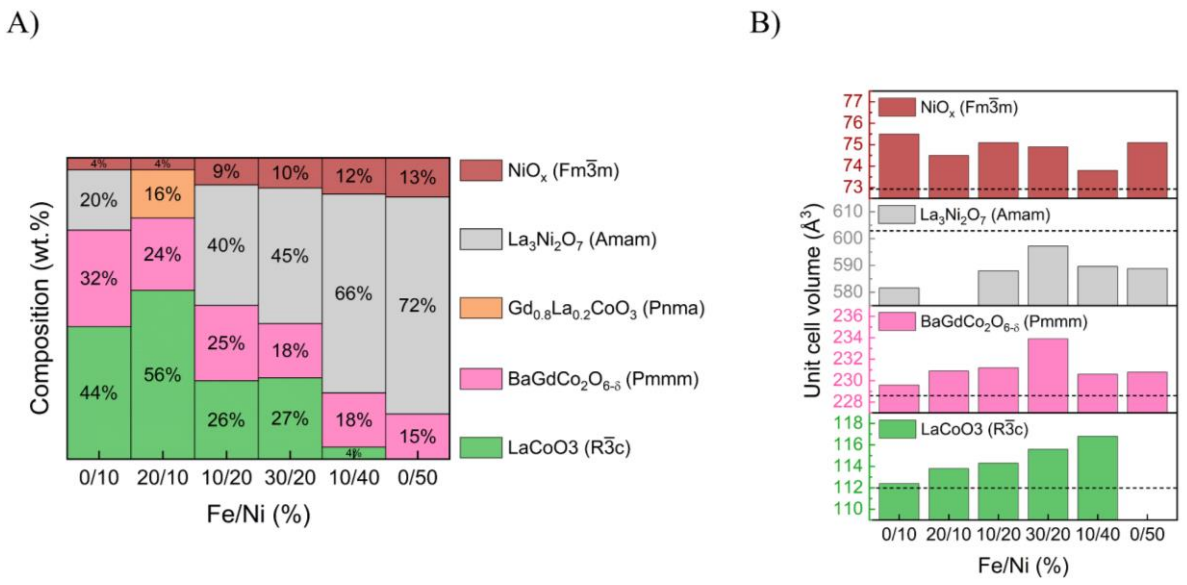

*Figure 5.5: **A)** Phase composition of electrocatalysts with both Fe and Ni substitution. The x-axis gives the percentage of Fe and Ni on B-site in BGLC587. Ni-content increases from left to right. **B)** Unit cell volume of the phases from A). The dotted lines represents the unit cell volumes reported in literature (found through the Inorganic Crystal Structure Database, ICSD). Experimental data were found by Rietveld refinement.*

Ling et al. found a unit cell volume of 602.9 $Å^3$ for the $La_3Ni_2O_7$ at 300 K [82], which is higher than any of the values found for this phase. This can be a consequence of the smaller Gd^{3+} cation substituting La^{3+}. In general, Ni seems to have little effect on the unit cell volume of the

BGC phase, because the largest changes observed in Figure 5.5 B come with increasing Fe content. The LC phase on the other hand, has an increasing unit cell volume with Ni-content as was also seen with Fe substitution. Huang, Lee and Goodenough also reported structural parameters indicating an increase in unit cell volume of $LaCoO_3$ with 40 at.% Ni [83]. The NiO_x phase has a significantly larger unit cell than what can be found in literature where Sasaki et al. found it to be 72.93 $Å^3$ [84]. The presence of Co and Fe can of course play a part in this result.

Z-Contrast Imaging of Fe and Ni Substituted Samples

Since some of the phases found from Rietveld refinement have a different A-site to B-site ratio, they also have a different average atomic number (*Z*). As discussed above, this is because the A-site atoms (Ba, La and Gd) have a significantly larger *Z* than the B-site atoms (Fe, Co or Ni). The variation within the A-site and the B-site atoms are not that big and we therefore assume that all A-sites have a *Z* equal to La and all B-sites have a *Z* equal to Co. When doing this, we find the average atomic number and molar mass of the Ruddlesden-Popper, perovskite and NiO phases to be as in Table 5.1.

Table 5.1: The average atomic number ($\bar{Z}$) and average molar mass ($\bar{M}$) of the stoichiometric Ruddlesden-Popper (RP), perovskite (LC/LF/GLC/BGC) and Ni O phases. Column four specifies which region in Figure 5.6 corresponds each phase corresponds to.

Phase	$\bar{Z}$	$\bar{M}$ **(u)**	**Region in Figure 5.6**
RP	23	54	1
LC/LF/GLC/BGC	22	49	2
NiO	18	27	3

The phases with higher average *Z* will show up as bright, whereas phases with lower average *Z* will show up as dark. Figure 5.6 shows SEM micrographs of BGLCFN1040 and BGLCN50 taken with the BSE detector. In both images we can clearly distinguish three regions with different contrast, which are not distinguishable in the SE micrographs. From the contrast of these, we suggest that region 1 is the RP-phase, as this has the highest $\bar{Z}$. Region 2 is then the perovskite phase and region three is NiO. Region (4) indicates the small nanoparticles present at the surface of both the RP and perovskite phases, which are not present at the NiO phase. However, the contrast of these are in any case not trivial to compare, since the particles are so small and scattering effects such as edge effects may also contribute.

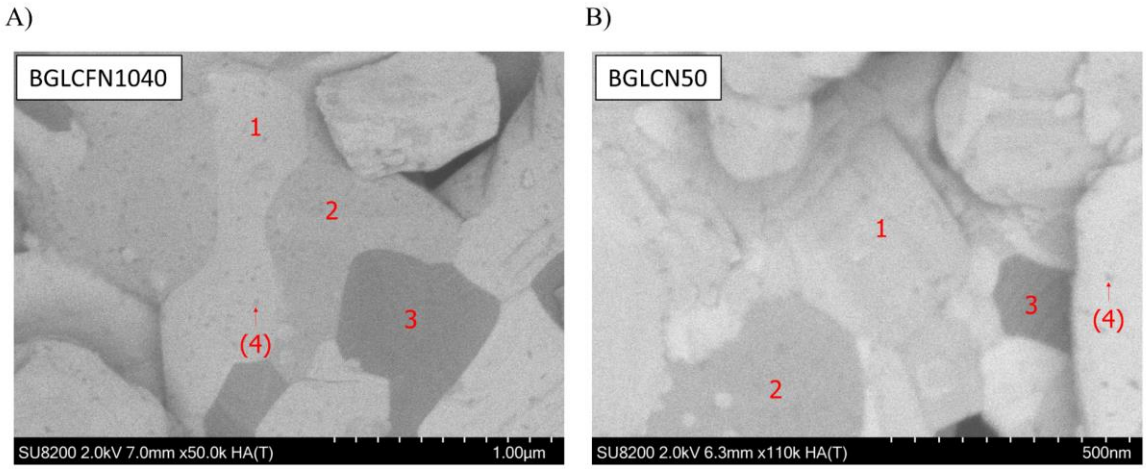

*Figure 5.6: SEM micrographs showing Z-contrast in **A)** BGLCFN1040 and **B)** BGLCN50.*

Both BGLCFN1040 and BGLCN50 presented above have a high amount of Ni on B-site (40% and 50% respectively) and hence also the highest wt.% of the RP and NiO phases. Figure 5.7 A and B show SEM micrographs, taken in the same way as in Figure 5.6, of the two other materials; BGLCFN2010 and BGLCFN3020 with 10% and 20% Ni respectively. The former showed no presence of the RP phase from the refinement in Figure 5.5 and only a little bit of NiO. This we observe by the lack of regions with distinguishable contrast in Figure 5.7 A.

On the other hand, BGLCFN3020 had more or less equal amounts of the perovskite and RP phases and a more pronounced NiO phase. From Figure 5.7 B we see one very distinct dark region which we attribute to the NiO phase (3). The two other phases are less distinguishable and by evaluating the topography of the area within the red square (from SE image in the inset), it is difficult to say if the difference is due to topographical effects or *Z*-contrast.

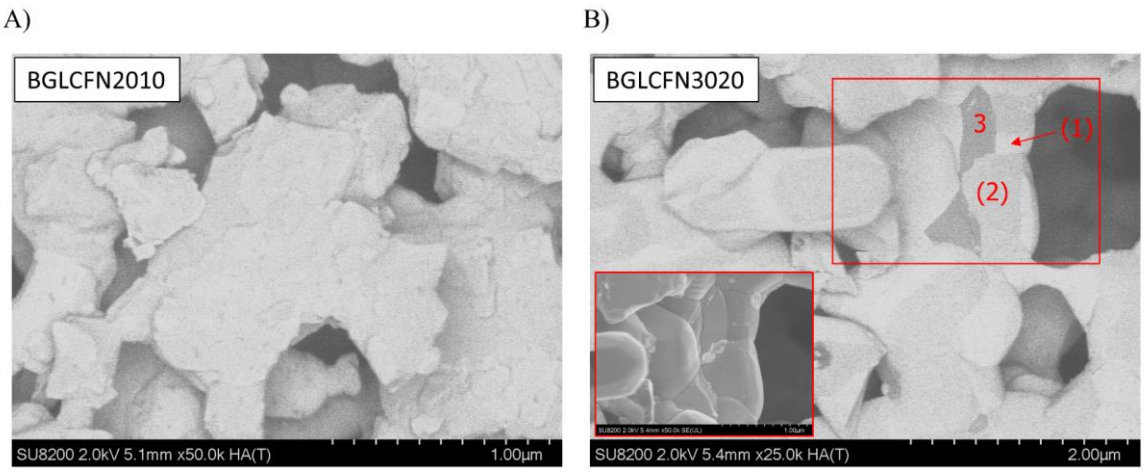

*Figure 5.7: SEM micrographs showing Z-contrast in **A)** BGLCFN2010 and **B)** BGLCFN3020. The inset in B) gives the SE image of the area indicated with the red square.*

In conclusion, the SEM analyses support the presence of up to three phases with different average *Z* as found from the XRD measurements. Moreover, the validity of the phase compositions found for the Ni substituted samples by Rietveld refinement is further corroborated by the *Z*-contrast imaging.

BGLC587 Annealed in NH_3

The PXRD of BGLC587 annealed at 400°C in NH_3 (BGLC-NH_3) is difficult to interpret because many new peaks emerged and the BGLC587 pattern is lost completely. As can be seen in Figure 5.8 only a couple of the peaks were identified with fingerprint identification in EVA. These were the cubic phases of BaO and metallic Co as well as a tetragonal CoPt phase.

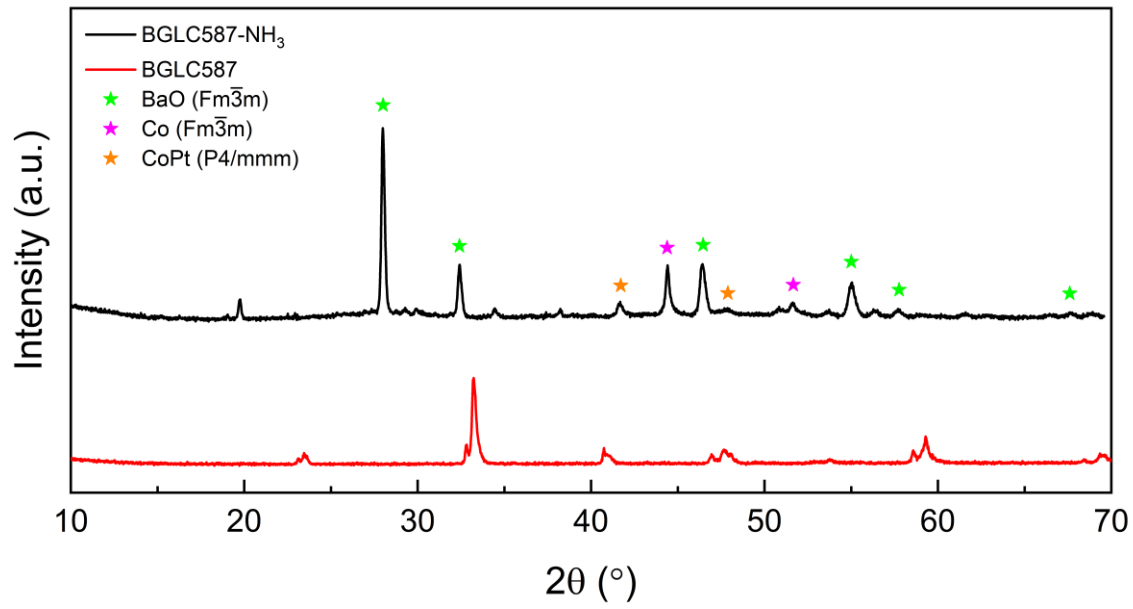

Figure 5.8: PXRD pattern of BGLC-NH_3 annealed at 400°C in NH_3 compared to the pristine BGLC587.

The reduced oxidation state of Ba and Co in these materials is likely due to the reducing ammonia atmosphere and the elevated temperature during synthesis, which may cause exsolution of particles or phase segregation. The SEM micrographs in Figure 5.9 A and B show the surface of BGLC-NH3 taken using a secondary electron (SE) detector and a backscatter electron (BSE) detector respectively. The contrast in the BSE micrograph gives atomic number contrast (*Z*-contrast) and it is therefore likely that dark and light areas represent two different phases. Since Ba, Gd and La have fairly similar Z and Co has a much lower *Z*, it is fair to assume that the darker areas are more Co-rich. Looking at Figure 5.9 A, we can see that the Co-rich regions form a layer on top of the Co-poor regions, strengthening the theory that Co

precipitated out of the structure during annealing. Whether it is pure Co or an alloy with Ba, Gd or La is not clear from these finding alone. Together with the XRD results, this led to the conclusion that the structure of BGLC587 is significantly altered under the annealing conditions and that the temperature and annealing time should be lowered in order to obtain a successfully N-doped material.

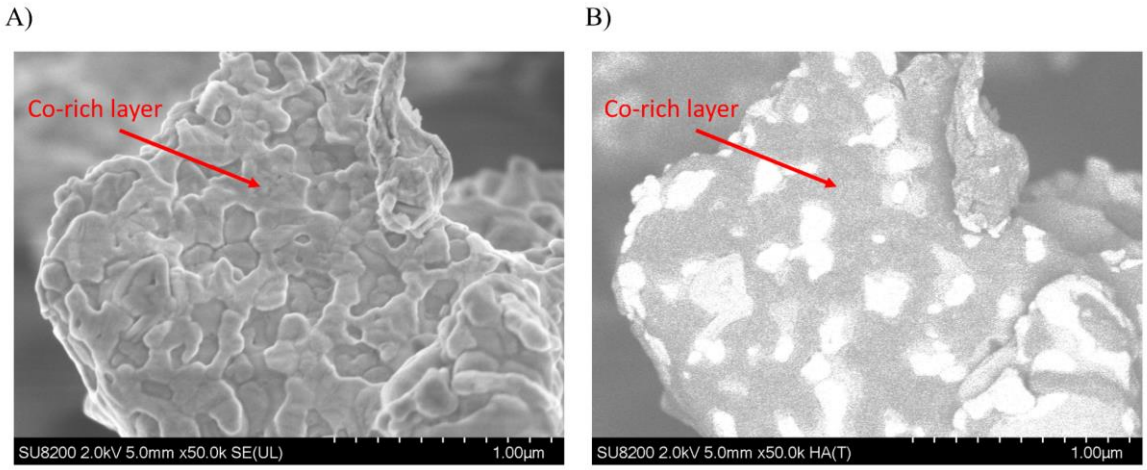

*Figure 5.9: **A)** SEM micrograph of BGLC-NH3 taken with a SE detector, giving topographical contrast. **B)** SEM micrograph of the same region as in A) taken with a BSE detector, giving Z-contrast.*

5.1.2 Topography and Microstructure

This subchapter presents macro- and microstructural properties of the B-site substituted electrocatalysts, such as porosity, grain sizes and particle facets through secondary electron SEM imaging.

Fe Substitution

Secondary electron SEM micrographs of BGLC587 with 0-100% Fe substitutions are shown in Figure 5.10 A-F. Taking BGLC587 as a starting point, we can see from the left image that it is a macroporous material due to pore diameters well above 50 nm. From the magnified image (right) we observe that BGLC587 has a complex microstructure on the surface. Grain sizes ranging from ~500 nm to ~10 nm are clearly visible on its surface. It is clear that the smaller nanoparticle grains (<50 nm) have a tendency of being localised at the surface of the larger grains (>100 nm), whereas the intermediate sized grains are more randomly distributed.

As the Fe content in BGLC587 increases from 0-100% in Figure 5.10, a notable change is observed in the porosity of the electrocatalysts. Since this may impact the surface area, this is important to assess. We find that a likely trend is that the pore sizes decrease with Fe content, while the number of pores increase. This can be indicative of a larger surface area. BGLCF70 have a different type of networking between the particles and is harder to place, however it looks more porous than BGLCF50 and less porous than BGLF.

From the higher magnification images we can observe the evolution of the microstructure. The overall trend seems to be that the grain sizes decreases with Fe content and the larger ones become less faceted. However, the exception is the nanoparticles found at the pristine BGLC587. These are observed to decrease in amount when going from 0-30% Fe and eventually disappear completely above 50% Fe. This can be an indication that these small NPs are Co-containing. Detection of Co-enrichment in these with energy dispersive spectroscopy (SEM-EDS) was tried, though with scarce results. This was because of the high accelerating voltage (~10 eV) resulted in a big interaction volume compared to the NPs on the surface. Lowering the acceleration voltage was also tried, but this only resulted in too low count rates.

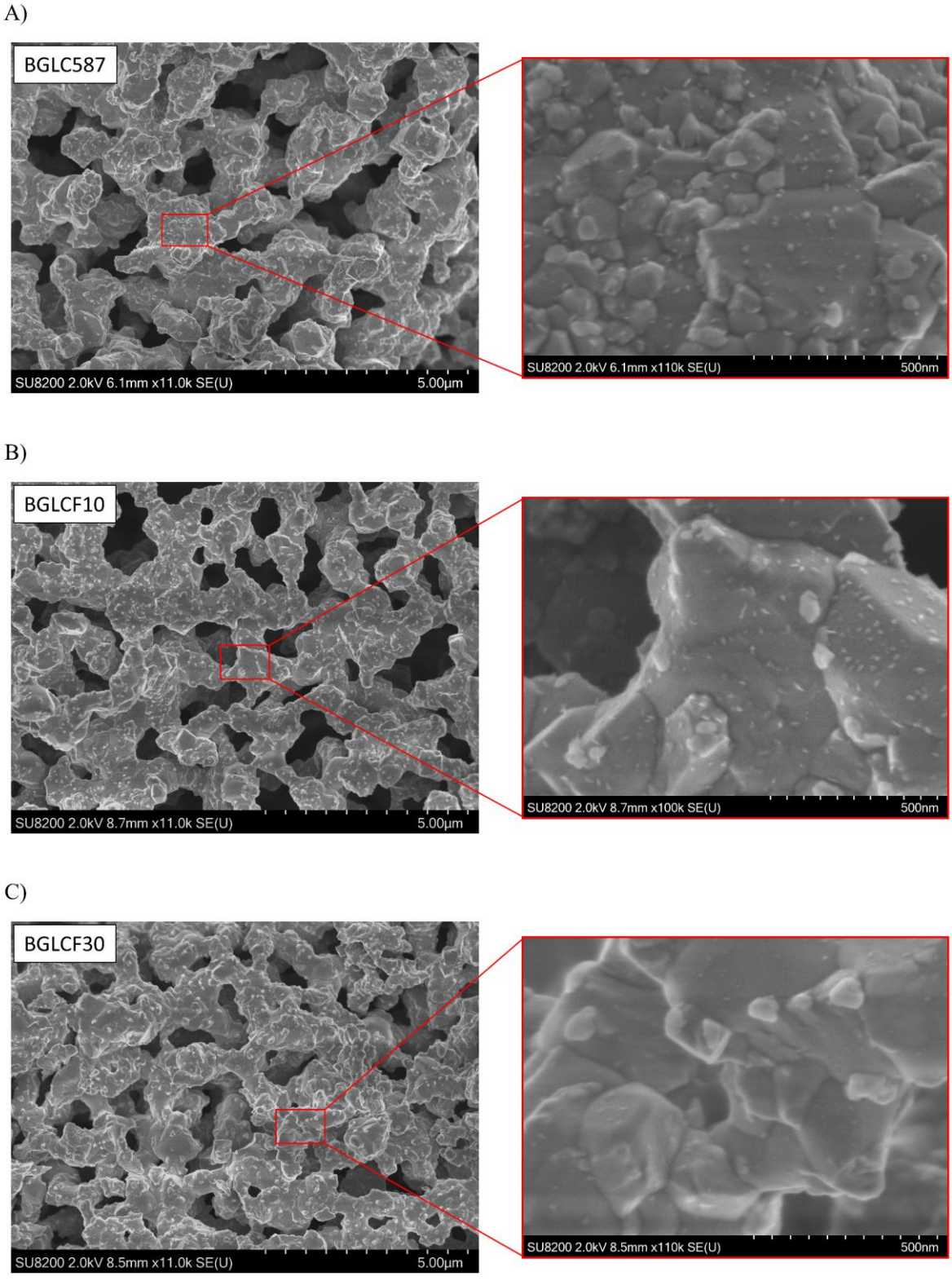

*Figure 5.10 A-B: Secondary electron SEM micrographs of **A)** BGLC587, **B)** BGLCF10 and **C)** BGLCF30.*

D)

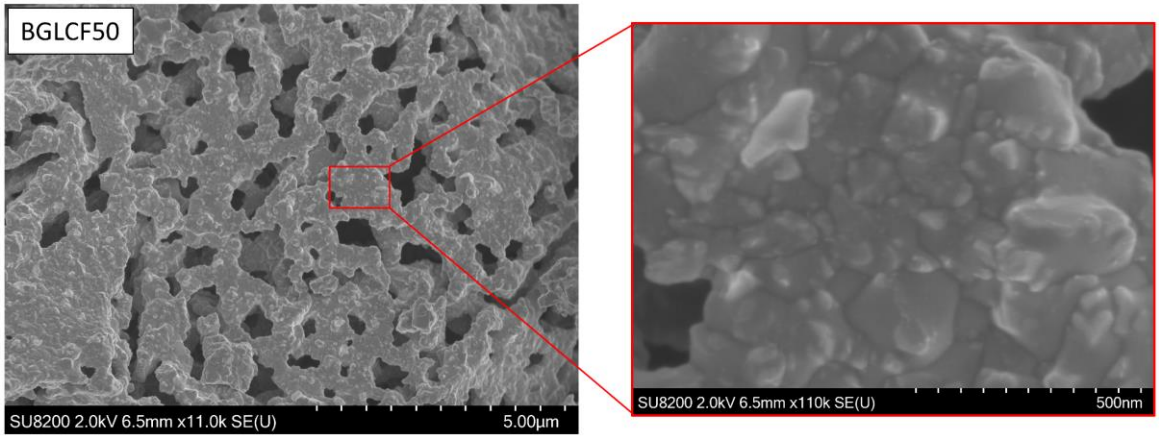

E)

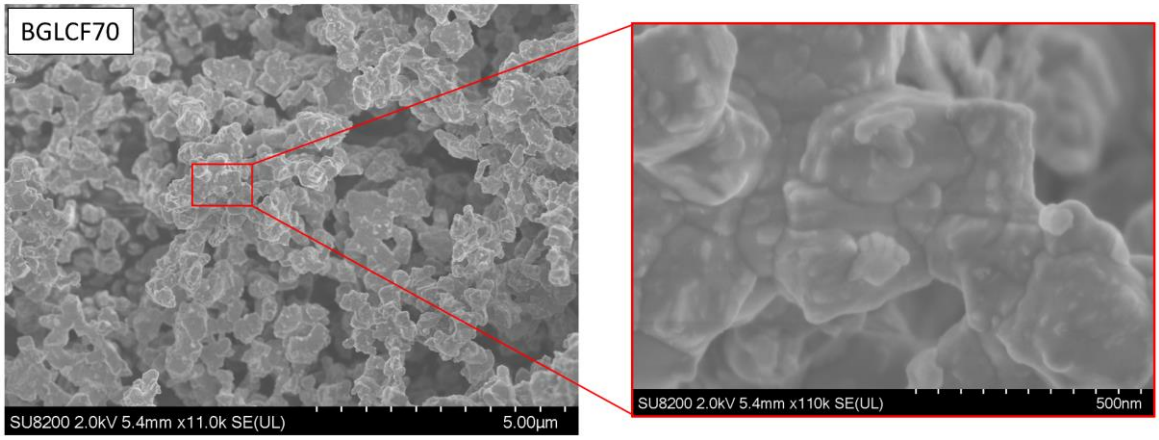

F)

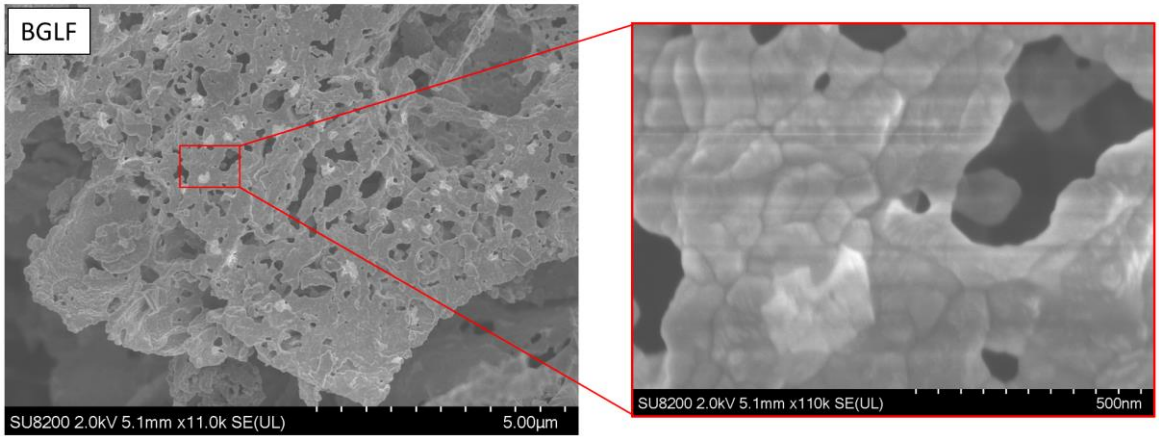

*Figure 5.10 D-F: Secondary electron SEM micrographs of **D)** BGLCF50, **E)** BGLCF70 and **F)** BGLF.*

Ni and Fe Substitution

The introduction of Ni on B-site proved to change the phase composition in BGLC587 substantially. It is also interesting to see how Ni and the mix of Ni and Fe affects the morphology of BGLC587. Figure 5.11 A-F gives the SEM micrographs acquired for BGLCN10, BGLCN50, BGLCFN1020, BGLCFN2010, BGLCFN1040, BGLCFN2010 and BGLCFN3020 respectively. With only 10% Ni substitution (Figure 5.11 A), there are no notable changes in the porosity or the microstructure of the material. However, there is a slight change in morphology, because some grains look slightly more faceted. At higher Ni content, such as in BGLCN50 (Figure 5.11 B), the amount of clearly faceted grains increases. It was found that some facets had NPs on the surface, whereas some of them where completely clean. From this it was hypothesised that the NPs precipitate from larger particles during synthesis, but that the facets have different selectivity towards this precipitation.

As opposed to the Fe substituted electrocatalysts in Figure 5.10, the difference in porosity of these electrocatalysts is harder to evaluate. Almost all of them look quite similar, with the exception of BGLCN50 and BGLCFN2010, which might have a higher surface area than the others. Since the microstructure of the samples in general consists of grains with large size differences, it is complicated to find a trend with composition. Though, comparing the micrographs to that of the pristine BGLC587 in Figure 5.10 A, we can argue that Ni-content increases the grain sizes in general.

The location of the three phases with different average Z (presented in Table 5.1) is given in the higher magnification micrographs (right) of BGLCN50 and BGLCFN1040. What we can see from these images, is that the NiO phases (3) have no precipitates at the surface. In fact, it was found that whenever the NiO phase was seen in the SEM, it always had a clean surface. This could indicate that there is a stable phase at higher temperatures from which the NiO phase precipitates, for example during cooling. This theory is however hard to validate solely from these micrographs and one could for instance do in situ X-Ray diffraction at high temperatures to resolve this.

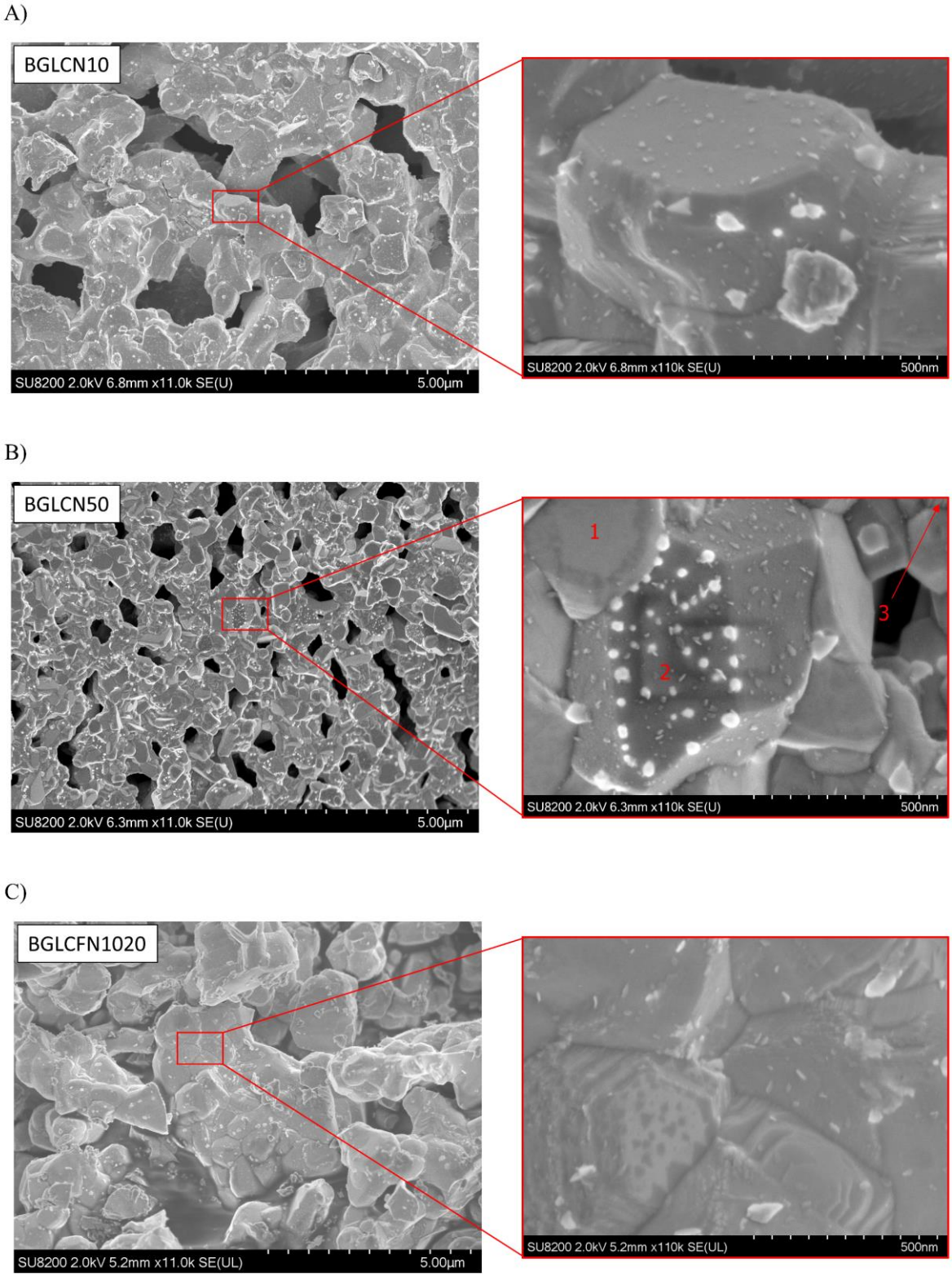

*Figure 5.11 A-C: Secondary electron SEM micrographs of **A)** BGLCN10, **B)** BGLCN50 and **C)** BGLCFN1020. Numbers indicate the location of phases observed from Z-contrast imaging.*

D)

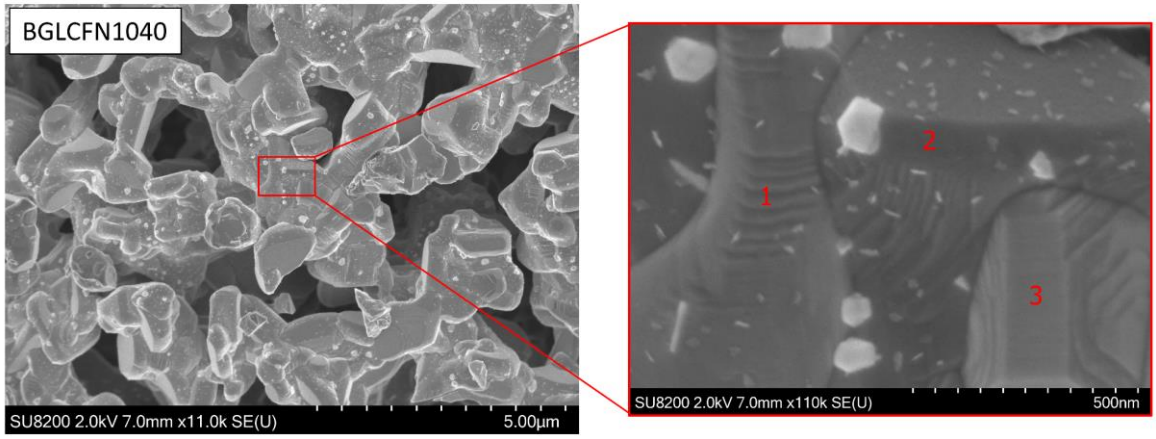

E)

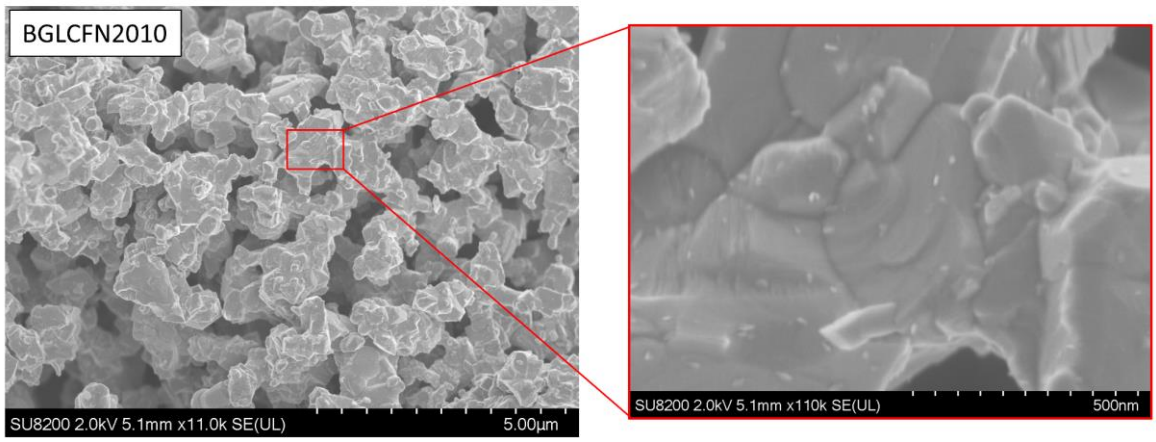

F)

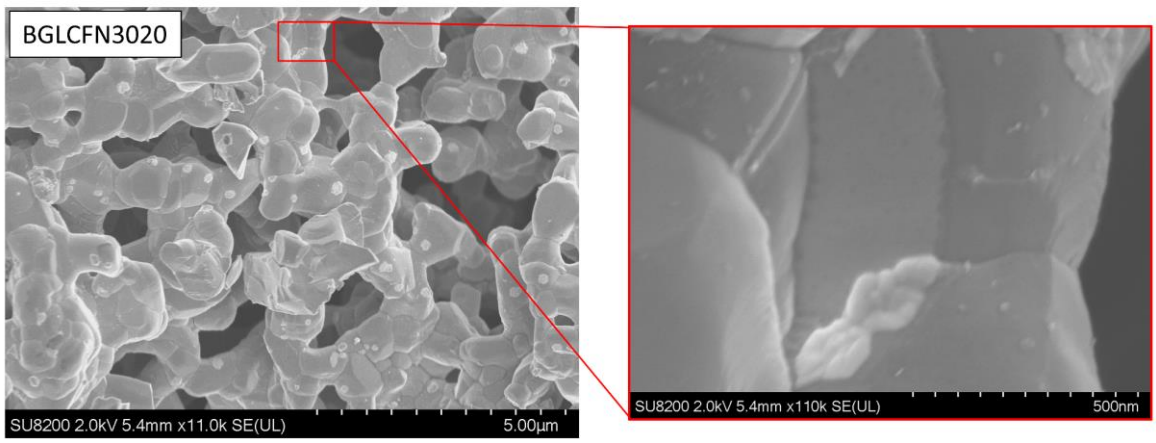

*Figure 5.11 D-F: Secondary electron SEM micrographs of **D)** BGLCFN1040, **E)** BGLCFN2010 and **F)** BGLCFN3020. Numbers indicate the location of phases observed from Z-contrast imaging.*

5.1.3 Elemental Composition

In the following subsection, we present the results from elemental quantification and mapping of the electrocatalysts by the use of EDS in the SEM and TEM instruments.

SEM-EDS

From EDS measurements in general, there were no indications of elemental impurities in the investigated samples. This is shown in Figure 9.2 in Appendix, where a representative EDS spectra is given for BGLCF70, containing no unknown peaks. The other spectra had the same trend and are therefore not given. From this it was concluded that the synthesis process was successful in terms of purity of the prepared samples.

Table 5.2: Mean molar fractions (χ_i) of the elements in the some of the B-site substituted BGLC587. The values where acquired with EDS from three different areas of the catalyst powders. The errors are statistical and based on the three individual measurements. Values in red are the nominal molar fractions.

Electrocatalyst	A-site			B-site		
	χ_{Ba}	χ_{Gd}	χ_{La}	χ_{Co}	χ_{Fe}	χ_{Ni}
BGLC587	0.51 ± 0.01 0.5	0.71 ± 0.04 0.8	0.73 ± 0.02 0.7	2.05 ± 0.02 2.0	-	-
BGLCF10	0.51 ± 0.5 0.5	0.72 ± 0.06 0.8	0.73 ± 0.05 0.7	1.85 ± 0.04 1.8	0.19 ± 0.01 0.2	-
BGLCF30	0.5 ± 0.1 0.5	0.73 ± 0.09 0.8	0.68 ± 0.09 0.7	1.5 ± 0.1 1.4	0.57 ± 0.08 0.6	-
BGLCF50	0.50 ± 0.02 0.5	0.73 ± 0.01 0.8	0.70 ± 0.01 0.7	1.06 ± 0.02 1.0	1.02 ± 0.02 1.0	-
BGLCF70	0.59 ± 0.06 0.5	0.77 ± 0.04 0.8	0.71 ± 0.04 0.7	0.65 ± 0.03 0.6	1.38 ± 0.03 1.4	-
BGLF	0.52 ± 0.01 0.5	0.78 ± 0.01 0.8	0.72 ± 0.02 0.7	-	1.99 ± 0.02 2.0	-
BGLCFN2010	0.48 ± 0.08 0.5	0.73 ± 0.02 0.8	0.7 ± 0.1 0.7	1.5 ± 0.09 1.4	0.41 ± 0.02 0.4	0.21 ± 0.04 0.2
BGLCFN3020	0.53 ± 0.01 0.5	0.75 ± 0.02 0.8	0.76 ± 0.06 0.7	1.04 ± 0.02 1.0	0.60 ± 0.03 0.6	0.32 ± 0.03 0.4
BGLCN50	0.51 ± 0.01 0.5	0.8 ± 0.1 0.8	0.76 ± 0.01 0.7	1.08 ± 0.06 1.0	-	0.88 ± 0.2 1.0

Table 5.2 shows the elemental quantification data of Ba, Gd, La, Co, Fe and Ni atoms in the synthesised samples as found from EDS. When comparing the theoretical mole fractions (red) to the experimental ones, we see that there is overall a good agreement. Some values, such as the Fe content in BGLCF30, deviates with as much as 0.1 mole fractions. However, since rough powder samples are not ideal for EDS measurements, this was not found worrying. In general, it looks like the mean values for Ba, La, Co, Fe and Ni content lies close to the theoretical ones

and that the Gd content is perhaps somewhat underestimated. Nonetheless, it can be concluded that there were no errors in the calculation of the stoichiometry during synthesis. All the errors are given in Table 5.2 and are well within the expected range in such a measurement.

STEM-EDS

The elemental quantification presented in Table 5.2, was done with SEM-EDS at a rather macroscopic area (at least 5x5 μm). This means that the information is more of an average values, which is appropriate when validating the composition with respect to the chemical formula. However, it has been discussed previously how the perovskite electrocatalysts in this work consists of several phases and how the grain sizes vary significantly. It is therefore important to see how the elements are distributed on a smaller scale. Hence, we used the TEM in the scanning transmission electron microscope (STEM) mode to carry out EDS mappings with higher spatial resolution. The result can be seen in Figure 5.12 and Figure 5.13, which show elemental mappings of a particle in BGLC587 and BGLCF70 respectively.

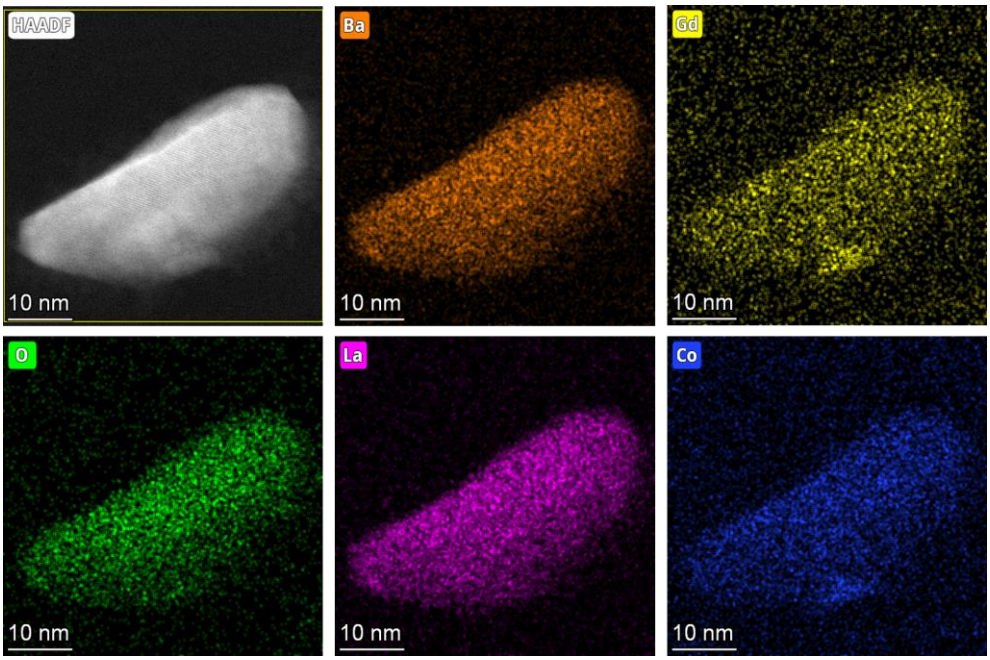

Figure 5.12: STEM-EDS mapping of a particle in BGLC587.

Both Figure 5.12 and Figure 5.13 show that all the elements in the chemical formulas of the electrocatalysts are present in a substantial amount. This proves that, in the case of BGLC587 where the majority phase was found to be $LaCoO_3$, we have both Ba and Gd dissolved in this phase. The particle of BGLCF70 investigated in Figure 5.13 is most probably polycrystalline and it is not easy to say which phases are present. However, we can conclude that also here, the atoms are mixed quite homogeneously.

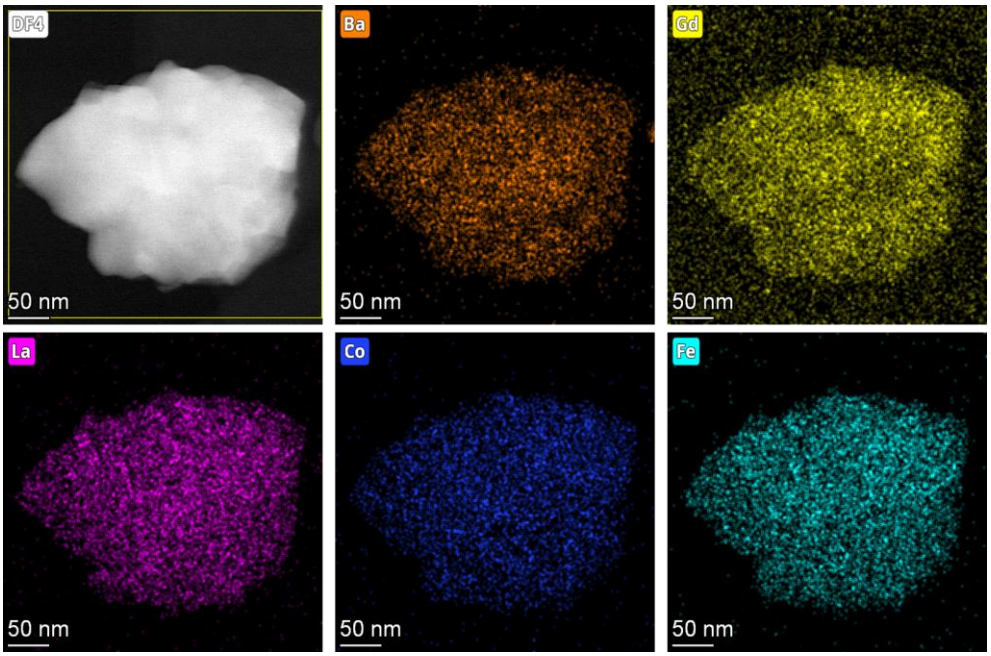

Figure 5.13: STEM-EDS mapping of a particle in BGLCF70.

5.1.4 BET Surface Area

The Brunauer-Emmet-Teller (BET) surface areas of the B-site substituted BGLC's are given in Figure 5.14. From the black line it can be seen that the surface area of the samples increases with increasing Fe-content, which is in good agreement with the trend found in the SEM. Samples with 0-70% Fe seem to increase rather linearly, whereas a bigger increase is observed in the composition with 100% Fe. The trend is similar to the results found by Wang et al. upon doping $LaCoO_3$ with Fe [85], however another result from Duan et al. found the change to be more fluctuating [78]. Still, it is important to note that the synthesis temperatures used in these two works were very different and can be significant.

We therefore find it reasonable that the observed trend in BET surface area is a result of the incorporation of Fe. Since we see an increase in the orthorhombic (*Pnma* and *Pbnm*) phases with Fe content, we have included the summed wt.% of the GLC and LF phases in Figure 5.14. This trend seems to correlate somewhat with the BET surface area. The two phases are summed because they alone do not show any comparable trend and as discussed earlier, they might even be the same phase.

The inset in Figure 5.14 presents the BET surface area of all the Fe- and Ni-substituted samples together in a contour plot. From this, one can see that Ni has little impact on the surface area as it is relatively constant. However, there is a substantial increase with BGLCN50 (50% Ni)

which could indicate that even higher Ni-content favours higher surface area. The BET surface areas can also be found tabulated in Table 9.8 in the Appendix.

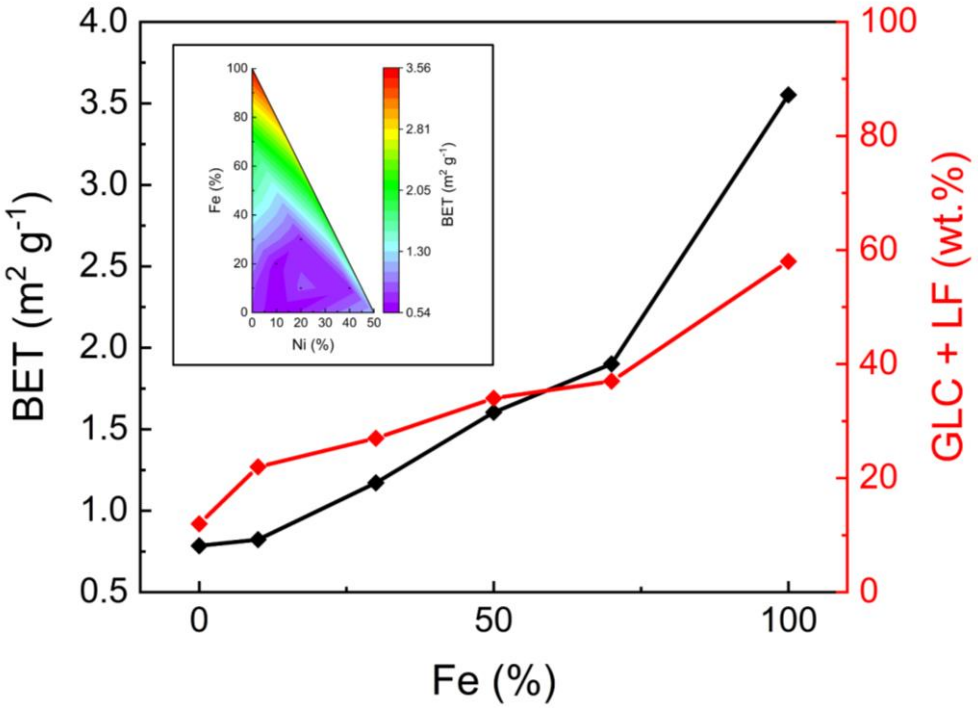

Figure 5.14: ***Black curve:*** *BET surface area of Fe-substituted BGLCs as a function of Fe-content.* ***Red curve:*** *Summed wt.% of the GLC and LF phases as a function of Fe-content.* ***Inset:*** *Contour plot of the BET surface area of all B-site substituted BGLCs.*

5.2 Electrocatalytic Activity

This subchapter presents the electrocatalytic performance of the synthesised electrocatalysts. We discuss the activity indicators such as overpotentials and Tafel slopes, as well as the charge transfer resistance and the double layer capacitance. Conclusively, we try to explain the observed results and correlate them to the physiochemical properties of the perovskite oxides.

5.2.1.1 Overpotentials and Tafel Slopes

Figure 5.15 A-F present the LSVs and Tafel curves of all the 17 electrocatalysts. A and B, C and D, E and F correspond to the purely Fe substituted, Fe and Ni substituted and A-site substituted ECs respectively. We will not focus on the A-site substituted ECs much, since they initially showed little improvement in OER activity from the LSVs and Tafel slopes compared to BGLC587. However, the overpotentials and Tafel slopes of these can be found together with all the other ECs in Table 9.3 in Appendix.

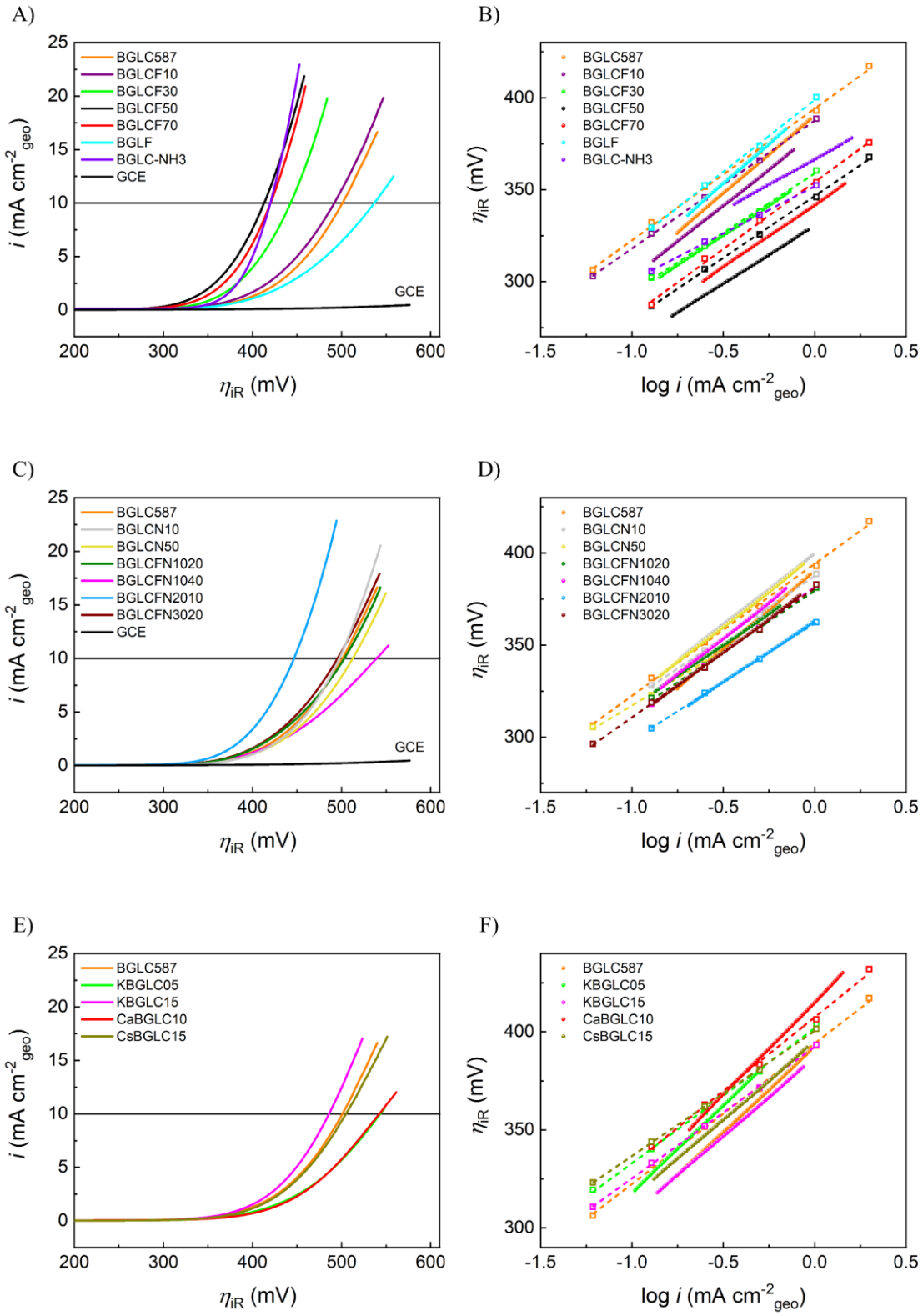

Figure 5.15: iR corrected LSVs (left) and corresponding Tafel slopes (right) of all electrocatalysts. ***A)*** *and* ***B)****: Fe substituted electrocatalysts plus BGLC-NH3,* ***C)*** *and* ***D)****: Ni and Fe substituted electrocatalysts and* ***E)*** *and* ***F)****: A-site substituted electrocatalysts. The dense curves in the Tafel figures are from the LSVs, whereas the open squares with dotted fittings are slopes from chronopotentiometry (CP) in the Tafel region.*

From the Tafel curves (left) in Figure 5.15, we observe that the Tafel region spans below one order of magnitude of i when derived from LSVs, but above one order of magnitude when derived from CP. This is expected, since the CP method approaches a steady-state in which the Butler-Volmer equation is applicable. In the case of the LSVs taken at a scan rate of 10 mV s^{-1}, which is not considered true steady-state, there will be a contribution from capacitive current disturbing the Butler-Volmer behaviour. As mentioned earlier, it is recommended to have a Tafel region spanning 1-2 orders of magnitude. Therefore, the Tafel slopes from CP is most likely to have the lowest experimental error. However, the Tafel slopes from LSV were done in triplicate and we therefore have a better knowledge of the statistical error in these. Based on this argument, we will consider the Tafel slopes from both methods in the following discussions.

The overpotentials at 10 mA cm^{-2}_{geo} from LSV of the purely Fe substituted ECs are presented in Figure 5.16 A. We observe that the overpotential reaches a minima of 428 mV at 50% Fe content, indicating an increased activity. However, increasing Fe content up to 100% seems detrimental. This can be correlated with the low intrinsic OER activity of Fe oxides estimated by Trasatti's volcano curves and M-OH bond strengths [42]. However, this does not account for possible synergetic effects between mixed transition metal oxides, which may be why we see an increased activity with lower Fe content. The BGLC-NH3 sample showed an overpotential of 429 mV, which was comparable with the Fe-samples. However, because of the unsuccessful N-doping procedure evident from XRD and SEM analyses, we will not discuss this composition much further.

Figure 5.16 B shows a ternary contour plot of the overpotentials of all the B-site substituted ECs. We observe that the highest activity lies close to the Fe-axis, indicating that Ni substitution does not increase the activity as much. The exception is however BGLCFN2010 with an overpotential of 451 mV, which is close to the best performing BGLCF50 and BGLCF70. This can be an indication that low Ni content in combination with Fe increases the OER activity, whereas higher content has the reverse effect. In comparison, She et al. found that 10% Ni substitution on B-site in $Sr_{0.95}Ce_{0.05}FeO_{3-\delta}$ (SCF) resulted in an increased OER performance [65]. They argued that Ni increases the electronic interaction between active sites and hence facilitates OER.

The Tafel slopes derived from LSV and CP are given in Figure 5.16 C as a function of Fe content. It is observed that the Tafel slopes from LSV coincide very well with the overpotentials in Figure 5.16 A. The Tafel slopes from CP have a similar trend, but with a peak activity around 30% Fe instead of 50%. It is also observed that the Tafel slopes from CP in general lie lower than those from LSV. This coincides well with what was discussed by Anantharaj et al. regarding Tafel slopes [33], where they showed that Tafel slopes of a Pt/C catalyst were lower when extracted from LSV compared to CA and EIS. The Tafel slopes from LSV of all the B-site substituted ECs are given in the ternary contour plot in Figure 5.16 D. We also observe, that the Tafel slopes correspond well with the overpotentials, presented in Figure 5.16 B.

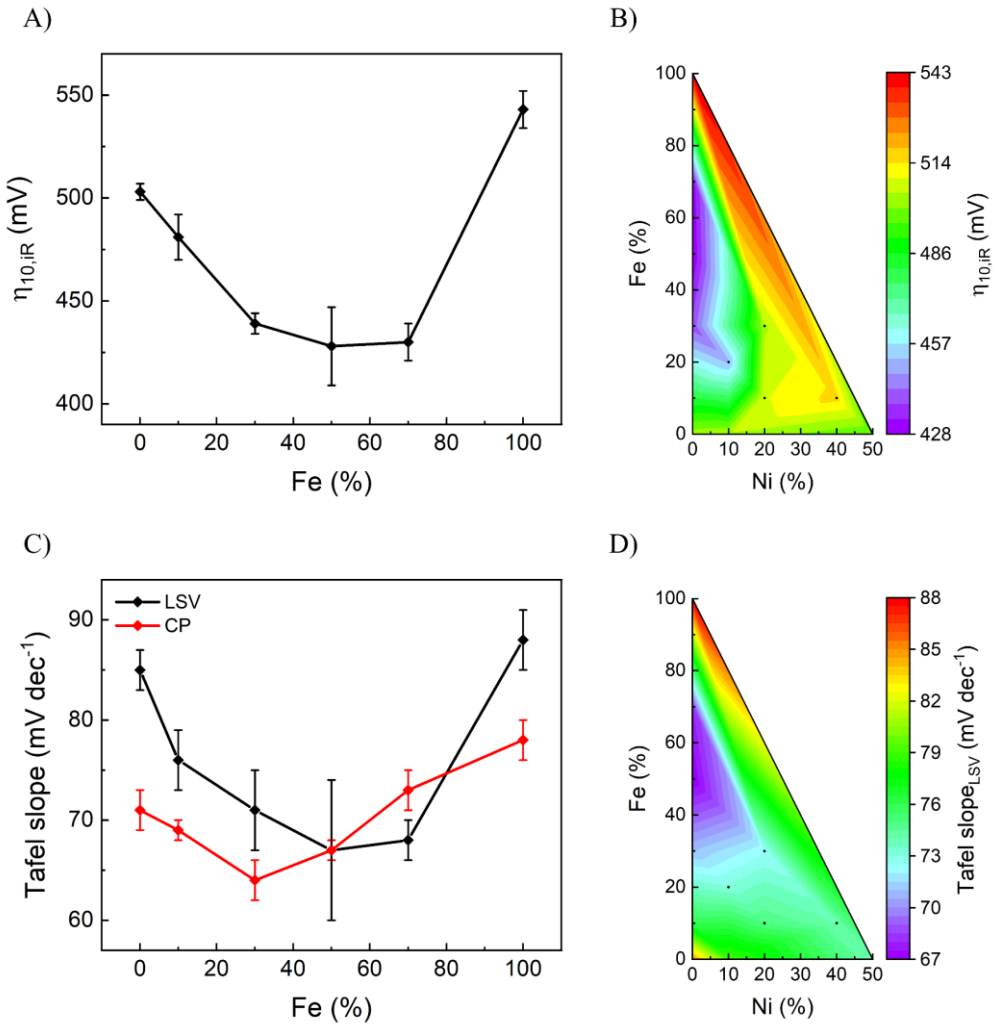

*Figure 5.16: **A):** Overpotentials at 10 mA cm$^{-2}_{geo}$ for the Fe substituted ECs, **B):** contour plot of the overpotentials at 10 mA cm$^{-2}_{geo}$ for all the B-site substituted ECs, **C):** Tafel slopes of the Fe substituted ECs from both LSV and CP and **D):** contour plot of the Tafel slopes of all the B-site substituted ECs. All values are mean values from three independent measurement, with the exception of Tafel slopes from CP, which are from a single measurement.*

Based on the Tafel slopes, we can suggest a rate determining step (rds) from the reaction paths of the adsorbate evolution mechanism (AEM) in Table 2.1. The initial reaction in all these OER paths is simply the adsorption and oxidation of hydroxide on the transition metal, M, as can be seen in Equation (5.1). This reaction has an assigned Tafel slope of 120 mV dec^{-1}.

$$M + OH^- \rightarrow MOH + e^- \tag{5.1}$$

However, this Tafel slope is higher than the 85 mV dec^{-1} found for BGLC587. The next closest reaction step has a Tafel slope of 60 mV dec^{-1}. According to path (2) and (3) in Table 2.1, this describes the deprotonation of the adsorbed hydroxyl and formation of water as shown in Equation (5.2).

$$MOH + OH^- \rightarrow MO^- + H_2O \tag{5.2}$$

This means that the rds of BGLC587 is a combination of the one-electron-transfer reaction in Equation (5.1) and the chemical (no electron-transfer) reaction in Equation (5.2). As the Tafel slopes decreases with increasing Fe content in Figure 5.16, it approaches a value of 60 mV dec^{-1}. Thus, we conclude that the introduction of up to 70% Fe in BGLC587 moves the rds in the direction of the proton-transfer reaction.

A significant finding by Shinagawa et al. was that the theoretical Tafel slopes can vary significantly with site coverage [86]. In fact, several calculated Tafel slopes are based on a purely 0 or 100% surface site coverage by the adsorbed intermediates, even though the Tafel slopes are very much coverage-dependant. This resulted in all the possible Tafel slopes of the Shinagawa path in Table 2.1. The 4th step (proton-transfer) of the Shinagawa path can also have a Tafel slope of 60 mV dec^{-1} and hence at this point, we cannot exclude this as a possible candidate. Nonetheless, we find it hard to imagine that the complex structure and morphology of the ECs in this work to have a perfect site coverage.

Another intuitive argument is that the (up to four) different phases in the ECs can have their own rds and hence contribute differently. In fact, some electrocatalysts may perform OER through the lattice oxygen mechanism (LOM) and hence dismantle the validity of the AEM reaction paths completely. The LOM mechanisms may in principle have its own reaction paths with designated Tafel slopes contributing to the observed values. We therefore conclude that it is not surprising that the Tafel slopes lie outside the theoretical values.

5.2.2 Electrochemical Impedance Spectroscopy

Figure 5.17 A-F give Nyquist plots from EIS of all the electrocatalysts at 10 mA cm^{-2}_{geo} (A-C), the onset overpotential (D-F) and the non-Faradaic (capacitive) region (G-I). The values from deconvolution of the EIS data can be found in Table 9.5-Table 9.7 in Appendix. We see that the large semicircles (mid-frequencies) assigned to the interfacial charge transfer resistance (R_{int}) and capacitance (C_{int}) of the electrocatalysts vary with applied potential. During OER at 10 mA cm^{-2}_{geo} we find the resistances to be between 10-40 Ω, compared to several hundred Ohms at the onset potential and a complete blocking behaviour in the capacitive region.

The semicircles at higher frequency (shown in insets) are ascribed to the resistance (R_d) and capacitance (C_d) associated with a surface passivating layer [40]. The value of R_d varies from 2-40 Ω depending on the catalyst material and the applied potential. This is a smaller variation compared to the one observed for R_{int}. From this we conclude that the value of R_d becomes more significant at higher OER potentials when R_{int} also becomes small.

Double Layer Capacitance and ECSA

An electrochemical property which may be indicative of trends in intrinsic activity of ECs is the electrochemically active surface area (ECSA). The calculated double layer capacitances can be found in Table 9.8 in Appendix. ECSA is proportional to the double layer capacitance C_{dl}, we report these as extracted from both EIS and cyclic voltammetry. We must highlight that we observe a significant spread in the C_{dl} extracted from repeated measurements for the same ECs with both CV and EIS. This puts a limitation on the reliability of our resulting capacitances and we will therefore mainly investigate their trends.

Figure 5.18 A gives the C_{dl} of the Fe substituted ECs found with EIS in the capacitive region, at the onset potential and at 10 mA cm^{-2}_{geo}. The lowest C_{dl} is found in the OER region, which is expected due to pore clogging and blocking of active sites by O_2 gas sticking to the catalyst surface [41, 87]. The highest C_{dl} is on the other hand observed in the onset potential, where less O_2 gas is evolved, but the interfacial charge transfer (R_{int}) initiates.

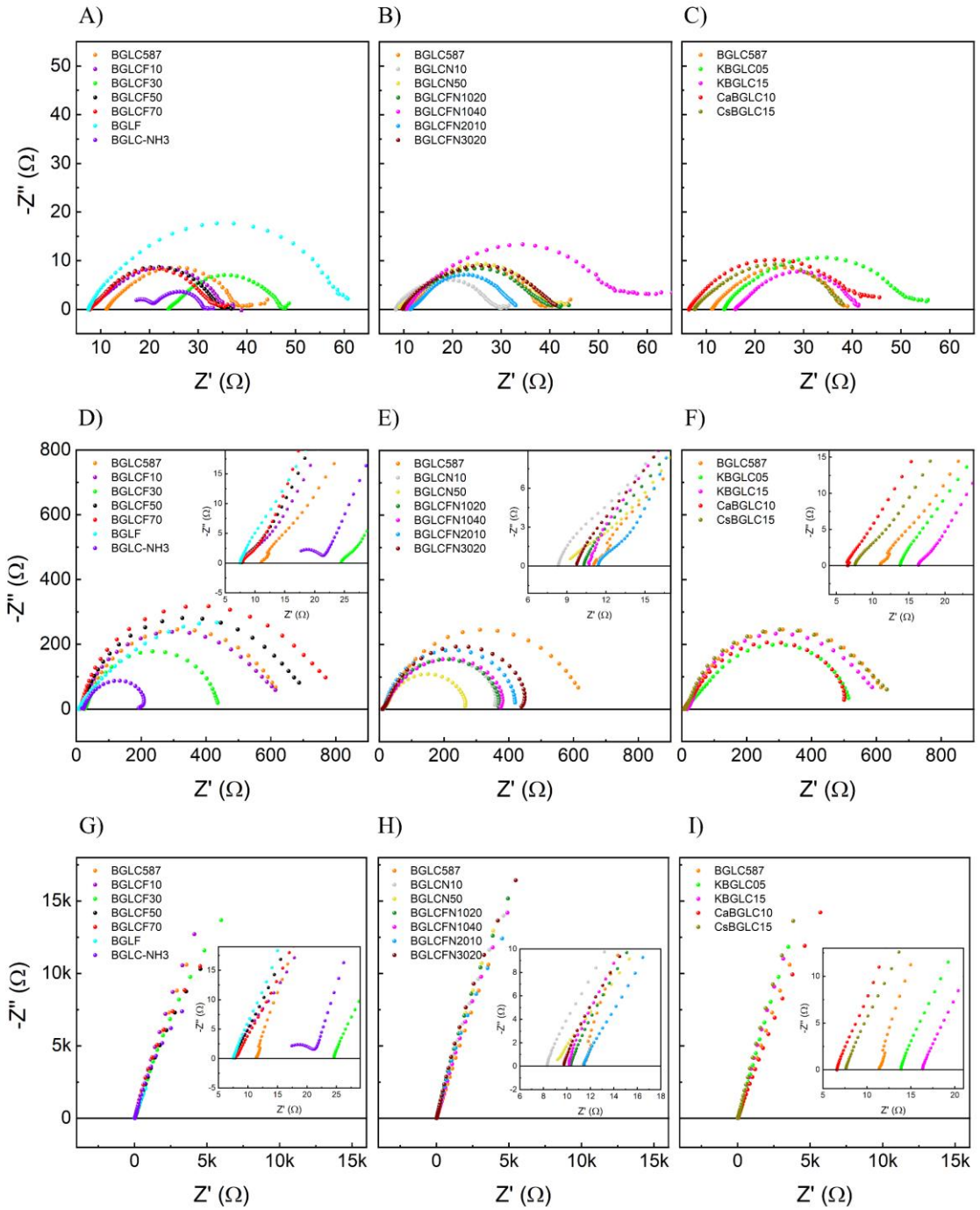

*Figure 5.17: Nyquist curves for all electrocatalysts obtained from EIS at **A)-C)**: 10 mA cm^{-2}_{geo}, **D)-F)**: the onset overpotential and **G)-I)**: the non-Faradaic (capacitive) region. The insets show the features in the high-frequency regions.*

Figure 5.18 B gives the double layer capacitances from cyclic voltammetry and EIS in the capacitive region. The capacitive current from CV exhibited one linear region at low scan rates and a second at high scan rates (see Figure 4.5 B). Capacitances extracted from low scan rates typically have a contribution from an "inner" capacitance, which is associated with less accessible surface of the electrode [88]. At higher scan rates, charged species do not have the

time to migrate to these "inner" surfaces and we observe a lower double layer capacitance as in Figure 5.18 B, which we call "outer" capacitance.

Comparing the C_{dl} from CV with EIS in the capacitive region, we find that the total double layer capacitance (sum of outer and inner capacitances), overlaps best with the data from EIS. The "outer" capacitance lies closer to the C_{dl} found during OER with EIS (Figure 5.18 A). We can therefore conclude that the "outer" double layer capacitance reflects better the ECSA in the OER region, compared to the total double layer capacitance.

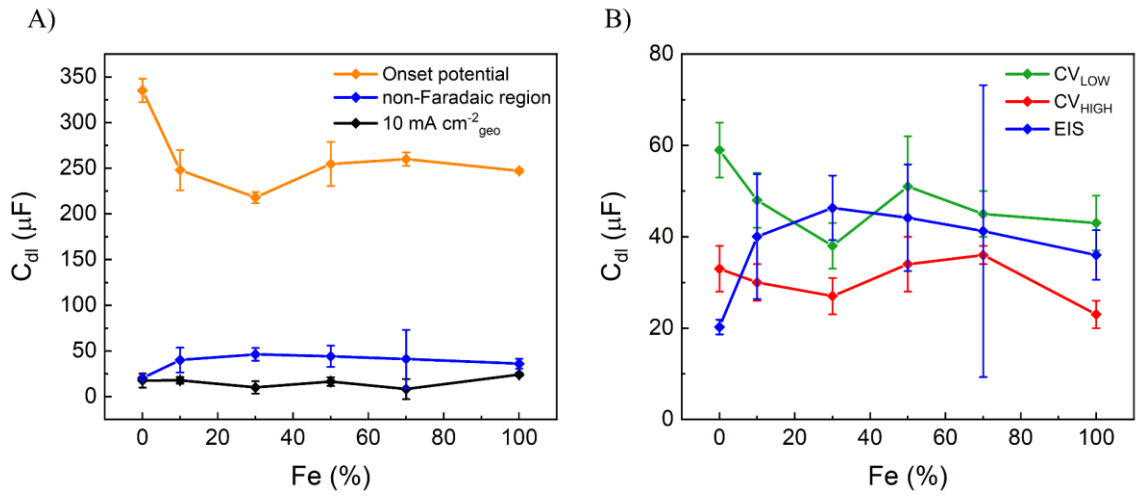

*Figure 5.18: **A)**: Double layer capacitance of the Fe substituted ECs in the non-Faradaic region (blue), at the onset overpotential (orange) and at 10 mA cm^{-2}_{geo} (black) as found from deconvolution of three independent EIS measurements. **B)**: Double layer capacitances measured in the non-Faradaic region by CV at both high (red) and low (green) scan rates and EIS (blue). All values are mean values from three independent measurements.*

It is interesting to compare the BET surface area and ECSA, since these are widely used to obtain specific activities (i_s or SA). In general, the double layer capacitance used to find ECSA can be influenced by the physical surface area, but it is also dependent on the chemical environment on the catalyst's surface. In Figure 5.14 we showed that the BET surface area increases with increasing Fe content almost linearly. Comparatively, the C_{dl} found with EIS in the non-Faradaic region has an initial increase from 0-30% Fe, whereupon it decreases almost linearly from 30-100% Fe.

The initial increase can likely be attributed to the increased BET surface area, but the decrease from 30-100% Fe is harder to explain. All we can say is that the deviation must be attributed to a competition between physical surface area and impact of Fe on the ECs ability to store electrical charge in the double layer.

Charge Transfer Resistance and the $R_{ct}C_{dl}$ Product

The charge transfer resistance as a function of Fe content is given in Figure 5.19 A. Compared to the Tafel slopes and overpotentials in Figure 5.16, we see that the trend of the R_{ct} correlates best with the Tafel slopes derived from CA. As mentioned, these Tafel slopes are in theory much more trustable, as they are acquired during a better steady-state. Combined with the R_{ct}, these two independently found activity descriptors should give a better description of the intrinsic activity of the electrocatalysts.

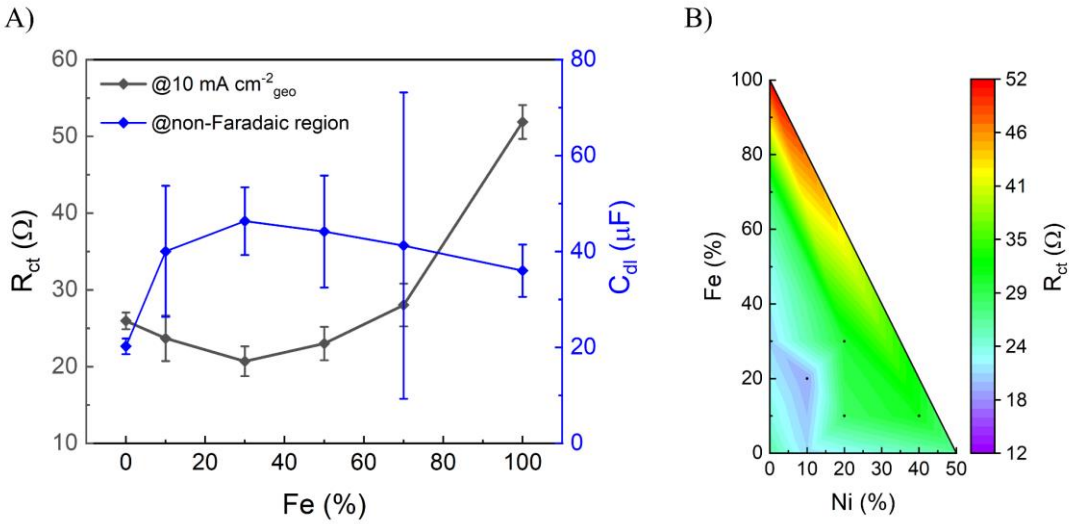

*Figure 5.19: **A):** The R_{ct} found at 10 mA cm^{-2}_{geo} (black) and the C_{dl} found in the capacitive region (blue) for the Fe substituted ECs and **B):** contour plot of the R_{ct} at 10 mA cm^{-2}_{geo} for all the B-site substituted ECs.*

Figure 5.19 A also shows the C_{dl} from EIS in the capacitive region. Of all the C_{dl} acquired from both EIS and CV, this trends best with the R_{ct}. We see that they have an inverse relationship, which could reflect how the OER depends on number of active sites (and ECSA). A similar inverse trend of the R_{ct} and ECSA was also found by Li et al. in IrO_x with different Nafion® concentration [89]. However, this was done with only one material with one specific intrinsic activity and hence it is not completely trivial to compare with the materials in this work. Either way, the trend is curious, and we therefore choose to consider this capacitance as an alternative to the C_{dl} during OER. As argued by Papaderakis et al. [41], this can be the best solution when the C_{dl} in the OER region is hard to determine precisely.

From the ternary contour plot in Figure 5.19 B, BGLCFN2010 presumably has the lowest R_{ct}. This is consistent with the low Tafel slope of 63 mV dec^{-1} (from CP) and overpotential of 451 mV, which places it among the top ECs in this work. In general, the R_{ct} seems to be lowest close

to the Fe-axis and hence follow the trend of the overpotentials and Tafel slopes in Figure 5.16 B and D, however slightly shifted towards lower Fe content.

Since we chose to evaluate the C_{dl} from EIS in the non-Faradaic region, we calculated the $R_{ct}C_{dl}$ product from this and the C_{dl} at 10 mA cm^{-2}_{geo}. In this work, we refer to the $R_{ct}C_{dl}$ product as the intrinsic catalytic activity (ICA), hence the lower the product, the higher the ICA. Calculated $R_{ct}C_{dl}$ products are given in Figure 5.20, where we can see that using these two capacitances results in two different trends. The $R_{ct}C_{dl}$ product with the C_{dl} outside the OER region indicates that ICA decreases with increasing Fe substitution. However, the ICA calculated with the capacitance within the OER region better corroborates the trends we found previously for the Tafel slopes and overpotentials. The error associated with the C_{dl} in the non-Faradaic region is also higher than those of the C_{dl} during OER.

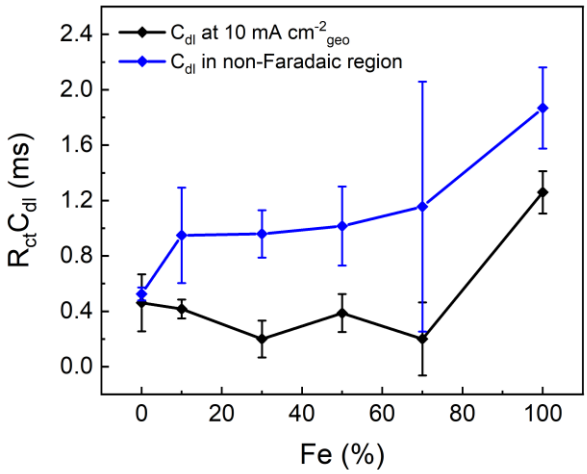

Figure 5.20: The $R_{ct}C_{dl}$ product of the Fe substituted ECs from the R_{ct} at 10 mA cm^{-2}_{geo} and the C_{dl} in the non-Faradaic (blue) and at 10 mA cm^{-2}_{geo} (black). All values are mean values from three independent measurements.

The contour plots in Figure 5.21 A and B, show that the two $R_{ct}C_{dl}$ products also vary with Ni content. Figure 5.21 A predicts the highest ICA for BGLC587 and BGLCFN2010 and that high Ni content is detrimental to the activity. Figure 5.21 B on the other hand, predicts increasing ICA with increasing Ni content up to BGLCN50. This increase is found to be due to the relatively low capacitances in the Ni-rich ECs during OER (see Table 9.8 in Appendix). Having said that, the capacitances of these were found to vary significantly (2-3 fold) between measurements compared to the Fe- and Co-rich ECs. Thus, looking past the Ni-rich region with

the biggest uncertainty, we find that Figure 5.21 B over all correlates well with the previously observed overpotentials and charge transfer resistances.

This observed compliance between methods strengthens the validity of the $R_{ct}C_{dl}$ as activity descriptor. Furthermore, we stress the importance of evaluating the double layer capacitance during OER conditions, seeing as it changes significantly with applied potential. This leaves the methods for acquiring ECSA at non-Faradaic potentials redundant and unsuitable. Hence, we come to the conclusion that the C_{dl} extracted during OER is a better surface area indicator of electrocatalysts, compared to ECSA measured outside the OER region. Conclusively, the $R_{ct}C_{dl}$ product becomes ideal for evaluating OER activity which is both intrinsic and active surface area normalised.

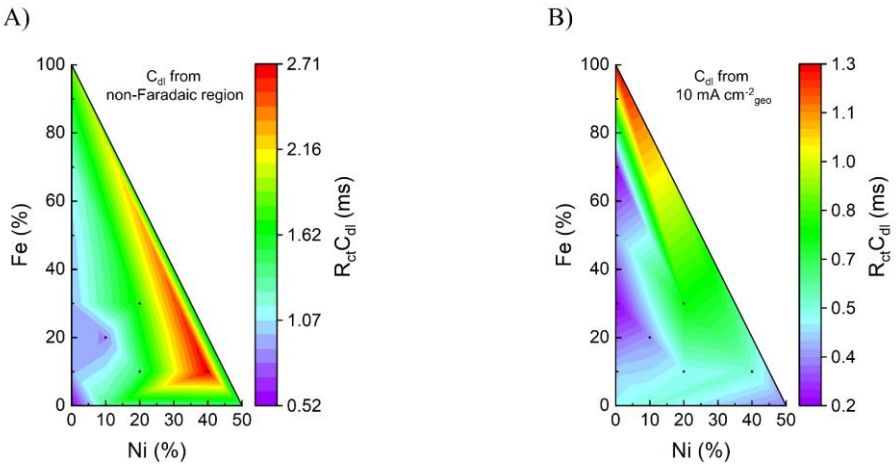

*Figure 5.21: Contour plot of the $R_{ct}C_{dl}$ product of all B-site substituted ECs. With C_{dl} from **A)**: EIS in the non-Faradaic potential region and **B)**: EIS at 10 mA cm^{-2}_{geo}.*

5.2.3 Specific Activity

In the above, we normalised the charge transfer resistance with the double layer capacitance to obtain information on intrinsic activity decoupled from electrochemically active surface area. In this subchapter, we discuss the results from normalising the OER current at 1.63 V vs. RHE (400 mV overpotential) with respect to BET surface area and double layer capacitance. All values of normalised activity descriptors can be found in Table 9.4 in Appendix.

As discussed previously, we found that the C_{dl} from EIS in the capacitive region gave the best trend with the observed R_{ct} and Tafel slopes from CA. Figure 5.22 therefore presents the specific activity (SA) of the Fe substituted ECs with respect to BET surface area (black) and the C_{dl} in the non-Faradaic region (blue) respectively. We did consider using the C_{dl} extracted from EIS at 10 mA cm^{-2}_{geo} to normalise, however the OER current is not equal for all ECs at 1.63 V vs.

RHE and it would thus not be correct to do so. We caution that BET surface area gives the total surface of the electrocatalysts and that the ECSA might be completely different. However, statistically, these are proportional to each other and good results can still be found.

The BET normalised specific activity show that the highest OER activity lies in the region with 30-50% Fe substitution, which is in satisfactory agreement with most of the previously presented results. The capacitance-normalised current on the other hand reveals the highest OER activity to be between 50-70% Fe substitutions. Yet, the high error in this region due to the variance in C_{dl}, renders this normalised curve less trustworthy. Hence, we conclude that the most trustworthy specific activity is found by normalising the current with the BET surface area.

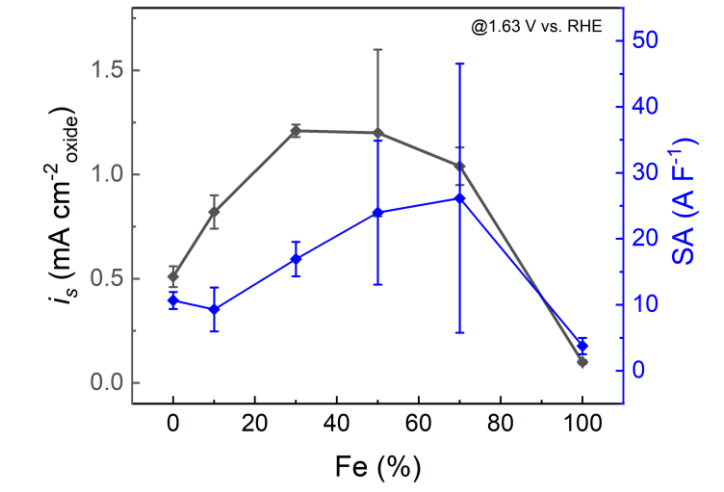

Figure 5.22: Specific activity at 1.63 V vs. RHE of the Fe substituted ECs. Current is normalised by the BET surface area (black) and the double layer capacitance (blue) from EIS in the capacitive (non-Faradaic) potential region.

The specific activities from BET and C_{dl} normalisation as a function of both Fe and Ni content are given in Figure 5.23 A and B. These figures confirm yet again that the highest OER activity is found at low Ni-content (below 20%) in BGLC587. Particularly the BGLCFN2010 sample is prominent from the BET normalised current, where it reaches a SA of 1.77 mA cm$^{-2}_{oxide}$. We can see a local increase in specific activity at this composition in Figure 5.23 B too, however not to the same extent. Other than this, both figures share the trend with the preceding findings.

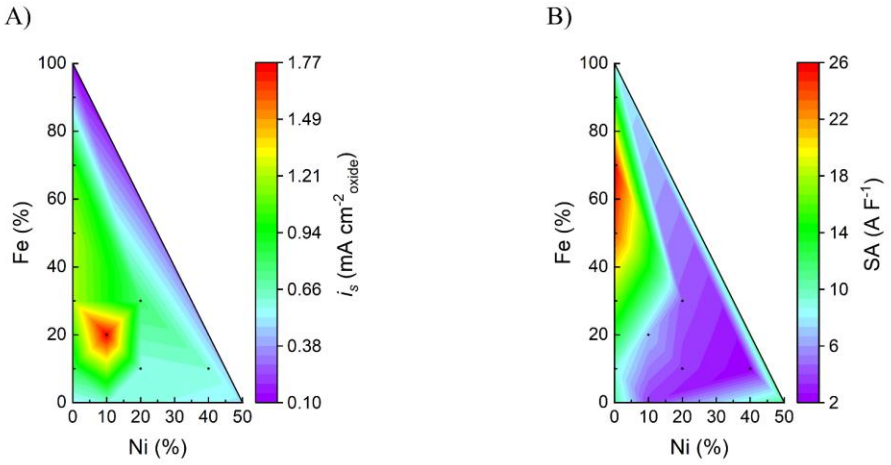

*Figure 5.23: Specific activity at 1.63 V vs. RHE of all B-site substituted ECs. Current is normalised by **A)**: the BET surface area and **B)**: the double layer capacitance from EIS in the capacitive (non-Faradaic) potential region.*

5.3 Electrochemical Stability

The stability of the most promising electrocatalysts during OER is given in Figure 5.24, where galvanostatic measurements have been done at 10 mA cm$^{-2}_{geo}$. The most important results from this type of measurements are presented in Table 5.3, which gives the durations for a 10% and 20% degradation compared to the initial values in the beginning of the OER measurement. Columns 3 and 5 also give the respective overpotentials at 10% and 20% degradation.

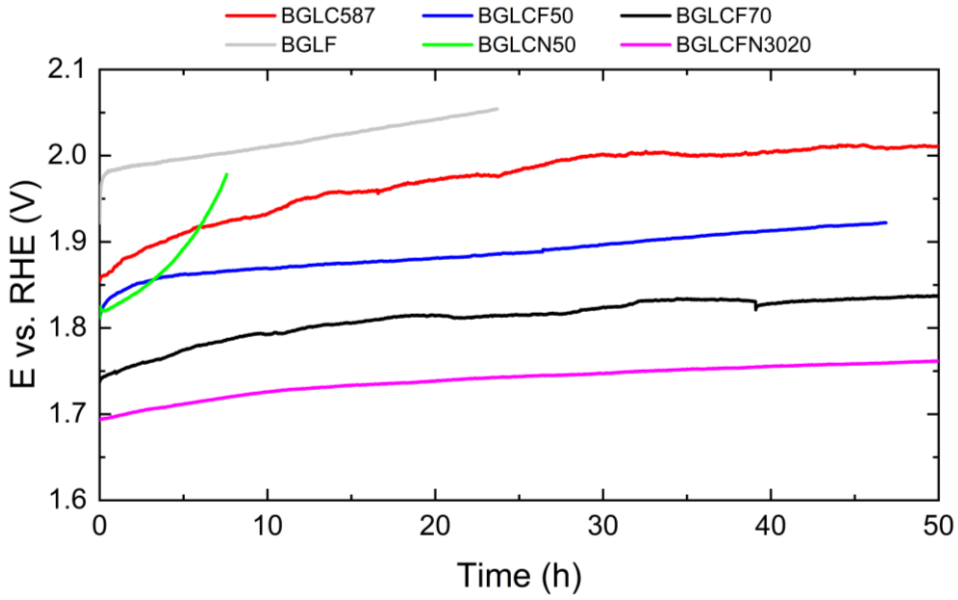

Figure 5.24: Chronopotentiometric (CV) curves of BGLC587, BGLCF50, BGLCF70, BGLF, BGLCN50 and BGLCFN3020 electrocatalysts at 10 mA cm$^{-2}_{geo}$ in O_2-saturated 1.0 M KOH. The working electrode was carbon paper with 5 mg cm^{-2} catalyst loading.

Ideally, a catalyst should have little to no degradation, but this is rare. It is therefore common to report the time it takes for an OEC to show a degradation of 10%. As can be seen from Table 5.3, BGLCFN3020 shows the best stability reaching 10% and 20% degradation rates after 20 h and 84 h respectively. In addition, both BGLCF50 and BGLCF70 show good stability, whereas the base electrocatalyst, BGLC587, reaches 20% degradation in under a third of BGLCFN3020. The EC with 100% Fe (BGLF) is initially underperforming compared to BGLC587, but at 20% degradation, they are quite similar. Lastly, BGLCN50 displays inferior stability and quickly degrades after a few hours of operation.

Compared to the stability of the ECs in Table 3.2, the degradation of even the best performing samples does not look superior. Still, it has to be taken into consideration that much of the stability measurements in literature is done using the RDE. As mentioned in Chapter 4.2.3, the use of these low surface area electrodes are unacceptable for approaching stability under realistic conditions. A second point is that much of the work shown in Table 3.2 was performed in 0.1 M KOH, which is not as harsh as the 1 M KOH used in this work. The electrolyte concentration, and hence the pH, can therefore be an important factor contributing to the higher degradation of the electrocatalysts observed. Lastly, it can be emphasised that it is not easy to compare the stability measured with CV and CA/CP methods, since CV methods measure the activity as a function of number of cycles, whereas CA/CP methods measure activity with time. The effective fatigue of the electrode is therefore not directly comparable.

Table 5.3: Data on the stability of the electrocatalysts collected from Figure 5.24. The time evolved until 10% and 20% degradation and corresponding overpotentials are given for the catalyst materials.

Electrocatalyst	10% degradation (h)	η at 10% degradation (mV)	20% degradation (h)	η at 20% degradation (mV)
BGLC587	5.7	688	24.1	750
BGLCF50	11.2	632	~50*	~690*
BGLCF70	8	559	54.7	610
BGLF	3.4	763	~26*	~832*
BGLCN50	4	641	6.3	700
BGLCFN3020	20.7	510	84.1	557

*CP measurement was cancelled close to the point of 20% degradation. Therefore, a linear fit of the last 60 minutes of data points was used to extrapolate the curve.

Since all the electrodes had the same catalyst loading and the same geometric surface area, their relative activity should be quite comparable just by looking at Figure 5.24. From this, it is evident that BGLCFN3020 exhibits the lowest overpotential, followed by BGLCF70,

BGLCF50, BGLC587 and BGLF. With the exception of BGLCFN3020, this trend is in good agreement with the activity observed from the RDE measurements and further supports the reliability of the results.

In chapter 3.1, we discussed how high activity is often related to low stability. Our results show on the other hand that the stability follows the activity in the Fe substituted ECs. This can be seen in Figure 5.25, which presents the trend of overpotential and Tafel slope vs. stability with Fe content.

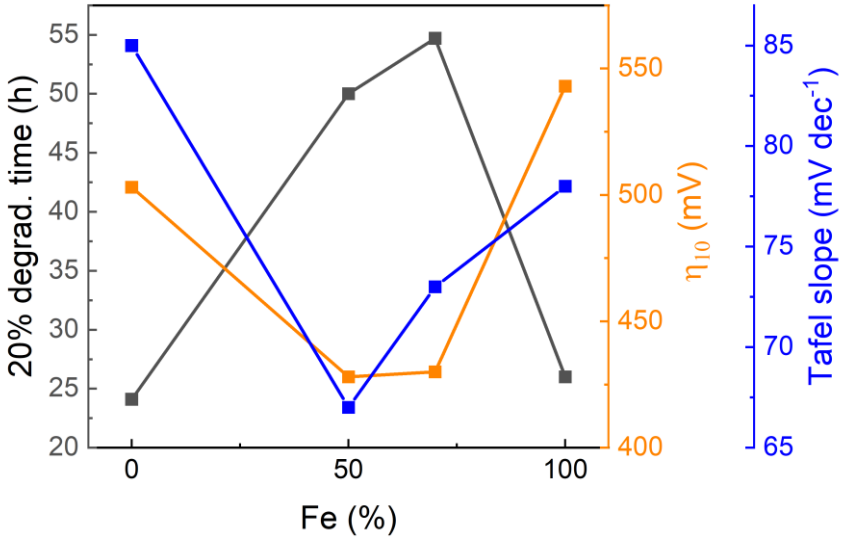

Figure 5.25: Stability vs. activity trend. The stability (black) is the time before reaching 20% degradation at 10 mA cm^{-2}_{geo}. The activity is given from the overpotentials at 10 mA cm^{-2}_{geo} and the Tafel slopes from CA.

Post Operation XRD

To further evaluate the stability of the ECs, we discuss their structural stability from post operation XRD. The results from these measurements are provided in Figure 5.26, where post operation XRD patterns are compared to their respective as-synthesised patterns. The post-mortem (PM) XRD was conducted on the C-paper electrodes from the chronopotentiometric stability measurements in Figure 5.24. Thus, green stars indicate the location of peaks originating from the C-paper support.

Phase quantification with Rietveld refinement was found to be impractical because some of the C-paper peaks were very close to those of the electrocatalysts, proving it difficult to fit correctly. Therefore, this was not done for the PM electrocatalysts. However, as can be seen from Figure 5.26, no new phases occur in the post operation diffraction patterns and it was found that all

electrocatalysts maintained the presence of their initial phases after operation. This led to the conclusion that the bulk structure of these materials are stable under operating conditions and that no irreversible phase transitions occurred.

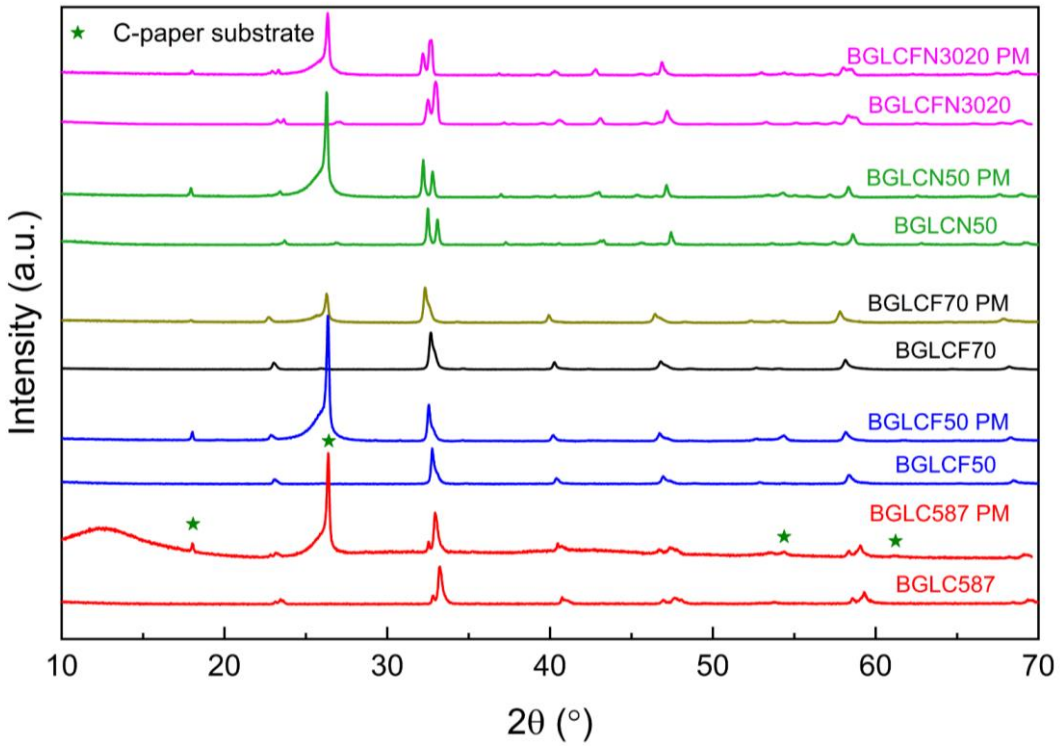

Figure 5.26: Post-mortem (PM) XRD patterns of BGLC587, BGLCF50, BGLCF70, BGLCN50 and BGLCFN3020 with respective as-synthesised powder XRD patterns.

5.4 In Situ Raman Spectroscopy

Figure 5.27 A-D show the resulting Raman spectra from BGLC587, BGLCN50, BGLCF50 and BGLCF70 during OER at 1.6V vs. RHE. We see that the peak intensities in the spectra of all the samples, except BGLCF70, vary initially with time and stabilise typically after 5 minutes. This can indicate that some of the electrocatalysts are either activating or degrading initially with some kind of reconstruction happening on the surface. Looking at the chronoamperometry curves in Figure 5.28, we observe that the biggest drop in current density occurs before 5 minutes, which is likely connected with the stabilisation seen in the Raman spectra. BGLCF70 shows the best electrochemical stability of the three materials, which is can be why it has no notable variation in peak intensities in its Raman spectra.

A theory supporting an initial activation/degradation, which was observed by Zhu et al. in BGLC587 [27], is that the active B-site elements can migrate to the surface of the electrocatalyst during OER as a result of Ba loss to the electrolyte. This can explain the development of the

Raman intensities. Since the spectra acquired from the BGLCF70 sample looks more or less constant with time, it could be an indication that this material does not undergo the same degree of A-site loss during OER.

The BGLCF70 spectra also appears less smooth with more noise than the other three. This is probably be due to its significantly higher current density, which can be observed in the CA measurements in Figure 5.28. The higher rate of oxygen evolution may, as discussed previously, interfere with the surface sensitive Raman measurement. From the CA measurements, we find that the current density increases in the order BGLC587 < BGLCN50 < BGLCF50 < BGLCF70. In fact, it looks like the noise in the Raman spectra in Figure 5.27 also increases in the same order and that this correlation holds well.

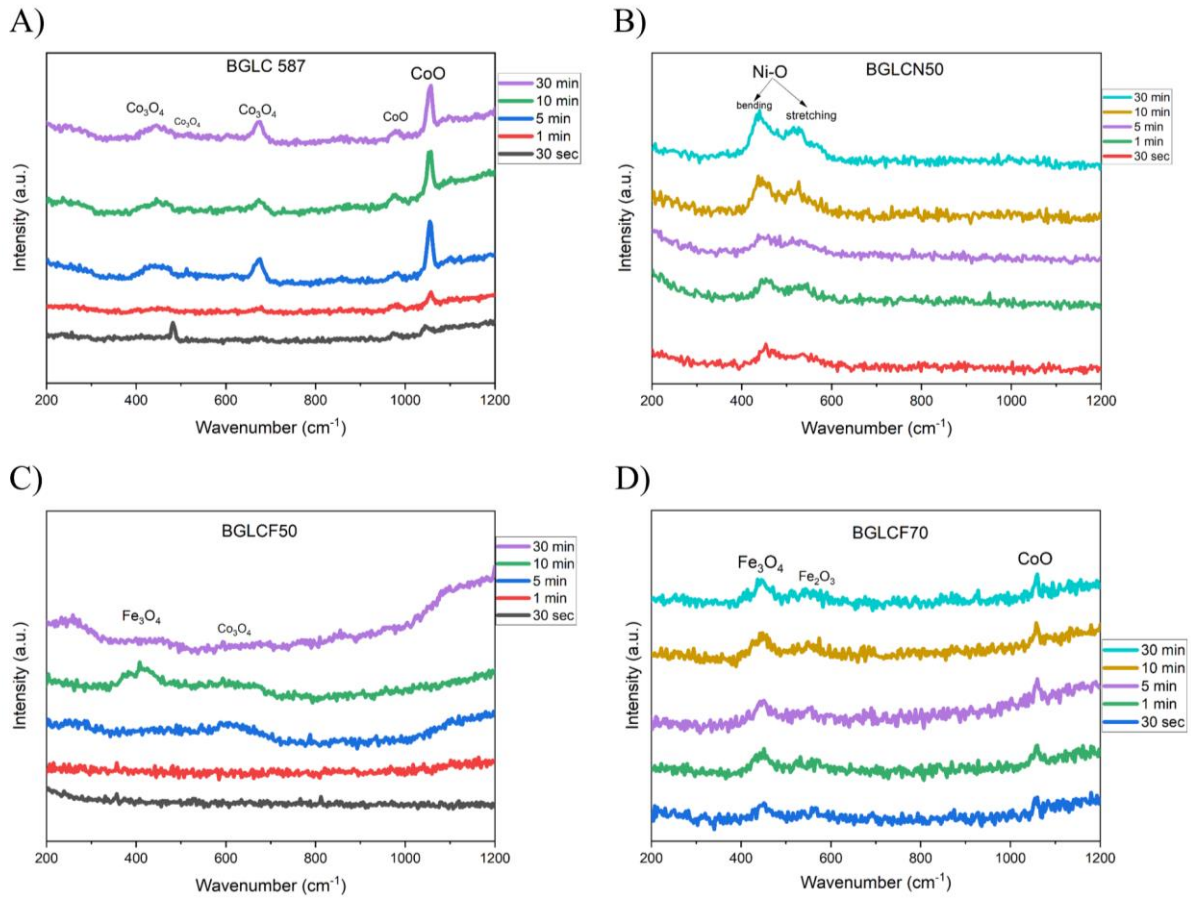

*Figure 5.27: Raman spectra collected after 30 seconds, 1, 5, 10 and 30 minutes of OER operation at 1.6V vs. RHE in 1.0 M KOH for **A)** BGLC587, **B)** BGLCN50, **C)** BGLCF50 and **D)** BGLCF70.*

The Raman shifts for BGLC587, BGLCF50 and BGLCF70 were found to correspond to oxides of Co and Fe, whereas no shifts were found that could indicate the presence of (oxy-)hydroxide. This suggests that rds in Equation (5.2) is more likely in these catalysts than that the fourth step

in the Shinagawa path (in Table 2.1) with similar Tafel slope. The observed Raman shifts indicate that both di- and tri-valent Co and Fe are present at the surface of the electrocatalysts, however no indications of tetra-valent Co or Fe were found.

The spinel structure of Co_3O_4 found in BGLC587 and BGLCF50 is interesting since it can be compared to the work by May et al. on post operation Raman spectroscopy of BSCF83 [38]. They found both amorphisation of the surface and A-site loss in BSCF82 after OER cycling, however they also saw indications of Co_3O_4 spinel structure in the surface layer from both HRTEM and Raman spectroscopy. This strengthens the hypothesis of A-site cation leaching and amorphisation, but may also help in explaining what happens at the surface.

For BGLCN50, the two Ni-O shifts were ascribed to NiO(OH) indicating the presence of Ni(III), which can be correlated with the mixed valence of Ni(II/III) in the dominating $La_3Ni_2O_7$ phase observed in BGLCN50 in Chapter 5.1.1. The detection of oxy-hydroxide in BGLCN50 and not the others, may be indicative of a different OER reaction mechanism and rate determining step (rds). Looking at the proposed reaction mechanisms of the OER in Table 2.1 one can see that only the paths where oxygen is formed through terminal peroxide groups may apply in a case with oxy-hydroxide intermediates. Comparing the Tafel slope of BGLCN50 (60 mV dec^{-1}) with these paths, it could be suggested that the reaction proceeds through the 4^{th} step in the Shinagawa path.

$$MO_2H + OH^- \rightarrow MO_2^- + H_2O \tag{5.3}$$

This would mean that oxyhydroxides are not deprotonating, but rather sticking to the surface, which is the reason why they appear in the Raman spectra. This result is of immense importance because it allows us to toss several rds's from the Tafel analysis aside and hence narrow down the possible reaction mechanisms. We therefore conclude that identification of adsorbed surface species and intermediates through in situ Raman spectroscopy is a key experiment in order to understand reaction mechanisms.

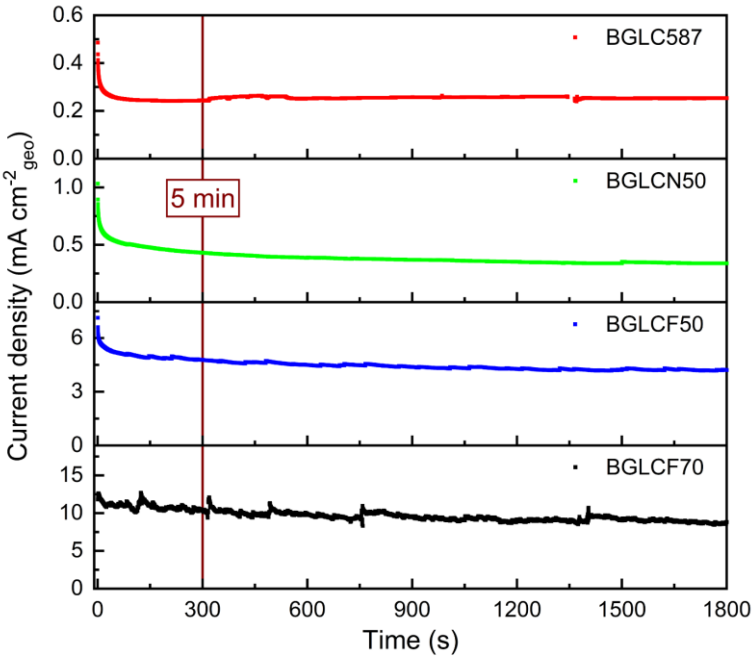

Figure 5.28: Chronoamperometry curves of BGLC587, BGLCN50, BGLCF50 and BGLCF70 during collection of Raman spectra. The vertical line indicates the position corresponding to 5 minutes of operation.

5.5 Electronic Effects of Fe Substitution

It is undeniable from the electrochemical characterisations above that Fe substitution in BGLC587 improves both the electrocatalytic activity towards the OER. However, we have limited knowledge as to how and why Fe enhances the OER performance. In this subchapter, we propose two main hypothesises for the increased activity based on results from literature regarding Fe content in oxides. We discuss the validity of these and argue that the electrochemical stability is also closely related to the activity.

5.5.1 Co 3*d* to O 2*p* Covalency

The first hypothesis is based on the work by Duan et al. in which they show that substitution with low Fe content in $LaCoO_3$ boosts the OER performance [78]. They found from DFT measurements that Fe induces the high-spin (HS) configuration of Co^{3+} as shown in Figure 5.29. This was confirmed by X-Ray near edge spectroscopy (XANES), from which they saw that the highest concentration of HS Co^{3+} was at Fe substitutions below 25%. This also correlated well with the specific activity the catalysts exhibited.

As can be seen from Figure 5.29, an increased covalency between the Co 3*d* and O 2*p* band is facilitated by the augmented overlap of these. The enhanced covalency promotes the OER by lowering the band gap and hence amplify the electronic conductivity of the material. As

discussed by Suntivich et al. [31], the OER activity can have a volcano shape dependence, with a peak activity at an e_g electron filling of unity. The e_g electron orbital filling in Fe substituted $LaCoO_3$ is naturally also affected by the escalated covalency and will effectively become closer to unity.

Our Fe substituted BGLC587's are closely related to the $LaCoO_3$ material through phase composition and B-site cation (see Chapter 5.1.1). We therefore conclude that the theoretical explanation by Duan et al. can be justified as a compatible explanation to the increased activity at low Fe content in the parent BGLC587.

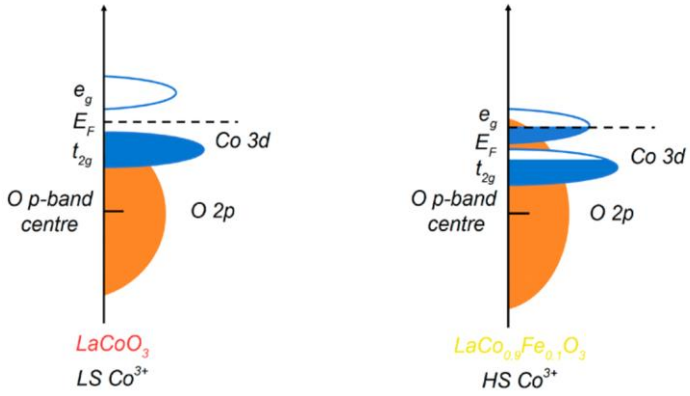

Figure 5.29: Schematic illustration of the Co 3d-O 2p overlap in LaCoO3 (left) and $LaCo_{0.9}Fe_{0.1}O_3$ (right) [78].

5.5.2 Electron hole concentration and Fe^{4+}/Co^{4+}

The second hypothesis is based on defect chemistry considerations in Fe substituted BGLC587 and the OER trend found by Nocera et al. in films of $CoFeO_x$ with varying Fe content [30]. We attempt at proving that the elevated OER activity at Fe 30-70% substitution is due to an increased concentration of electron holes, presumably localised in Fe^{4+} and/or Co^{4+}. This we base on the discovery by Nocera et al. that the OER activity, as reflected by Tafel slopes, tracks the Fe^{4+} concentration in thin films of $CoFeO_x$ [30]. Comparatively, they noticed that the highest activity was found in the 40-60% Fe alloying range as can be seen in Figure 5.30.

It must be emphasised that the $CoFeO_x$ films are a very different materials than our perovskite BGLCF-based powders and they can thus not be compared directly. However, we consider this result in the discussion because the activity trend is similar with what we find in this work. It is also essential that $CoFeO_x$ have the same active elements as Fe substituted BGLC. Another argument is that the surface of BGLC587 becomes amorphous and rich in B-site cations during

OER operation [27]. Assuming that this also happens in the Fe substituted ECs, it can provide a chemical environment similar to a $CoFeO_x$ film.

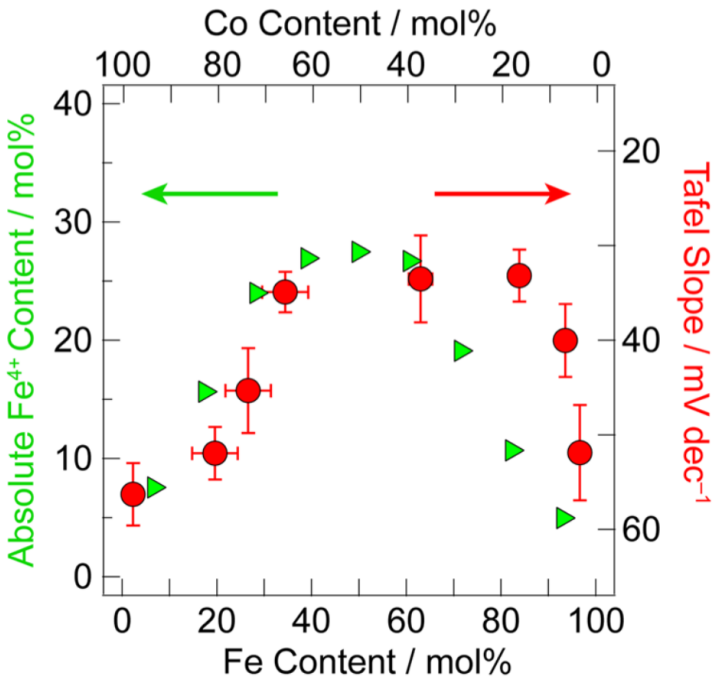

Figure 5.30: The Tafel slope and Fe^{4+} concentration in $CoFeO_x$ films as a function of Fe content [30].

Oxidation State of Fe

A key discussion by Nocera et al. is that Co^{4+} is the active OER site, while Fe^{4+} only acts as a redox cooperative centre strengthening the oxidising power of a Co:Fe site compared to a pure Co^{4+} site. Thus we investigated the oxidation state of Fe through the binding energies (BE) of its 2*p* electrons with XPS. Figure 5.31 A shows how the BE varies with Fe content in BGLCF30, BGLCF50 and BGLCF70. It can be realised from this that Fe exhibited a tri-valent oxidation state in all three ECs, with no indication of Fe^{4+} or Fe^{2+}. In comparison, the results from in situ Raman spectroscopy indicated the presence of Fe^{3+} and Co^{3+}, but also Fe^{2+} and Co^{2+}. This difference can be explained by the fact that XPS measurements are ex situ in vacuum, whereas Raman spectroscopy was done in situ during oxygen evolution and they hence provide very different conditions.

It is important to note that some presence of higher or lower valent Fe cannot be fully excluded with XPS. However, it is possible that the absence of Fe^{4+} is compensated by Co^{4+}, which we did not resolve from the XPS measurements. In addition, we have to clarify that these ex situ XPS measurements do not tell us how the oxidation state of Fe and Co behaves during OER.

Considering the anodic potentials during OER, it is imaginable that this will facilitate the formation of higher-valent Fe or Co. In fact, the $CoFeO_x$ films investigated by Nocera et al. were synthesised from a Co:Fe hydroxide film by applying an anodic potential, which supports this argument.

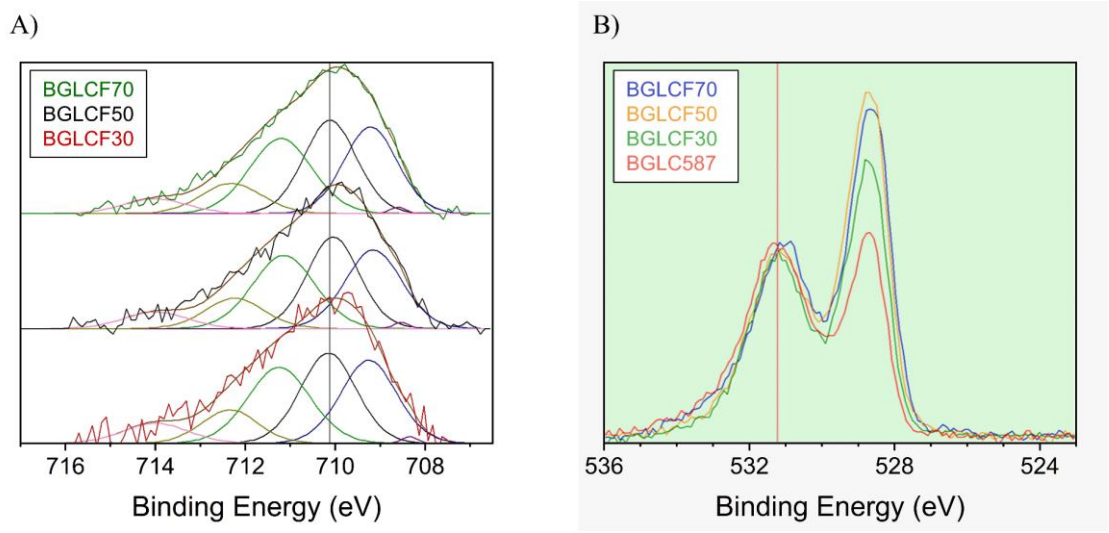

*Figure 5.31: Binding energies of **A)**: Fe 2p in BGLCF30, BGLCF50 and BGLCF70 and **B)**: O 1s in BGLC587, BGLCF30, BGLCF50 and BGLCF70.*

Oxygen Content

As mentioned in the theory chapter, acceptor doping of perovskite oxides may induce both electron holes and oxygen vacancies. In terms of OER it is beneficial to increase the electron hole concentration to facilitate oxidation of water. Since BGLC587 has a substantial oxygen deficiency, it is interesting to see how this varies with Fe content. We thus did XPS measurements on BGLC587, BGLCF30, BGLCF50 and BGLCF70.

Figure 5.31 B shows the O 1*s* BE of the ECs and we find that the intensification of the peak at 528.5 eV indicates that the oxygen content increases with increasing Fe content. The peak at 531.2 eV was attributed to perovskite lattice oxygen similar to that observed in $LaCoO_3$. The unchanged intensity of this peak coincides well with the perovskite phases found from Rietveld refinement in all compositions. We attribute the increased lattice oxygen content to the higher Fe-O bond strength compared to that of Co-O. This is in agreement with what was found by Lim et al. in Fe doped $PrBa_{0.8}Ca_{0.2}Co_2O_{6-\delta}$ (PBCO) [39].

The oxygen vacancies in BGLC587 is a result of charge compensation of the acceptor doping with Ba^{2+} on a La^{3+}/Gd^{3+}-site. Since Fe incorporation increases the oxygen content in BGLC587, it will also be closer to stoichiometric. In this situation, we will have electron holes

as the dominating defects, which explains the higher OER performance. However, it is obvious that Fe needs Co to facilitate OER, since the BGLF (100% Fe) composition is rather inferior.

5.6 Faradaic Efficiency

Measuring the Faradaic efficiency (FE) is important to assess the selectivity of the catalyst materials towards the OER in the given chemical environment. Figure 5.32 presents the results from FE measurements of six of the most promising electrocatalysts. The data used to calculate the FE were acquired after 20 minutes to let the system reach a steady state and stopped after 90 minutes where the H_2 detection range of the gas chromatograph (GC) was typically exceeded.

Figure 5.32 A and B give the FEs of the OER and HER with efficiencies ranging between 85-101% and 50-82% respectively. Notably, the FEs of the HER are very low. Since no leakage was detected from the electrolytic cell, leakages out of the micro GC during sampling was considered likely. However, with such a high deviation from the ideal case, we cannot be certain that the loss in FE is only due to leakages. It is possible that oxygen from the anode diffuse to the Pt cathode and that ORR happens. This would lower the FE of the HER. Therefore, the FE of the HER performed by the electrocatalysts are not considered very reliable with these experimental configurations.

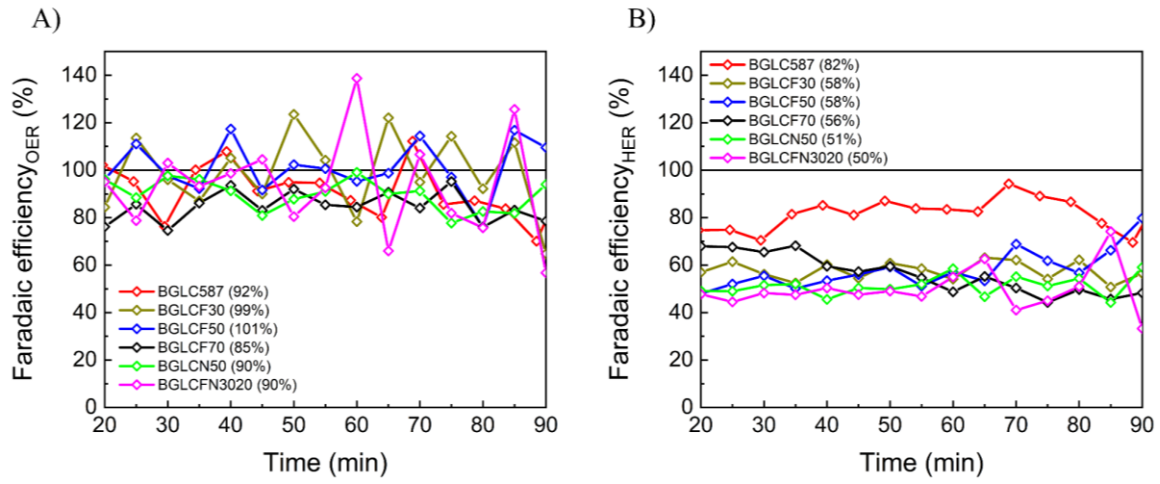

*Figure 5.32: Faradaic efficiency of **A)** the OER and **B)** the HER of the six most active electrocatalysts loaded in C-paper electrodes.*

In all measurements, an increase in N_2 was observed with time. This can be attributed to leakage of air into the GC during sampling. However, from the amount of N_2 leakage, the O_2 coming from air was found easily by the 78:21 ratio in the atmosphere. The FEs of the catalysts in Figure 5.32 A are therefore corrected for O_2 leakage into the GC. Hydrogen correction because of this leakage is on the other hand harder to correct and account for. This could be the reason why not all FEs of the HER reached 100%, although the cathode was Pt-based. In any case, the measured OER efficiencies were considered as minima and it was concluded that the real values are probably found close to 100%.

6 Future Perspectives

6.1 Applications

In order to test the applicability of the electrocatalysts in full electrolysis cells, BGLCF50 was deployed in a novel, monolithic photoelectrochemical (PEC) water splitting device in related activities in the group for Electrochemistry at UiO. A thorough explanation of a similar PEC cell design can be found in [27], but in short, the device consisted of a NiMo cathode electrodeposited on Ti foil, a high performance GaAs photovoltaic cell and an anode with BGLCF50 as prepared under this work, deposited by pulsed laser deposition (PLD) on ITO-coated glass.

The photocurrent density generated under 1 sun illumination in 1M KOH electrolyte is shown in Figure 6.1 A. It was found that the cell delivered an initial solar-to-hydrogen efficiency of 10.5%, but dropping to 5.1% in just under 4 hours. Figure 6.1 B shows LSVs of the NiMo cathode, GaAs PV and BGLCF50 anode before and after 1 sun illumination. It is clear that the degradation of the anode (red dashed line) contributes the most to the lowered STH efficiency. This shows that the high stability of BGLCF50 previously observed is not present in this PEC cell. Nonetheless, the catalyst layers deposited by PLD in these cells are only a few tens of nanometres thick, which can be an explanation as to why the degradation is so fast. Future physico-chemical characterisation is expected to reveal structural changes (amorphisation, loss of material etc.) that contributed to the poor stability under these conditions.

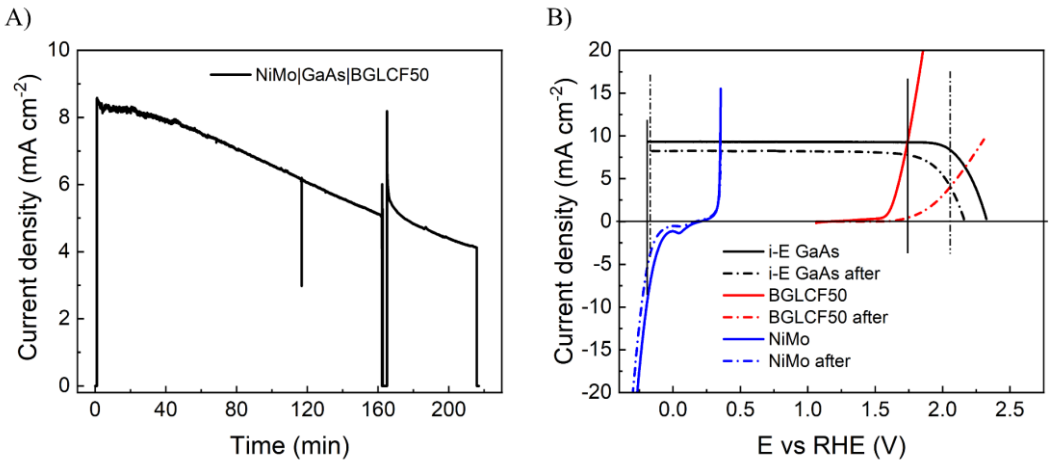

*Figure 6.1: **A)**: The photocurrent density of the NiMo|GaAs|BGLCF50 PEC cell. **B)**: LSVs of the NiMo cathode, GaAs PV and BGLCF50 anode taken before and after the chronoamperometric test in A).*

6.2 Future Investigations

This work has only touched upon the surface of the mechanisms and explanations as to why BGLC587 behaves differently during OER with A-site and B-site substitution. One of the most uncertain results are the proposed mechanisms, as Tafel analysis of the OER is not trivial. To further evaluate this, we suggested to do in situ Raman spectroscopy at different potentials to see how the type of surface species changes with potential from i.e. hydroxide to oxy-hydroxide and to oxide. A possible solution to differentiate whether the OER happens through AEM or LOM is to perform isotope measurements. By having oxygen isotopes in either the electrocatalyst lattice or the electrolyte, a gas phase analysis of the evolved O_2 gas through mass spectrometry would be able to identify if the evolved gas comes from the lattice or the electrolyte.

It will be beneficial to precisely determine the oxidation state of the B-site cations. This can be done with the powerful technique of Mössbauer spectroscopy which has a high energy resolution able to distinguish small changes in the chemical environment in materials. Another method is by evaluating the energy loss near edge structure (ELNES) from electron energy loss spectroscopy (EELS) measurements in a TEM. Ultimately, if it is possible to do these measurements (including XPS) operando, this will be key to understanding how the redox properties of the surface cations change upon polarisation.

One of the investigations that started during the work with this thesis, was the study of the electrocatalyst surface after OER operation. Since we know the surface of BGLC587 becomes amorphous, it will be important to find out whether this happens to the Fe and Ni substituted electrocatalysts too. This can for instance be done at the same intervals and current densities that we here acquired the Raman shifts. In this way, they can be correlated with each other and give enhanced insight. The amorphisation could be a result of the OER potential pushing redox active B-site cations to the surface. A hypothesis regarding this that the amorphisation may not happen is the B-site cations already are present at the surface from the start. This could then be done by for instance exsolution in reducing conditions. Moreover, the extent of the amorphisation is very important when these catalysts are applied as thin films, e.g. in the monolithic photoelectrochemical cell above.

Other simple investigations that are tempting to conduct based on our results is to investigate the increased activity and stability found with low Ni content (< 20%). This can for instance be done by taking the best performing electrocatalysts with Fe substitution and incorporate small

amounts of Ni. Another great achievement would be to find out which of the 3-4 phases in the electrocatalysts that contributes the most to the activity and thus synthesis (if possible) a single phase of this material.

7 Conclusions

To conclude, this work confirmed the hypothesis that substitution with Fe and Ni leads to increased OER activity in BGLC587. Consequently, the aim to reduce the cobalt content was also achieved. Through several electrochemical techniques, we confirmed that a 30-70% Fe content in BGLC587 led to the biggest increase in activity and stability, whereas high Ni content had the adverse effect. However, the overall best activity and stability was found with low Ni content in combination with Fe, suggesting a synergetic effect. We conclude that the enhanced activity with Fe is mainly due to the increased electron hole concentration and that Ni contributes with an increased electronic interaction between active sites. Substitution on A-site was less successful, where only the introduction of K at Ba-sited led to a lower overpotential.

We found that in situ Raman spectroscopy was crucial in order to deduce the rate determining step and decide on an OER mechanism in the Fe and Ni substituted BGLC587. Oxy-hydroxide intermediates were detected on BGLCN50 during OER and with a Tafel slope of 60 mV dec^{-1}, this indicated that the OER on Ni substituted electrocatalysts progresses through a peroxide terminated reaction path such as the Shinagawa path. Tafel slopes and results from Raman spectroscopy in Fe substituted electrocatalysts showed on the other hand no (oxy-)hydroxide formation. This indicated the presence of AEM rather than LOM. Based on the Tafel slopes approaching 60 mV dec^{-1}, the rds was assigned to a proton-exchange reaction.

The best estimation on the relative ECSAs of the electrocatalysts during OER was found through the C_{dl} from EIS at 10 mA cm^{-2}_{geo}. We found that the C_{dl} determined by CV in the non-Faradaic region to be less correct in order to describe the ECSA. This result was supported by the good correlation between the $R_{ct}C_{dl}$ product and the observed overpotentials, Tafel slopes and charge transfer resistances, which were not seen when using C_{dl} estimated in the non-Faradaic region. In conclusion, these results serve as a validation of the $R_{ct}C_{dl}$ as a descriptor on the true intrinsic surface area-normalised activity of electrocatalysts.

As a final remark, we successfully synthesised promising electrocatalysts with performances comparable with several reported materials in literature. With further investigations, we believe that these perovskite materials has the potential to be developed into high performance state-of-the-art electrocatalysts for the OER, possessing both high catalytic activity and stability.

8 References

1. IEA. *Global Energy Review: CO2 Emissions in 2020*. 2021 [cited 2021 October 5th]; Available from: https://www.iea.org/data-and-statistics/charts/global-energy-related-co2-emissions-1990-2021.
2. Company, M. *Global Energy Perspective 2021*. Energy Insights by McKinsey & Company 2021 [cited 2021 October 5th]; Available from: https://www.mckinsey.com/industries/oil-and-gas/our-insights/global-energy-perspective-2021.
3. IEA. *Key World Energy Statistics 2021*. 2021 [cited 2021 October 7th]; Available from: https://www.iea.org/reports/key-world-energy-statistics-2021.
4. IEA. *Renewables and low-carbon share in power generation in the Net Zero Scenario, 2000-2030*. 2021 [cited 2022 March 7th]; Available from: https://www.iea.org/data-and-statistics/charts/renewables-and-low-carbon-share-in-power-generation-in-the-net-zero-scenario-2000-2030.
5. IEA. *Renewable Power*. 2021 [cited 2022 March 7th]; Available from: https://www.iea.org/reports/renewable-power.
6. Ehret, O. and K. Bonhoff, *Hydrogen as a fuel and energy storage: Success factors for the German Energiewende.* International Journal of Hydrogen Energy, 2015. **40**(15): p. 5526-5533.
7. IEA. *Net Zero by 2050*. 2021 [cited 2022 March 7th]; Available from: https://www.iea.org/reports/net-zero-by-2050.
8. Barber, J., *Hydrogen derived from water as a sustainable solar fuel: learning from biology.* Sustainable Energy & Fuels, 2018. **2**(5): p. 927-935.
9. Edwards, P.P., V. Kuznetsov, and W.I. David, *Hydrogen energy.* Philosophical Transactions of the Royal Society A: Mathematical, Physical and Engineering Sciences, 2007. **365**(1853): p. 1043-1056.
10. Detz, R., J. Reek, and B. Van Der Zwaan, *The future of solar fuels: when could they become competitive?* Energy & Environmental Science, 2018. **11**(7): p. 1653-1669.
11. Detollenaere, A., et al., *Snapshot of Global PV Markets 2020 PVPS Task 1 Strategic PV Analysis and Outreach*. 2020.
12. Albrecht, U., et al., *Study on hydrogen from renewable resources in the EU - Final Report* 2021, Fuel Cells and Hydrogen Joint Undertaking (FCH JU).
13. Suen, N.-T., et al., *Electrocatalysis for the oxygen evolution reaction: recent development and future perspectives.* Chemical Society Reviews, 2017. **46**(2): p. 337-365.
14. Anantharaj, S., et al., *Recent trends and perspectives in electrochemical water splitting with an emphasis on sulfide, selenide, and phosphide catalysts of Fe, Co, and Ni: a review.* Acs Catalysis, 2016. **6**(12): p. 8069-8097.
15. McCrory, C.C., et al., *Benchmarking hydrogen evolving reaction and oxygen evolving reaction electrocatalysts for solar water splitting devices.* Journal of the American Chemical Society, 2015. **137**(13): p. 4347-4357.
16. Lyu, F., et al., *Noble-metal-free electrocatalysts for oxygen evolution.* Small, 2019. **15**(1): p. 1804201.
17. Osgood, H., et al., *Transition metal (Fe, Co, Ni, and Mn) oxides for oxygen reduction and evolution bifunctional catalysts in alkaline media.* Nano Today, 2016. **11**(5): p. 601-625.

18. Deng, X. and H. Tüysüz, *Cobalt-oxide-based materials as water oxidation catalyst: recent progress and challenges.* AcS catalysis, 2014. **4**(10): p. 3701-3714.
19. Zhu, Y., et al., *Self-Assembled Ruddlesden–Popper/Perovskite Hybrid with Lattice-Oxygen Activation as a Superior Oxygen Evolution Electrocatalyst.* Small, 2020. **16**(20): p. 2001204.
20. Zhu, Y., et al., *Chlorine-anion doping induced multi-factor optimization in perovskties for boosting intrinsic oxygen evolution.* Journal of Energy Chemistry, 2021. **52**: p. 115-120.
21. Xia, B., et al., *Optimized Conductivity and Spin States in N-Doped LaCoO3 for Oxygen Electrocatalysis.* ACS Applied Materials & Interfaces, 2021. **13**(2): p. 2447-2454.
22. Wang, J., et al., *Redirecting dynamic surface restructuring of a layered transition metal oxide catalyst for superior water oxidation.* Nature Catalysis, 2021. **4**(3): p. 212-222.
23. Hwang, J., et al., *Perovskites in catalysis and electrocatalysis.* Science, 2017. **358**(6364): p. 751-756.
24. Nitopi, S., et al., *Progress and perspectives of electrochemical CO2 reduction on copper in aqueous electrolyte.* Chemical reviews, 2019. **119**(12): p. 7610-7672.
25. Vøllestad, E., et al., *Mixed proton and electron conducting double perovskite anodes for stable and efficient tubular proton ceramic electrolysers.* Nature materials, 2019. **18**(7): p. 752.
26. Andersen, H., et al., *A highly efficient electrocatalyst based on double perovskite cobaltites with immense intrinsic catalytic activity for water oxidation.* Chemical Communications, 2020. **56**(7): p. 1030-1033.
27. Zhu, J., et al., *Double Perovskite Cobaltites Integrated in a Monolithic and Noble Metal-Free Photoelectrochemical Device for Efficient Water Splitting.* ACS Applied Materials & Interfaces, 2021. **13**(17): p. 20313-20325.
28. Han, L., S. Dong, and E. Wang, *Transition-metal (Co, Ni, and Fe)-based electrocatalysts for the water oxidation reaction.* Advanced materials, 2016. **28**(42): p. 9266-9291.
29. Subbaraman, R., et al., *Trends in activity for the water electrolyser reactions on 3d M (Ni, Co, Fe, Mn) hydr (oxy) oxide catalysts.* Nature materials, 2012. **11**(6): p. 550-557.
30. Li, N., et al., *Detection of high-valent iron species in alloyed oxidic cobaltates for catalysing the oxygen evolution reaction.* Nature Communications, 2021. **12**(1): p. 1-6.
31. Suntivich, J., et al., *A perovskite oxide optimized for oxygen evolution catalysis from molecular orbital principles.* Science, 2011. **334**(6061): p. 1383-1385.
32. He, D., et al., *Enhanced durability and activity of the perovskite electrocatalyst Pr 0.5 Ba 0.5 CoO 3− δ by Ca doping for the oxygen evolution reaction at room temperature.* Chemical Communications, 2017. **53**(37): p. 5132-5135.
33. Anantharaj, S., et al., *Precision and correctness in the evaluation of electrocatalytic water splitting: revisiting activity parameters with a critical assessment.* Energy & Environmental Science, 2018. **11**(4): p. 744-771.
34. Marshall, A.T. and L. Vaisson-Béthune, *Avoid the quasi-equilibrium assumption when evaluating the electrocatalytic oxygen evolution reaction mechanism by Tafel slope analysis.* Electrochemistry Communications, 2015. **61**: p. 23-26.
35. Rong, X., J. Parolin, and A.M. Kolpak, *A fundamental relationship between reaction mechanism and stability in metal oxide catalysts for oxygen evolution.* Acs Catalysis, 2016. **6**(2): p. 1153-1158.
36. Yoo, J.S., et al., *Role of lattice oxygen participation in understanding trends in the oxygen evolution reaction on perovskites.* ACS Catalysis, 2018. **8**(5): p. 4628-4636.
37. Mefford, J.T., et al., *Water electrolysis on La1− xSrxCoO3− δ perovskite electrocatalysts.* Nature communications, 2016. **7**(1): p. 1-11.

38. May, K.J., et al., *Influence of oxygen evolution during water oxidation on the surface of perovskite oxide catalysts.* The journal of physical chemistry letters, 2012. **3**(22): p. 3264-3270.
39. Lim, C., et al., *Investigation of the Fe doping effect on the B-site of the layered perovskite PrBa0. 8Ca0. 2Co2O5+ δ for a promising cathode material of the intermediate-temperature solid oxide fuel cells.* International Journal of Hydrogen Energy, 2019. **44**(2): p. 1088-1095.
40. Bredar, A.R., et al., *Electrochemical impedance spectroscopy of metal oxide electrodes for energy applications.* ACS Applied Energy Materials, 2020. **3**(1): p. 66-98.
41. Papaderakis, A., et al., *Electrochemical impedance studies of IrO2 catalysts for oxygen evolution.* Journal of Electroanalytical Chemistry, 2015. **757**: p. 216-224.
42. Trasatti, S., *Electrocatalysis in the anodic evolution of oxygen and chlorine.* Electrochimica Acta, 1984. **29**(11): p. 1503-1512.
43. Ghosh, S. and R.N. Basu, *Multifunctional nanostructured electrocatalysts for energy conversion and storage: current status and perspectives.* Nanoscale, 2018. **10**(24): p. 11241-11280.
44. Li, S., et al., *Nanostructured Co-based bifunctional electrocatalysts for energy conversion and storage: current status and perspectives.* Journal of Materials Chemistry A, 2019. **7**(32): p. 18674-18707.
45. Zeng, F., et al., *Stability and deactivation of OER electrocatalysts: A review*. Journal of Energy Chemistry, 2022.
46. Danilovic, N., et al., *Activity–stability trends for the oxygen evolution reaction on monometallic oxides in acidic environments.* The journal of physical chemistry letters, 2014. **5**(14): p. 2474-2478.
47. Cherevko, S., et al., *Dissolution of noble metals during oxygen evolution in acidic media.* ChemCatChem, 2014. **6**(8): p. 2219-2223.
48. Roger, I., M.A. Shipman, and M.D. Symes, *Earth-abundant catalysts for electrochemical and photoelectrochemical water splitting.* Nature Reviews Chemistry, 2017. **1**(1): p. 1-13.
49. Sun, X., et al., *Earth-abundant electrocatalysts in proton exchange membrane electrolyzers.* Catalysts, 2018. **8**(12): p. 657.
50. Zhu, Y., et al., *A high-performance electrocatalyst for oxygen evolution reaction: LiCo0. 8Fe0. 2O2.* Advanced Materials, 2015. **27**(44): p. 7150-7155.
51. Su, C., et al., *SrCo0. 9Ti0. 1O3− δ as a new electrocatalyst for the oxygen evolution reaction in alkaline electrolyte with stable performance.* ACS applied materials & interfaces, 2015. **7**(32): p. 17663-17670.
52. Zhang, J., et al., *Interface engineering of MoS2/Ni3S2 heterostructures for highly enhanced electrochemical overall-water-splitting activity.* Angewandte Chemie, 2016. **128**(23): p. 6814-6819.
53. Qiu, T., et al., *Highly exposed ruthenium-based electrocatalysts from bimetallic metal-organic frameworks for overall water splitting.* Nano Energy, 2019. **58**: p. 1-10.
54. Bhowmik, T., M.K. Kundu, and S. Barman, *Growth of one-dimensional RuO2 nanowires on g-carbon nitride: an active and stable bifunctional electrocatalyst for hydrogen and oxygen evolution reactions at all pH values.* ACS applied materials & interfaces, 2016. **8**(42): p. 28678-28688.
55. Kötz, R., H. Lewerenz, and S. Stucki, *XPS studies of oxygen evolution on Ru and RuO2 anodes.* Journal of The Electrochemical Society, 1983. **130**(4): p. 825.
56. Kötz, R., H. Neff, and S. Stucki, *Anodic Iridium Oxide Films: XPS-Studies of Oxidation State Changes and.* Journal of The Electrochemical Society, 1984. **131**(1): p. 72.

57. Cherevko, S., et al., *Oxygen and hydrogen evolution reactions on Ru, RuO2, Ir, and IrO2 thin film electrodes in acidic and alkaline electrolytes: A comparative study on activity and stability.* Catalysis Today, 2016. **262**: p. 170-180.
58. Lyons, M.E. and S. Floquet, *Mechanism of oxygen reactions at porous oxide electrodes. Part 2—Oxygen evolution at RuO2, IrO2 and IrxRu1− xO2 electrodes in aqueous acid and alkaline solution.* Physical Chemistry Chemical Physics, 2011. **13**(12): p. 5314-5335.
59. Kötz, R. and S. Stucki, *Stabilization of RuO2 by IrO2 for anodic oxygen evolution in acid media.* Electrochimica acta, 1986. **31**(10): p. 1311-1316.
60. Jung, J.I., et al., *Fabrication of Ba0. 5Sr0. 5Co0. 8Fe0. 2O3–δ catalysts with enhanced electrochemical performance by removing an inherent heterogeneous surface film layer.* Advanced Materials, 2015. **27**(2): p. 266-271.
61. Zhu, Y., et al., *Boosting oxygen evolution reaction by creating both metal Ion and lattice-oxygen active sites in a complex oxide.* Advanced Materials, 2020. **32**(1): p. 1905025.
62. Yagi, S., et al., *Covalency-reinforced oxygen evolution reaction catalyst.* Nature communications, 2015. **6**(1): p. 1-6.
63. Xie, R., et al., *Pr-Doped LaCoO3 toward Stable and Efficient Oxygen Evolution Reaction.* ACS Applied Energy Materials, 2021. **4**(9): p. 9057-9065.
64. Zhu, Y., et al., *Enhancing electrocatalytic activity of perovskite oxides by tuning cation deficiency for oxygen reduction and evolution reactions.* Chemistry of Materials, 2016. **28**(6): p. 1691-1697.
65. She, S., et al., *Realizing High and Stable Electrocatalytic Oxygen Evolution for Iron-Based Perovskites by Co-Doping-Induced Structural and Electronic Modulation.* Advanced Functional Materials, 2021: p. 2111091.
66. Strandbakke, R., *Oxygen electrodes for ceramic fuel cells with proton and oxide ion conducting electrolytes.* 2014.
67. Strandbakke, R., et al., *Gd-and Pr-based double perovskite cobaltites as oxygen electrodes for proton ceramic fuel cells and electrolyser cells.* Solid State Ionics, 2015. **278**: p. 120-132.
68. Vøllestad, E., et al., *Relating defect chemistry and electronic transport in the double perovskite Ba 1− x Gd 0.8 La 0.2+ x Co 2 O 6− δ (BGLC).* Journal of Materials Chemistry A, 2017. **5**(30): p. 15743-15751.
69. Strandbakke, R., et al., *Ba0. 5Gd0. 8La0. 7Co2O6-δ infiltrated in porous BaZr0. 7Ce0. 2Y0. 1O3 backbones as electrode material for proton ceramic electrolytes.* Journal of The Electrochemical Society, 2017. **164**(4): p. F196.
70. Vøllestad, E., et al., *Mixed proton and electron conducting double perovskite anodes for stable and efficient tubular proton ceramic electrolysers.* Nature materials, 2019. **18**(7): p. 752-759.
71. NorECs. *ProboStat, overview*. [cited 2022 March 28th]; Available from: https://norecs.com/index.php?page=Overview.
72. Wei, C., et al., *Recommended practices and benchmark activity for hydrogen and oxygen electrocatalysis in water splitting and fuel cells.* Advanced Materials, 2019. **31**(31): p. 1806296.
73. Mayrhofer, K., et al., *An electrochemical cell configuration incorporating an ion conducting membrane separator between reference and working electrode.* International Journal of Electrochemical Science, 2009. **4**(1): p. 1-8.
74. Guan, D., et al., *Searching general sufficient-and-necessary conditions for ultrafast hydrogen-evolving electrocatalysis.* Advanced Functional Materials, 2019. **29**(20): p. 1900704.

75. Faid, A.Y., et al., *NiCu mixed metal oxide catalyst for alkaline hydrogen evolution in anion exchange membrane water electrolysis.* Electrochimica Acta, 2021. **371**: p. 137837.
76. Joya, K.S. and X. Sala, *In situ Raman and surface-enhanced Raman spectroscopy on working electrodes: spectroelectrochemical characterization of water oxidation electrocatalysts.* Physical Chemistry Chemical Physics, 2015. **17**(33): p. 21094-21103.
77. Niu, S., et al., *How to reliably report the overpotential of an electrocatalyst.* ACS Energy Letters, 2020. **5**(4): p. 1083-1087.
78. Duan, Y., et al., *Tailoring the Co 3d-O 2p covalency in LaCoO3 by Fe substitution to promote oxygen evolution reaction.* Chemistry of Materials, 2017. **29**(24): p. 10534-10541.
79. An, S.R., et al., *Fe-doped LaCoO3 perovskite catalyst for NO oxidation in the post-treatment of marine diesel engine's exhaust emissions.* Korean Journal of Chemical Engineering, 2018. **35**(9): p. 1807-1814.
80. Wachowski, S.L., et al., *Structure and water uptake in BaLnCo2O6− δ (Ln= La, Pr, Nd, Sm, Gd, Tb and Dy).* Acta Materialia, 2020. **199**: p. 297-310.
81. Taguchi, H., et al., *Crystal structure and methane oxidation on perovskite-type (La1− x Nd x) CoO3 synthesized using citric acid.* Journal of materials science, 2009. **44**(21): p. 5732-5736.
82. Ling, C.D., et al., *Neutron diffraction study of La3Ni2O7: Structural relationships among n= 1, 2, and 3 phases Lan+ 1NinO3n+ 1.* Journal of Solid State Chemistry, 2000. **152**(2): p. 517-525.
83. Huang, K., H.Y. Lee, and J.B. Goodenough, *Sr-and Ni-doped LaCoO3 and LaFeO3 perovskites: new cathode materials for solid-oxide fuel cells.* Journal of the Electrochemical Society, 1998. **145**(9): p. 3220.
84. Sasaki, S., K. Fujino, and Y. Takéuchi, *X-ray determination of electron-density distributions in oxides, MgO, MnO, CoO, and NiO, and atomic scattering factors of their constituent atoms.* Proceedings of the Japan Academy, Series B, 1979. **55**(2): p. 43-48.
85. Wang, M., et al., *Influence of Fe substitution into LaCoO3 electrocatalysts on oxygen-reduction activity.* ACS applied materials & interfaces, 2019. **11**(6): p. 5682-5686.
86. Shinagawa, T., A.T. Garcia-Esparza, and K. Takanabe, *Insight on Tafel slopes from a microkinetic analysis of aqueous electrocatalysis for energy conversion.* Scientific reports, 2015. **5**(1): p. 1-21.
87. Li, G., et al., *New insights into evaluating catalyst activity and stability for oxygen evolution reactions in alkaline media.* Sustainable Energy & Fuels, 2018. **2**(1): p. 237-251.
88. Da Silva, L., L. De Faria, and J. Boodts, *Determination of the morphology factor of oxide layers.* Electrochimica Acta, 2001. **47**(3): p. 395-403.
89. Li, G.-F., D. Yang, and P.-Y. Abel Chuang, *Defining nafion ionomer roles for enhancing alkaline oxygen evolution electrocatalysis.* ACS Catalysis, 2018. **8**(12): p. 11688-11698.

9 Appendix

9.1 Chemicals and Materials Used

Table 9.1: Chemicals and materials used in this work.

Chemical/Material	**Feature**	**Manufacturer**
Ammonia	28%	AnalaR NORMAPUR®
Barium(II)carbonate	99.8%	Alfa Aesar
Calcium(II)carbonate	99.8%	Alfa Aesar
Toray Carbon paper	PEM grade	Alfa Aesar
Citric acid monohydrate	≥ 99.0%	Sigma-Aldrich
Co(II)chloride hexahydrate	98%	Sigma-Aldrich
Co(II)nitrate hexahydrate	≥ 98%	Sigma-Aldrich
Cs(I)nitrate	99.99%	Sigma-Aldrich
Ethanol absolute		
Fe(III)nitrate nonahydrate	≥ 98%	Sigma-Aldrich
Gd(III)nitrate hexahydrate	99.9%	Sigma-Aldrich
K(I)nitrate	99.99%	Sigma-Aldrich
La(III)nitrate hexahydrate	99.99%	Sigma-Aldrich
Nafion®	5 wt.%	Sigma-Aldrich
Ni(II)nitrate hexahydrate	98%	Alfa Aesar
Potassium hydroxide	85% and 90%	Sigma-Aldrich

9.2 PXRD of A-site Substituted Electrocatalysts

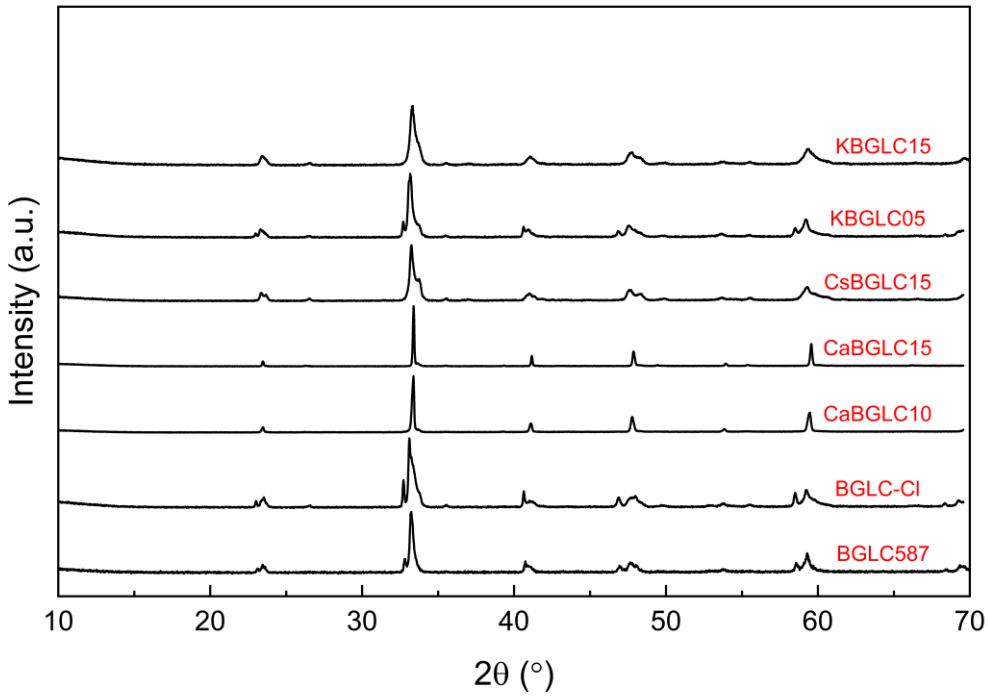

Figure 9.1: PXRD patterns of the as-synthesised Cl-, Ca-, Cs- and K-substituted BGLCs..

9.3 Phase Composition and Unit Cell Volume of Fe and Ni Substituted BGLC587

Table 9.2: Phase composition and unit cell volume of B-site substituted BGLC587 electrocatalysts. Values from post operation PXRD is indicated by (PM) after catalyst name. The unit cell volume of the $LaCoO_3$ ($R\bar{3}c$) phases correspond to unit cells with rhombohedral axes. A unit cell with double b- and c-axis (a2b2c) was used for the BGC phase, whereas a single unit cell was used for the GDC and LF phases. The NiO_x phase was refined using a 2x2x2 supercell, but the given volume is normalized with respect to cells.

Electrocatalyst	**$LaCoO_3$ ($R\bar{3}c$)**		**$BaGdCo_2O_{6-\delta}$ (Pmmm)**		**$Gd_{0.8}La_{0.2}CoO_3$ (Pnma)**		**$LaFeO_3$ (Pbnm)**		**$La_3Ni_2O_7$ (Amam)**		**NiO_x ($Fm\bar{3}m$)**	
Fe	**Wt.%**	**V_{cell} (Å^3)**	**Wt.%**	**V_{cell} (Å^3)**	**Wt.%**	**V_{cell} (Å^3)**	**Wt.%**	**V_{cell} (Å^3)**	**Wt.%**	**V_{cell} (Å^3)**	**Wt.%**	**V_{cell} (Å^3)**
BGLC587	66	112.4	22	229.9	12	224.5	-	-	-	-	-	-
BGLCF10	65	113.2	13	229.8	22	224.7	-	-	-	-	-	-
BGLCF30	39	115.3	34	229.6	15	223.8	12	227.9	-	-	-	-
BGLCF50	37	117.1	29	232.9	18	227.1	16	230.1	-	-	-	-
BGLCF70	17	118.3	46	236.7	20	230.8	17	232.5	-	-	-	-
BGLF	-	-	42	244	40	236.9	18	238.2	-	-	-	-
Ni	**Wt.%**	**V_{cell} (Å^3)**	**Wt.%**	**V_{cell} (Å^3)**	**Wt.%**	**V_{cell} (Å^3)**	**Wt.%**	**V_{cell} (Å^3)**	**Wt.%**	**V_{cell} (Å^3)**	**Wt.%**	**V_{cell} (Å^3)**
BGLCN10	44	112.4	32	229.6	-	-	-	-	20	581.6	4	75.5
BGLCN50	-	-	15	230.8	-	-	-	-	72	588.8	13	73.6
Mixed Fe/Ni	**Wt.%**	**V_{cell} (Å^3)**	**Wt.%**	**V_{cell} (Å^3)**	**Wt.%**	**V_{cell} (Å^3)**	**Wt.%**	**V_{cell} (Å^3)**	**Wt.%**	**V_{cell} (Å^3)**	**Wt.%**	**V_{cell} (Å^3)**
BGLCFN1020	26	114.3	25	231.2	-	-	-	-	40	588	9	75.1
BGLCFN1040	4	116.8	18	230.6	-	-	-	-	66	589.6	12	73.8
BGLCFN2010	56	113.8	24	230.9	16	224.4	-	-	-	-	4	74.5
BGLCFN3020	27	115.6	18	233.9	-	-	-	-	45	597.2	10	74.9

9.4 EDS Spectra

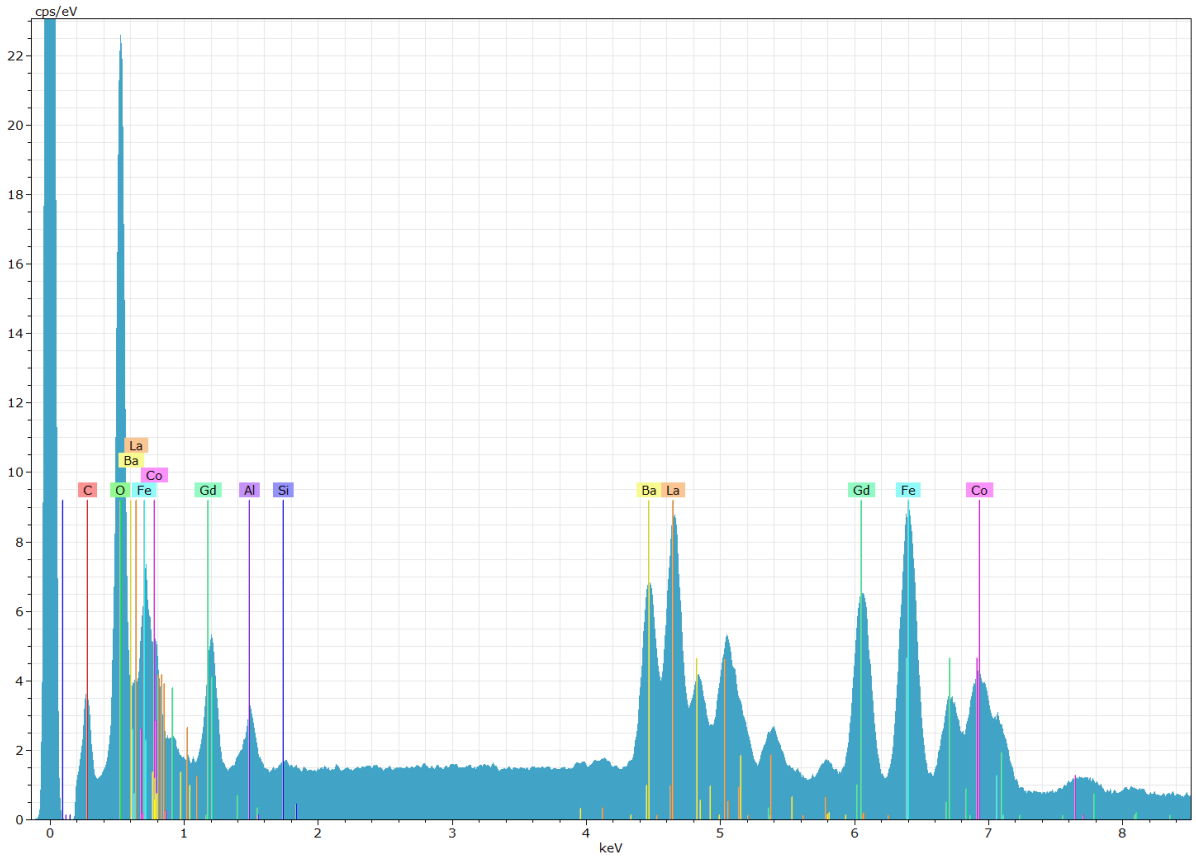

Figure 9.2: Representative EDS spectra of BGLCF70 measured in a Hitachi SU8200 SEM using a Bruker XFlash 6-10 detector. For the other samples investigated with EDS, the spectra are not given since they did not show any sign of elemental impurities.

9.5 Un-normalised OER Activity Benchmarks

Table 9.3: Collection of un-normalised OER activity benchmarks of all the synthesised electrocatalysts. ***From left****: Tafel slopes from LSVs and CP measurements with respective exchange current densities, overpotentials at 0.3 mA cm^{-2}_{geo} (onset) and 10 mA cm^{-2}_{geo} and charge transfer resistance at 10 mA cm^{-2}_{geo}. Values above the horizontal line are mean values from three independent measurements, the rest is only from one measurement.*

Electrocatalyst	b_{LSV} (mV dec^{-1})	b_{CP} (mV dec^{-1})	$i_{0,LSV}$ (mA cm^{-2})	$i_{0,CP}$ (mA cm^{-2})	$\eta_{0.3}$ (mV)	η_{10} (mV)	R_{ct} (Ω)
BGLC587	85	71	2.1E-5	3.1E-6	353	503	26
BGLCF10	76	69	1.1E-5	2.6E-6	339	481	24
BGLCF30	71	64	1E-5	2.7E-6	319	439	21
BGLCF50	67	67	8E-6	6.9E-6	313	428	23
BGLCF70	68	73	1.2E-5	1.3E-5	305	430	28
BGLCFN1020	75	66	7E-6	2E-6	352	509	28
BGLCFN1040	74	71	5E-6	5E-6	354	516	31
BGLCFN2010	73	63	6.84E-6	2E-6	327	451	19
BGLCFN3020	72	70	5.1E-6	4E-6	345	504	30
BGLCN10	79	67	1.2E-5	1.6E-6	363	504	21
BGLCN50	74	60	7E-6	5E-7	347	495	26
BGLF	88	78	2.8E-5	7.7E-6	355	543	52
BGLC-NH3	64	54	3E-6	1.3E-7	332	429	34
CaBGLC10	94	75	3.85E-5	3.69E-6	366	542	30
CsBGLC15	80	64	1.07E-5	5.21E-7	353	505	36
KBGLC05	89	69	2.65E-5	1.45E-6	360	543	25
KBGLC15	80	67	1.36E-5	1.41E-6	344	486	13

9.6 Normalised OER Activity Benchmarks

Table 9.4: Collection of normalised OER activity benchmarks of all the synthesised electrocatalysts. ***From left****: Mass activity at η=0.4V, specific activity normalised with respect to BET and double layer capacitance (from EIS in non-Faradaic region) at η=0.4V and the intrinsic catalytic activity, $R_{ct}C_{dl}$, calculated with C_{dl} at 10 mA cm^{-2}_{geo} and in the non-Faradaic (capacitive) potential region respectively. Values above the horizontal line are mean values from three independent measurements, the rest is only from one measurement.*

Electrocatalyst	Mass activity ($A\ g^{-1}$)	i_s ($mA\ cm^{-2}_{BET}$)	i_s ($A\ F^{-1}$)	$R_{ct}C_{dl}$ (ms) from OER	$R_{ct}C_{dl}$ (ms) from non-Faradaic region
BGLC587	4	0.51	148	0.46	0.52
BGLCF10	6.7	0.82	309	0.42	0.95
BGLCF30	14.2	1.21	826	0.20	0.96
BGLCF50	19	1.2	831	0.39	1.02
BGLCF70	19.8	1.04	955	0.20	1.16
BGLCFN1020	5	0.57	314	0.48	1.44
BGLCFN1040	4.4	0.61	256	0.45	2.71
BGLCFN2010	11	1.77	561	0.36	0.87
BGLCFN3020	5.6	0.77	375	0.73	1.75
BGLCN10	3.3	0.61	185	0.51	1.35
BGLCN50	4.8	0.5	254	0.34	1.41
BGLF	3	0.1	178	1.26	1.87
BGLC-NH3	14	-	405	0.27	3.71
CaBGLC10	2.6	-	129	0.66	1.16
CsBGLC15	4.2	-	209	0.56	1.61
KBGLC05	3	-	109	0.65	1.99
KBGLC15	5.6	-	190	0.45	4.38

9.7 EIS Deconvolution Data

Table 9.5: Mean values of parameters from the deconvolution of the EIS spectra extracted at the overpotential giving 10 mA cm^{-2}_{geo}. Values above the horizontal line are mean values from three independent measurements, the rest are from one measurement. Fitting was done with χ^2 values below 10^{-4}.

Electrocatalyst	R_s (Ω)	R_d (Ω)	Y_d (F)	n_d	R_{int} (Ω)	Y_{int} (F)	n_{int}
BGLC587	10	7	1.1E-03	0.60	19	3.5E-04	0.83
BGLCF10	9	3	1.7E-04	0.78	21	3.2E-04	0.81
BGLCF30	12	2	2.7E-04	0.68	18	3.4E-04	0.82
BGLCF50	8	2	7.9E-04	0.69	21	3.7E-04	0.83
BGLCF70	7	6	1.8E-04	0.66	22	4.2E-04	0.80
BGLCFN1020	9	4	1.5E-04	0.85	24	3.0E-04	0.76
BGLCFN1040	12	2	6E-05	0.94	34	2.8E-04	0.71
BGLCFN2010	9	2	1.3E-04	0.83	17	3.2E-04	0.83
BGLCFN3020	8	2	3.1E-04	0.80	28	2.2E-04	0.78
BGLCN10	8	2	1.3E-04	0.88	19	2.6E-04	0.78
BGLCN50	8	3	3.1E-04	0.72	23	4.2E-04	0.74
BGLF	9	6	2.2E-04	0.80	45	1.9E-04	0.81
BGLC-NH3	11	3	1.8E-04	0.83	10	5.1E-04	0.81
CaBGLC10	7	1	4E-05	1.00	33	2.3E-04	0.73
CsBGLC15	8	4	2.0E-04	0.78	26	3.0E-04	0.79
KBGLC05	14	4	1.3E-04	0.82	32	2.7E-04	0.75
KBGLC15	16	2	1.5E-04	0.81	23	4.1E-04	0.76

Table 9.6: Mean values of parameters from the deconvolution of the EIS spectra extracted at the onset overpotential. Values above the horizontal line are mean values from three independent measurements, the rest is from one measurement. Fitting was done with χ^2 values below 10^{-4}. Values to the right of the vertical line are calculated from the deconvolution values to the left of the line. Since the exponent value, n_d, of the CPE_d's is close to 0.5, it shows a Warburg behaviour. This is indicative of a purely diffusive process and we therefore disregarded this in the calculation of the C_{dl}.

Electrocatalyst	R_s (Ω)	R_d (Ω)	Y_d (F)	n_d	R_{int} (Ω)	Y_{int} (F)	n_{int}
BGLC587	8	42	5.8E-03	0.37	533	3.8E-04	0.93
BGLCF10	8	18	2.0E-03	0.53	521	2.9E-04	0.92
BGLCF30	15	20	4.9E-03	0.46	607	2.5E-04	0.93
BGLCF50	8	6	4.8E-03	0.61	726	3.1E-04	0.88
BGLCF70	7	17	4.6E-03	0.46	708	2.9E-04	0.94
BGLCFN1020	9	15	5.8E-04	0.67	405	1.8E-04	0.88
BGLCFN1040	8	12	4.4E-04	0.71	384	1.7E-04	0.84
BGLCFN2010	9	11	5.5E-03	0.45	555	2.7E-04	0.92
BGLCFN3020	8	12	6.3E-04	0.67	474	1.5E-04	0.87
BGLCN10	7	20	7.8E-04	0.63	409	2.4E-04	0.88
BGLCN50	8	27	3.5E-03	0.49	252	3.1E-04	0.88
BGLF	9	55	8.3E-04	0.66	832	3.7E-04	0.75
BGLC-NH3	9	6	2.2E-03	0.61	246	5.3E-04	0.88
CaBGLC10	6	17	1.2E-03	0.61	553	2.8E-04	0.81
CsBGLC15	7	15	1.0E-03	0.60	574	2.9E-04	0.90
KBGLC05	14	43	7.3E-04	0.64	509	3.5E-04	0.82
KBGLC15	16	63	4.2E-03	0.49	481	3.8E-04	0.95

Table 9.7: Mean values of parameters from the deconvolution of the EIS spectra extracted in the non-Faradaic region potential region. Values above the horizontal line are mean values from three independent measurements, the rest is from one measurement. Fitting was done with χ^2 values below 10^{-4}. Values to the right of the vertical line are calculated from the deconvolution values to the left of the line. The dash indicates pure resistive behaviour of R_{int}.

Electrocatalyst	R_s (Ω)	R_d (Ω)	Y_d (F)	n_d	R_{int} (Ω)	Y_{int} (F)	n_{int}
BGLC587	9.3	9.5	3.0E-04	0.70	115285	1.2E-04	0.81
BGLCF10	8.5	9.3	3.7E-04	0.73	335623	1.1E-04	0.84
BGLCF30	13.0	22.9	1.1E-03	0.59	71045	1.0E-04	0.87
BGLCF50	8.3	17.3	7.0E-04	0.67	129495	1.2E-04	0.85
BGLCF70	10.2	11.8	1.1E-03	0.55	-	1.4E-04	0.80
BGLCFN1020	9.6	8.2	2.7E-04	0.78	-	9.1E-05	0.87
BGLCFN1040	10.1	7.6	9.7E-04	0.74	-	9.3E-05	0.84
BGLCFN2010	9.3	4.7	3.8E-04	0.75	-	1.1E-04	0.86
BGLCFN3020	8.2	7.7	3.7E-04	0.76	-	9.4E-05	0.86
BGLCN10	7.5	3.8	1.8E-04	0.86	-	1.0E-04	0.84
BGLCN50	8.4	12.9	6.5E-04	0.65	-	1.1E-04	0.84
BGLF	9.1	3.5	1.3E-04	0.89	12937	8.4E-05	0.84
BGLC-NH3	8.8	19.1	2.0E-03	0.62	-	2.2E-04	0.87
CaBGLC10	6.6	1.8	4.9E-05	0.96	-	8.6E-05	0.82
CsBGLC15	7.5	9.8	5.1E-04	0.70	-	1.1E-04	0.85
KBGLC05	13.8	3.1	1.8E-04	0.86	-	1.3E-04	0.79
KBGLC15	16.1	12.5	2.8E-03	0.55	-	1.4E-04	0.81

9.8 Double Layer Capacitances and BET Surface Area

Table 9.8: The double layer capacitances in the non-Faradaic (capacitive) region as found by low and high scan rate CV data and EIS, in the onset potential region and at 10 mA cm^{-2}_{geo}. The rightmost column gives the BET surface area of the ECs.

Electrocatalyst	Non-Faradic region			OER onset	10 mA cm^{-2}_{geo}	Ex situ
	$C_{dl,CV,low}$ (mF)	$C_{dl,CV,high}$ (mF)	$C_{dl,EIS}$ (mF)	$C_{dl,EIS}$ (mF)	$C_{dl,EIS}$ (mF)	BET (m^2 g^{-1})
BGLC587	59	33	20	487	18	0.785
BGLCF10	48	30	40	94	18	0.823
BGLCF30	38	27	46	352	10	1.171
BGLCF50	51	34	44	90	17	1.604
BGLCF70	45	36	41	238	8	1.901
BGLCFN1020	33	19	51	55	17	0.827
BGLCFN1040	37	22	86	52	17	0.716
BGLCFN2010	42	27	46	175	19	0.605
BGLCFN3020	32	22	57	56	24	0.723
BGLCN10	39	25	64	69	23	0.541
BGLCN50	49	30	54	290	13	1.131
BGLF	43	23	36	176	24	3.552
BGLC-NH3	76	63	296	158	29	-
CaBGLC10	43	21	34	109	19	-
CsBGLC15	44	27	54	62	19	-
KBGLC05	60	39	54	106	18	-
KBGLC15	64	42	177	1015	18	-